2003

Experimental study of heat transfer from a moving and evaporating meniscus on a heated surface

Wai Keat Kuan

EXPERIMENTAL STUDY OF HEAT TRANSFER FROM A MOVING AND EVAPORATING MENISCUS ON A HEATED SURFACE

By

Wai Keat Kuan

A Thesis Submitted in
Partial Fulfillment Of the
Requirement for the

MASTER OF SCIENCE
IN
MECHANICAL ENGINEERING

Approved by:

Dr. Satish G. Kandlikar Department of Mechanical Engineering	Satish G. Kandlikar (Thesis advisor)
Dr. Jian Yu Department of Mechanical Engineering	Jian Yu
Dr. P. Venkataraman Department of Mechanical Engineering	P. Venkataraman
Dr. Alan H. Nye Associate Department Head of Mechanical Engineering	Alan H. Nye

DEPARTMENT OF MECHANICAL ENGINEERING
ROCHESTER INSTITUTE OF TECHNOLOGY

JULY, 2003

Thesis Reproduction Permission Statement

Experimental Study of Heat Transfer from a Moving and Evaporating Meniscus on a Heated Surface

I, Wai Keat Kuan, hereby grant permission to the Wallace Library of the Rochester Institute of Technology to reproduce my thesis in whole or in part. Any reproduction will not be for commercial use or profit.

Date: August 14, 2003 Signature of Author: Wai Keat Kuan

Publications

• **Circular Evaporating Meniscus – A New Way to Study Heat Transfer Mechanism During Nucleate Boiling** (Wai Keat Kuan and Satish G. Kandlikar), 5th International Conference on Boiling Heat Transfer 2003, Jamaica, May 4-8.

• **Experimental Study on the Moving Interface Using a Meniscus on a Rotating Surface** (Wai Keat Kuan and Satish G. Kandlikar), Paper No HT2003-47449, ASME Summer Heat Transfer Conference, Las Vegas, Nevada, July 21-23, 2003, ASME.

Acknowledgements

I am very grateful of my time spent at Rochester Institute of Technology, made possible by Eugene Clark, and the steadfast support of my wife.

First, I thank my thesis advisor, Professor Kandlikar who gave me the opportunity and inspired my interest in the field of Meniscus Heat Transfer. His patience with me, knowledge in heat transfer, and enthusiasm for learning has given me an education that I will always value. I thank him for his guidance while working on my thesis, advise, and being my mentor.

Thanks to Dave Hathaway and Steve Kosciol who gave their valuable time, skills and enthusiasm to make this project work.

I would like to thank to Connie LaBarre and Diane Selleck for their help in getting me started at Rochester Institute of Technology, and their ongoing commitment to student success.

Finally, I would like to thank my wife who put up with a husband who spent many long nights working downstairs, and for the encouragement, care and support that she has given to me during my time at Rochester Institute of Technology.

Abstract

A stable meniscus is formed between a needle dispensing water over a heated circular face of a rotating copper block. The needle is offset from the axis of rotation and thus forms a moving meniscus. The water flow rate, heater surface temperature and the speed of rotation are controlled to provide a stable meniscus with complete evaporation of water without any meniscus break-up. The experimental heat transfer rate is compared with the transient heat conduction model. The results indicate that the transient heat conduction plays a major role in the heat transfer process from a moving meniscus. The study provides an important insight on the role of transient conduction around a nucleating bubble in pool boiling.

Nomenclature

A – Area, m^2

c_p – Specific heat of water at constant pressure, J/kg-°C

h_{fg} – Latent heat of vaporization, J/kg

k – Thermal conductivity, W/m-°C

L – Distance between the advancing and receding fronts along the heater surface, m

$\dot{m}$ – Mass flow rate, kg/s

P – Perimeter, m

q' – Heat transfer rate per unit contact line length, W/m

q'' – Heat flux , W/m^2

$T_{w,in}$ – Water supply temperature, °C

$T_{w,i}$ – Water temperature at the inlet to the transient conduction region, °C

$T_{S,i}$ – Initial heater surface temperature at for the transient conduction, same as the heater block temperature, °C

T_S – Heater surface temperature, °C

$T_{i,S-W}$ – Interface temperature between surface and water, °C

t – time elapsed after the initial contact of water with the heater surface at the advancing front, s

t_{max} – time required for the heater surface to move from the advancing to the receding liquid-vapor interface, s

V – relative velocity between the heater surface and the meniscus, m/s

Greek Letters

α – Thermal diffusivity, m^2/s

ρ – Density, kg/m^3

Subscripts

S – Heater surface

S-W – Interface between surface and water

w – Water supply

Table of Contents

List of Figures

List of Tables

1. Introduction

Heat transfer during nucleate boiling is associated with bubble nucleation, its growth and subsequent departure from a heated surface. Heat transfer at the liquid-vapor interface with a moving contact line on a heated surface is of great interest in boiling studies. The meniscus region heat transfer is not well understood in spite of a large number of experimental, analytical and numerical studies conducted over several decades. A major challenge has been in obtaining accurate and detailed information on the thermal behavior at the liquid vapor interface and its interaction with the heated surface.

A number of recent investigations focused on obtaining the local information on the heater surface under a bubble using microelectronic fabrication technology (Holm 1979, Swanson 1992, Hallinan 1994, Khrustalev 1996, Kim 1996, etc.]. Their results have provided useful information, but the detailed description of the heat transfer mechanism during boiling still remains illusive. The interface shape, contact angles during bubble growth, and accurate heat transfer rate for each bubble still remain unknown. A direct measurement of heat flux under an evaporating meniscus is useful in providing an insight on the associated heat transfer phenomena. The heat transfer around a nucleating bubble is in many respects similar to the advancing and receding motion of the meniscus on a heated surface.

A novel technique is presented in this thesis by which we can access the liquid-vapor interface and the contact line region (defined as the region where the liquid-vapor interface meets the heater surface). Figure 1 presents a comparison between a moving meniscus and a nucleating bubble. As the bubble grows, the liquid-vapor interface advances into the liquid; the receding liquid front of a moving meniscus represents this region of the bubble ebullition

cycle. As the bubble grows to its departure size, its footprint on the heater surface rapidly shrinks as the liquid front advances over the region that formed the bubble base during the bubble growth period. This region of rewetting is represented by the advancing liquid front of a moving meniscus.

A clear influence of the meniscus velocity on heat flux was demonstrated by Kandlikar and Kuan (2003). In these experiments, heat flux was found to increase linearly with the meniscus velocity from 0 to 1.8 m/s. Further increase in velocity caused a meniscus breakdown. The variation of advancing and receding contact angles with meniscus velocity was also studied over the range of parameters investigated.

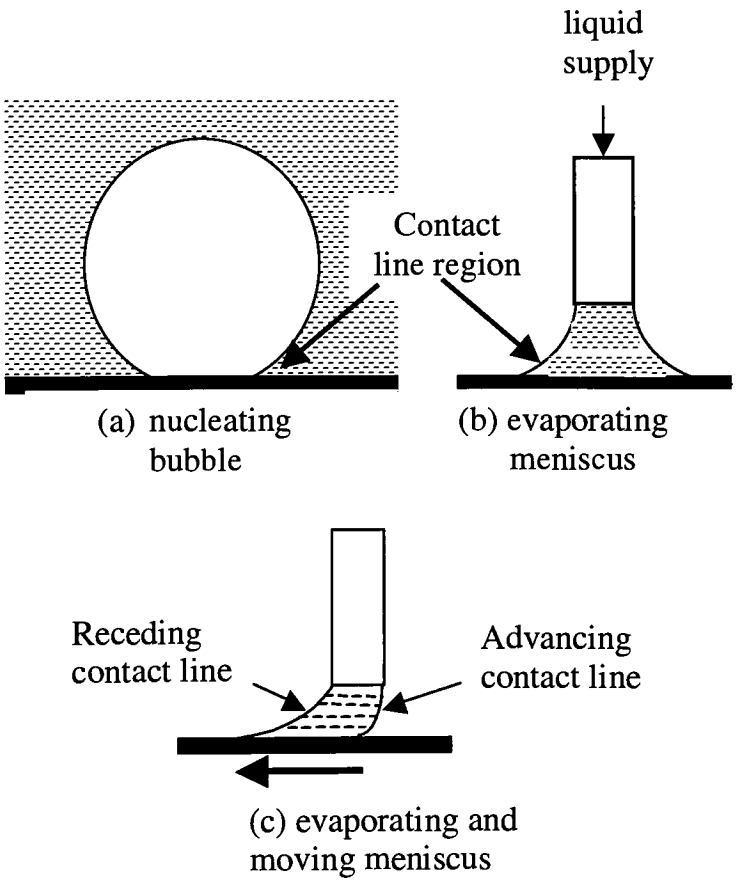

Figure 1: Similarity between a nucleating bubble and an evaporating meniscus in the contact line region

The advantages of studying the meniscus geometry are fairly obvious: (i) the liquid-vapor interface and the contact line region can be viewed clearly without any obstruction from the highly active boiling phenomena occurring around a bubble in pool boiling, (ii) the liquid flow rate provides a direct measurement of the heat transfer rates over the wetted region bounded by the advancing and receding interfaces, as all liquid that is supplied is evaporated at the interface under stable operating conditions.

2. Literature Survey

Previous studies on meniscus mainly focused on stationary menisci, which were formed inside or at the outlet end of a capillary or a small diameter tube, or at a straight edge between two intersecting surfaces. The focus of most of these studies [1-7 and 11-28] was the microscale and macroscale heat transfer and fluid mechanics in the vicinity of the stationary contact line region. A brief overview of available literature is presented here. Also, Table 1 provides a summary of previous studies on meniscus

In 1978, Wayner stated that viscous flow in a thin film in the immediate vicinity of the interline (junction of solid-liquid-vapor) significantly affects the complete profile of an evaporating meniscus. This change as a function of heat flux was theoretically analyzed based on the premise that fluid flow was caused by the London-van der Waals dispersion force. In the analysis, the change in the apparent contact angle from its intrinsic value was attributed to viscous effects only and did not include a surface roughness effect. The extended meniscus was divided into three zones: 1) the immediate vicinity of the interline (the thin film region), where the thinkness of the liquid can vary from a monolayer to approximately 500Å; 2) the inner intrinsic meniscus region, where the thickness range is approximately $0.05 - 10 \times 10^{-6}$ m; and 3) the outer intrinsic meniscus region, where the thickness is greater than 10^{-5} m. As shown in Figure 2, the curvature of the outer intrinsic meniscus becomes a constant as the centerline of the capillary is approached.

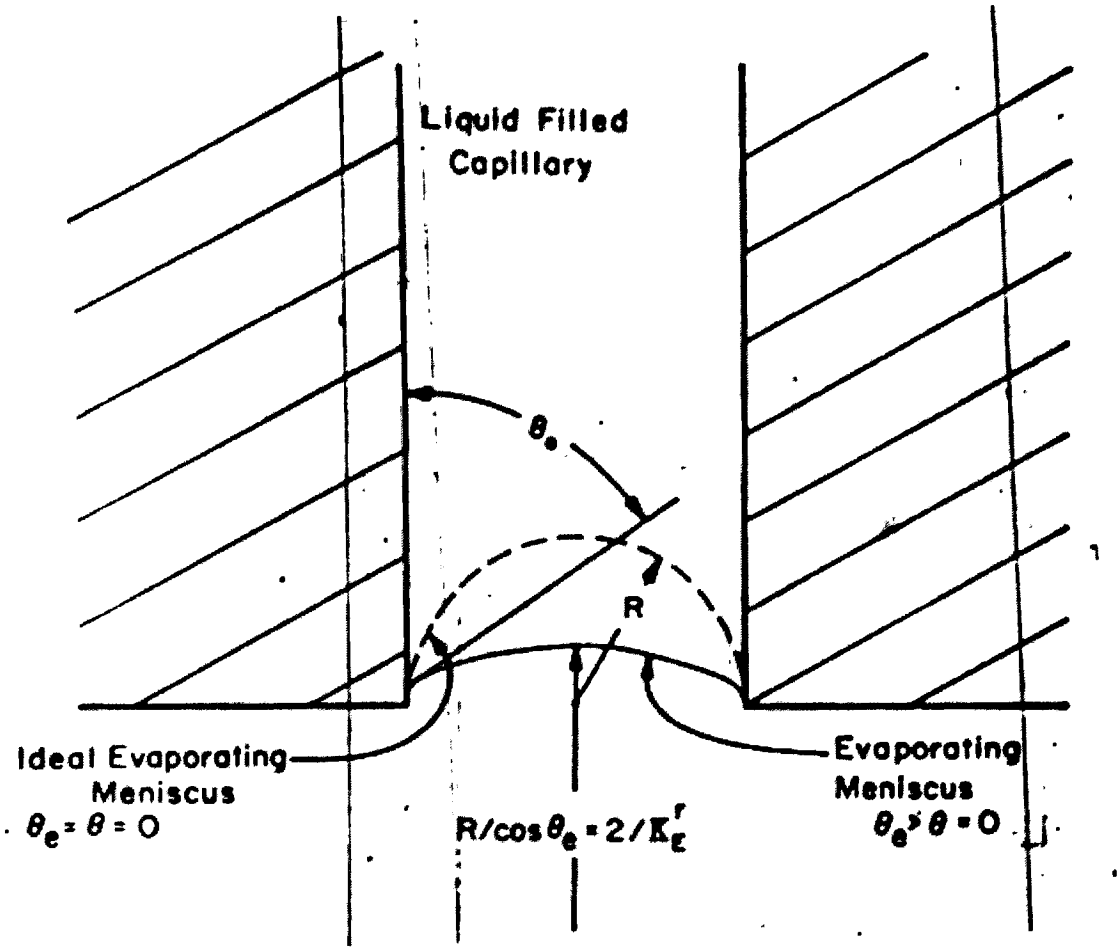

Figure 2: Evaporating meniscus profile (Wayner, 1978)

Holm and Goplen stated in 1979 that very high heat transfer rates have been observed near the triple interline, the junction of the vapor, the evaporating thin film, and the non-evaporating adsorbed thin film. Dropwise condensation was used as an example that exhibits surface heat transfer coefficients that are approximately one order of magnitude greater than the coefficients resulting from film condensation. At the same time, Holm and Goplen demonstrated that the extent of interline dispersion at any time can be controlled by using capillary grooves partially filled with a liquid as a means of forming the triple interline region. As shown in Figure 3, the number and length of the interlines can easily be controlled by the number and length of the grooves, thus allowing them to control the extent of interline dispersion. The heat transfer is augmented by the flow of the liquid into the groove under the action of capillary forces, a passive process. Because of the small physical dimentions associated with a meniscus, the local characteristics of the combined heat and mass transfer process was deduced from overall characteristics such as: i) total heat transfer from a grooved plate, ii) overall temperature drops in the walls separating the grooves, and iii) the temperature difference between the top of the wall and the surrounding vapor.

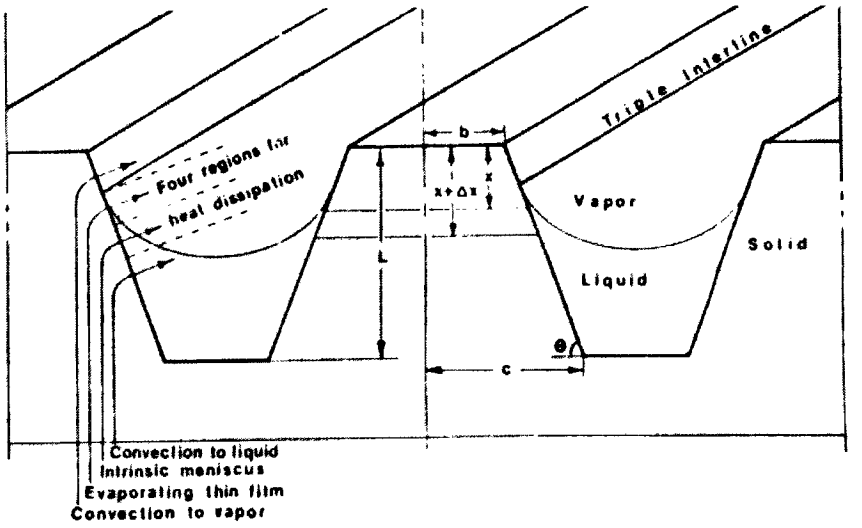

Figure 3: Liquid-filled capillary grooves on a plate (Holm and Goplen, 1979)

In 1992, Swanson and Herdt formulated a mathematical model describing the evaporating meniscus in a capillary tube incorporating the full three-dimensional Young-Laplace equation, Marangoni convection, London-van der Waals dispersion forces, and non-equilibrium interface conditions. The governing equations and boundary conditions were cast in terms of five coupled non-linear ordinary differential equations and solved numerically. The model was tested using various values of the dimensionless superheat and dispersion number. Figure 4 shows the various flow regions in a capillary tube.

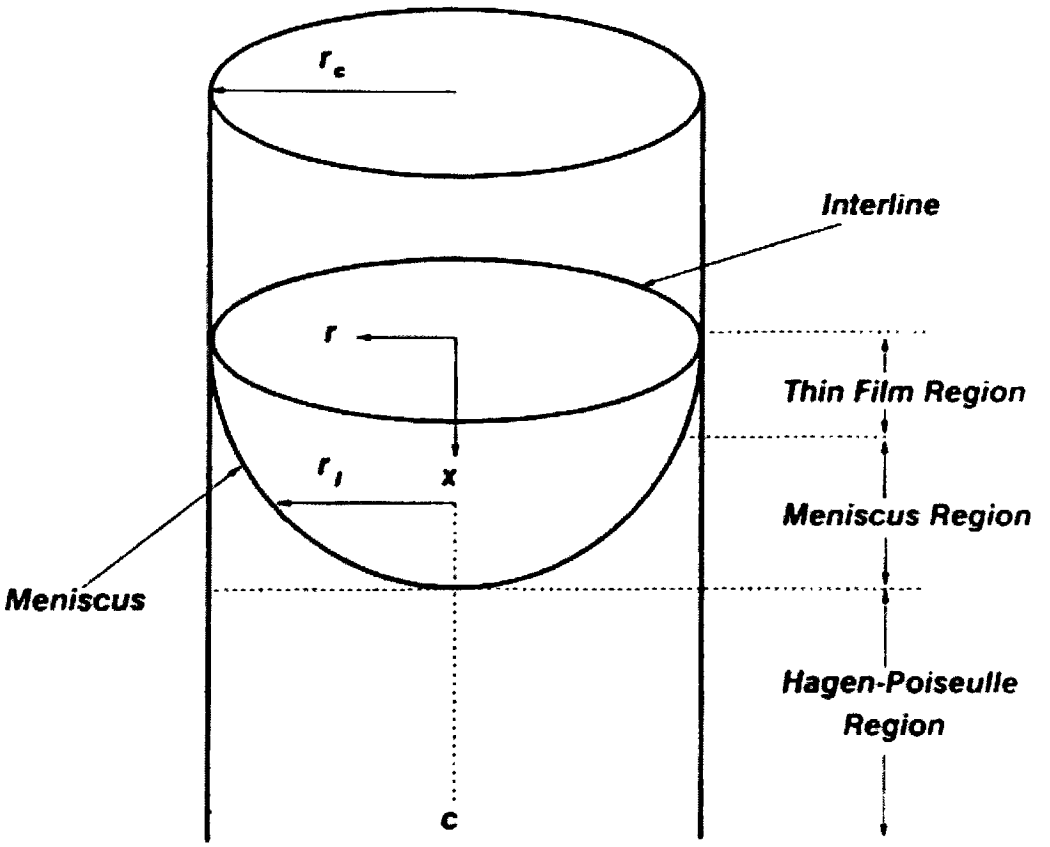

Figure 4: Flow regions for an isolated evaporating meniscus in a capillary tube (Swanson and Herdt, 1992)

In 1994, Hallinan, Chebaro, Kim and Chang determined the effects of evaporation from the thin film region of a liquid-vapor meniscus within the micropores of a heat pipe porous or grooved wick on the interfacial shape, temperature distribution, and pressure distribution. Figure 5 shows a rectangular coordinate frame of reference used in the study. The x axis is along the wall and y axis normal to the wall.

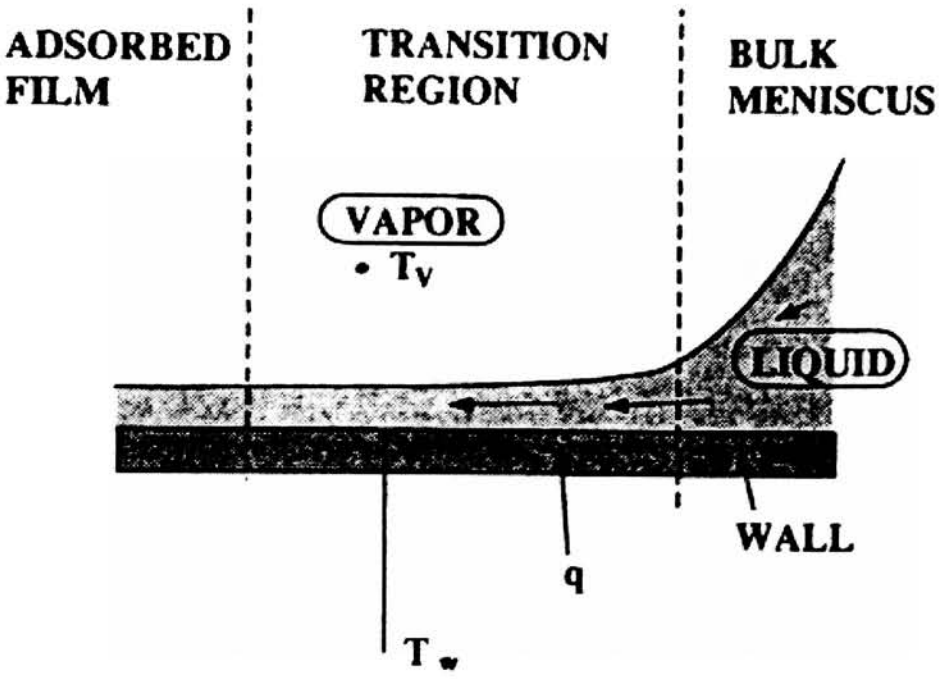

Figure 5: Thin film region between an adsorbed film and a meniscus (Hallinan, et al., 1994)

Khrustalev and Faghri (1996) developed a mathematical model of the evaporating liquid-vapor meniscus in a capillary slot in 1996. The model consists of two-dimensional steady-state momentum conservation and energy equations for both the vapor and liquid phases, and incorporates the existing simplified one-dimensional model of the evaporating microfilm. Figure 6 illustrates the liquid-vapor meniscus interface in a narrow slot used in the mathematical model. A constant wall temperature, T_w is assumed in the analysis since the solid wall thermal conductivity is significantly higher than that of liquid.

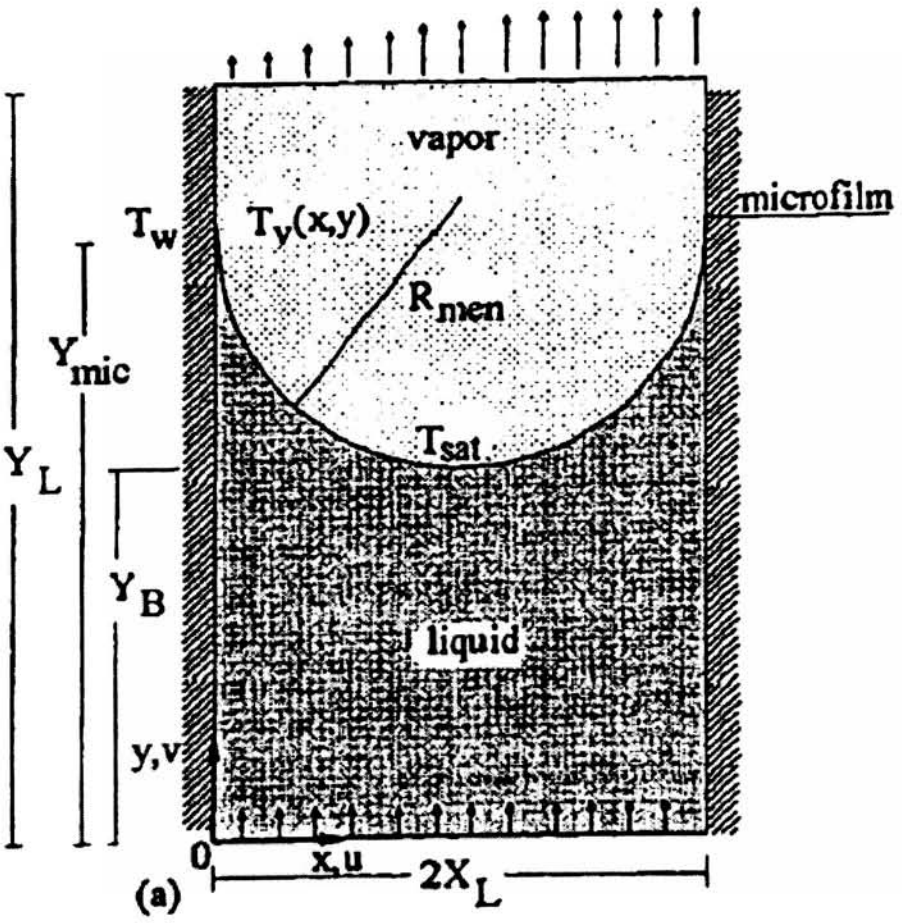

Figure 6: Computational domain conventions for an evaporating liquid-vapor meniscus (Khrustalev and Faghri, 1996)

Kim and Wayner (1996) experimentally and theoretically evaluated the microscopic details of fluid flow and hear transfer in the contact line region of an evaporating curved liquid film in 1996. In their experiment, the evaporating film thickness profiles were measured optically using null ellipsometry and image analyzing interferometry. The pressure field was obtained from the thickness profiles using the augmented Young-Laplace equation. Using the liquid pressure field, the evaporative mass flux profile was obtained from a Kelvin-Clapeyron model for the local vapor pressure. Using octane as the working fluid, the evaporating meniscus is formed in the circular experimental cell as shown in Figures 7 and 8.

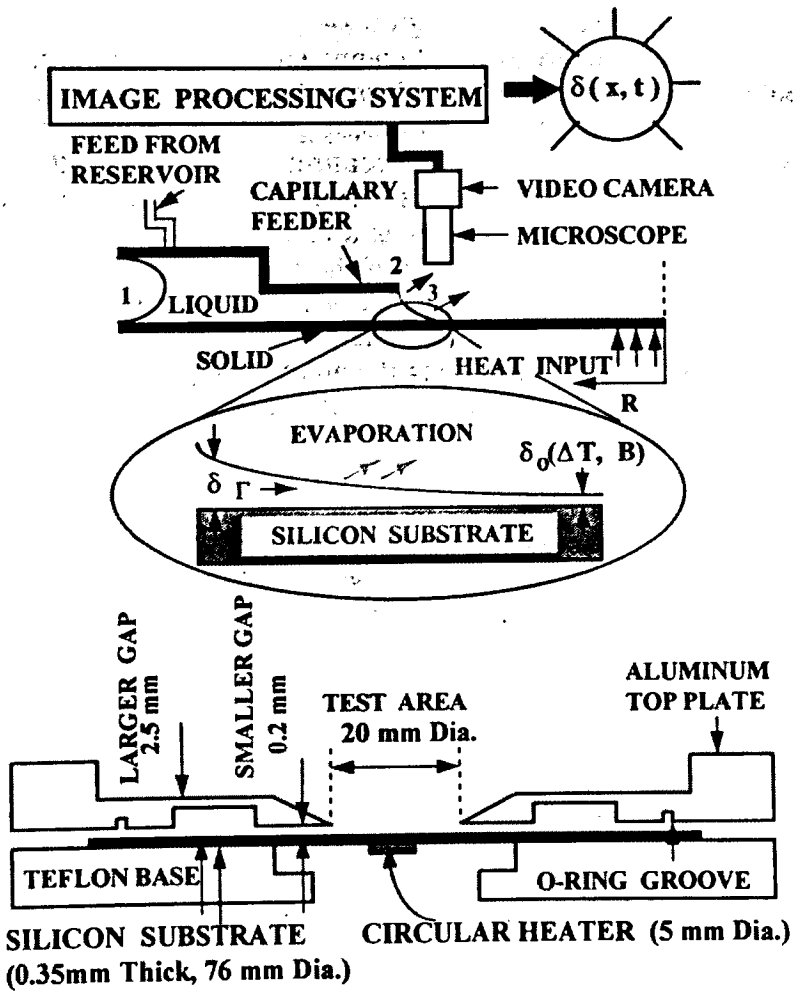

Figure 7: Cross-sectional view of a circular capillary heat transfer cell (Kim and Wayner, 1996)

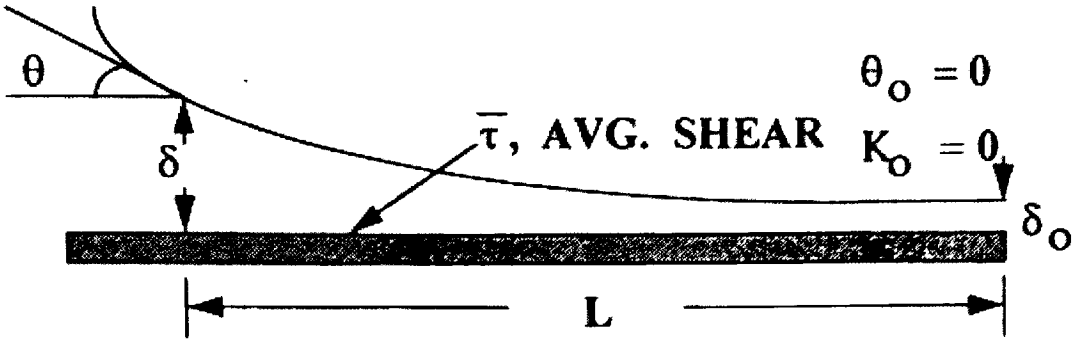

Figure 8: Evaporating meniscus (Kim and Wayner, 1996)

Table 1: Summary of Available Literature on Meniscus

Author (Year)	Meniscus Geometry	Meniscus Details	Working Fluid	Experimental or Analytical	Major Conclusions
Wayner (1978)	Please refer to Figure 2	$K_E^r = 2\cos\theta_e/R$ where K_E^r is the curvature	CCl_4 – Quartz	Analytical	Viscous flow of evaporating liquid in interline region has significant effect on contact angle of the meniscus. For large heat flux, effective contact angle can be the order of 30 degree.
Holm and Goplen (1979)	Please refer to Figure 3	Grooved plate 0.02 in wide separated by walls 0.05 in high. Width of wall varies from 0.001 in to 0.01 in. Wall angle is 90 degree. Groove length is 1 ft.	The model could use any kind of liquids.	Experimental and analytical.	Thin-film transition region, approximately 0.005 in to 0.006 in high and located at the top of the intrinsic meniscus accounts for approximately 80% of the heat dissipated from the wall.
Swanson and Herdt (1992)	Please refer to Figure 4	Tube radius, r_c less than 100 μm. Average radial location of the meniscus is less than 0.2 m.	Room temperatu re and pressure hexane.	Analytical	Varying the dimensionless superheat, for a constant dissipation number (number characterizing the London-van der Waals forces in the thin film region), had no apparent effect on the meniscus profile. However, varying the dispersion number did produce a noticeable microscopic change in the meniscus profile near the tube wall. Contact angle is independent o fthe dimensionless superheat or dispersion number.
Hallinan, et al. (1994)	Please refer to Figure 5	X varies from 0 to 45 microns, where X = 0 at the intersection of the absorbed film with the thin film.	Ammonia	Analytical	Maximum evaporation fluxes from the wall-heated meniscus are present in the ectended meniscus when constant wall temperature, and therefore nonisothermal interfacial conditions, are considered.
Khrustale v and Faghri (1996)	Please refer to Figure 6.	X_L = 50 μm, Y_L = 400 μm, Y_B = 100 μm, and θ_{men} = 15°.	Water	Analytical	The fliud flow effect on the heat transfer during evaporation from the liquid-vapor meniscus results in the increase of the effective heat transfer coefficient by up 30%.

Kim and Wayner (1996)	Please refer to Figures 7 and 8.	δ = 20 nm and 40 nm. δ_0 ranges from 3.9 x 10^{-9} m to 1.9 x 10^{-8} m. Relative distance at specific δ is from 0 to 300 μm.	Octane	Experimental and Analytical.	The shape (thinkness, slope, curvature, and apparent contact angle) of the liquid-vapor interface is a function of the evaporative heat flow rate per unit width of the meniscus. The viscous losses that are directly related to the flow of the evaporating liquid in the thinnest part of the evaporating meniscus have the dominant effect on the base curvature.

3. Objectives of Present Work

The objectives of the present work are as follows:

1. Develop an apparatus to investigate stationary and moving liquid-vapor interface formed by a meniscus on a heated surface,
2. Study the interface characteristics – advancing and receding contact angles, meniscus stability, and break-off through high-speed photographic techniques,
3. Obtain quantitative information on the size and shape of the meniscus as a function of water flow rate, meniscus velocity and heater surface temperature,
4. Obtain quantitative information on the heat transfer rates from the meniscus as a function of water flow rate, meniscus velocity and heater surface temperature, and
5. Compare the experimental results with an analytical model presented in Kandlikar and Kuan (2003) for the heat transfer between the heater surface and the liquid contained inside the meniscus.

4. Experiment Apparatus

An overall schematic of the experimental setup is shown in Figure 9. It consists of fluid delivery system, stationary and moving test sections and high speed imaging cameras. These subsystems are explored in this section.

4.1 Fluid Delivery System

The experimental setup for the fluid delivery system is designed to deliver degassed and de-ionized water to a dispensing needle. Using the Gilmont Direct-Reading Variable Area Flowmeter (2001/02 Cole-Parmer catalog number: U-03234-51), it can deliver water mass flow rates ranging from 0.002 – 1.1 mL/min. Figure 9 shows a schematic of the water delivery system. The system includes a degassed water pouch (1000 mL IV pouch from Baxter Health Care Corporation), the Gilmont flowmeter with attached regulator valve, and a dispensing needle (B-D PrecisionGlide 16G1 needle) as shown in Figures 32, 33 and 34 respectively in Appendix A. Note that the tapered end of the needle is removed by grinding it to eliminate any effects that it might have on the meniscus.

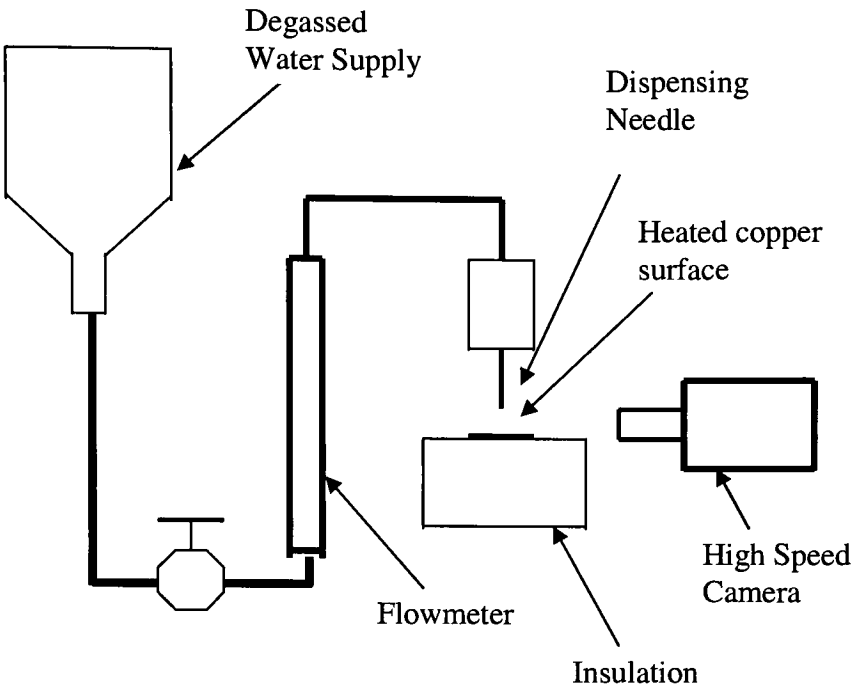

Figure 9: Fluid delivery system degassed water pouch, flow meter with regulator valve, and dispensing needle

4.2 Stationary and Rotating Test Sections

The test section details are shown in Figures 10 and 11. Figure 10 shows the schematic of the stationary test section used in the present study. A copper block with a 10 mm diameter cylindrical extension is used as the heated surface. It is heated with the cartridge heater as shown. The dimension of the cartridge heater is one inch in length with a quarter inch in diameter. In Omega catalog, the model number of the 120 V and 20 Watts cartridge heater is CSS-10120/120. The top surface of the copper block is polished with a 1 micron slurry in the final stage of polishing. The polished surface prevents any boiling inside the meniscus by removing large sized nucleation cavities. This allows a superheat of around 8 to 10 degrees Celsius without nucleation occurring inside the meniscus, thus providing a stable evaporating meniscus.

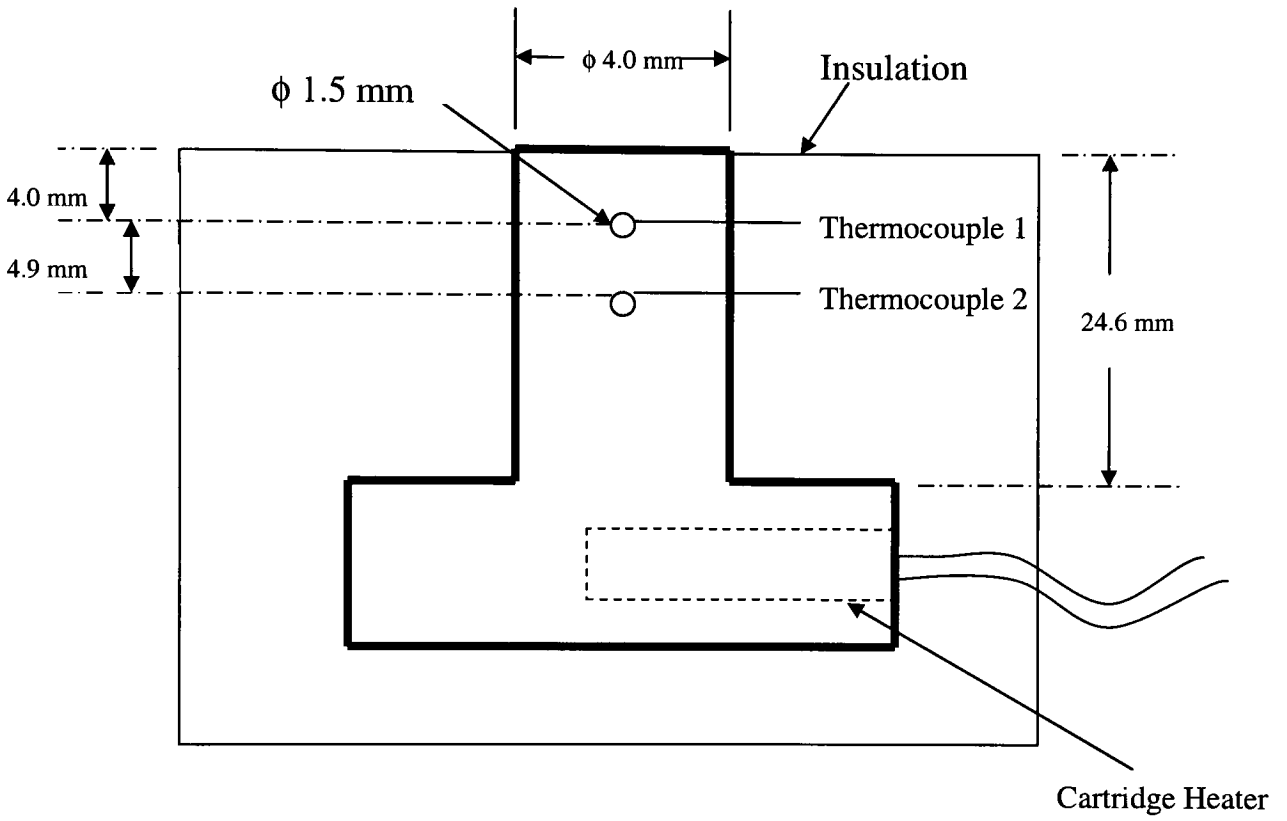

Figure 10: Stationary test section schematic

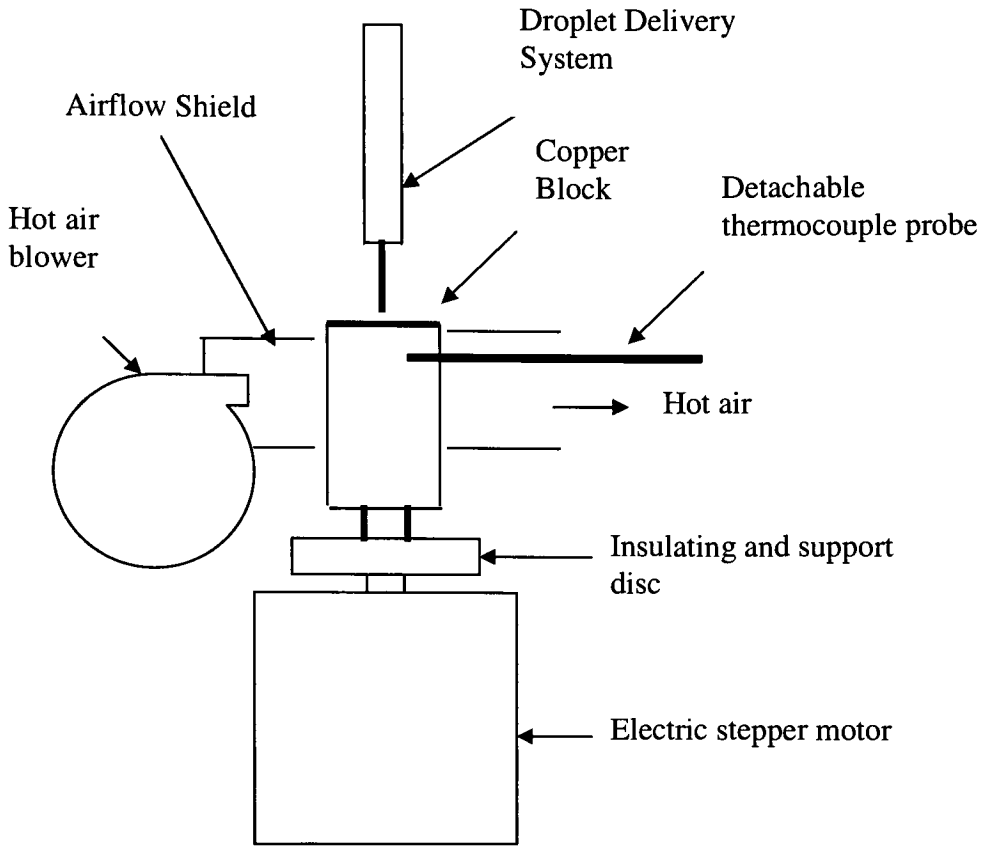

Figure 11: Rotating test section schematic

Figure 11 shows the schematic of a rotating test section. A copper block, 37 mm in diameter and 63 mm long is placed on an insulating and support disc (2002 Edmund Optics catalog number: A03-678) with four screw attachments to minimize the conduction losses. The top surface of the copper block is also polished with the 1 micron slurry in the final stage of polishing. After the polishing, the measured average surface roughness value is 0.04 μm. The assembly is then mounted on the shaft of an electric DC motor (Pittman, model number: GM8724S011) whose rotational speed can be closely controlled by supplying voltage from a digitally regulated DC power source, 0-20 Volts (Hewlett Packard, model number: 6572A).

The test section is heated to the desired temperature by adjusting the temperature of an electric blower (2001/02 Cole-Parmer catalog number: U-03026-00) that blows hot air over the cylindrical surface of the copper block. The airflow is shielded from the heater surface as shown. A K-type thermocouple probe is used to measure the temperature by stopping the rotation and inserting the probe in a hole made in the copper block. Because of the large mass of the copper block, the temperature does not change during the measurement. The copper surface is made level and true to the rotational axis so that the distance between the needle and the heater surface does not change as the motor turns the heater assembly. The needle is positioned at a certain radial distance from the center of rotation. This provides the necessary relative velocity as the heater surface turns. By adjusting the voltage to the electric motor, the rotational speed of the heated copper block can be closely controlled. The complete assembly of the rotating test section can be seen in picture A4 in Appendix A. Copies of the equipment as appeared in the catalogs can be found in Appendix D.

4.3 High Speed Cameras

The images of the meniscus are obtained using a microscopic lens attached to two high-speed cameras that are both capable of recording frame rates of up to 8000 fps. The cameras are mounted on tripods and are located at an angle of 90 degrees apart from each other. One is used to obtain the side view of the meniscus, while the other one is used to view the meniscus outline from the above at 45° angle. Using two cameras, we can obtain the width and length of the meniscus.

5. Experimental Procedure

5.1 Water Supply

The water-degassing process is presented in Kandlikar, Steinke and Balasubramanian (2002). The procedure developed by Mark Steinke is employed to produce degassed water that is supplied to the needle. De-ionized and filtered water is degassed by boiling it at 15 psi (105 kPa) in a commercially available pressure cooker. Using a deadweight corresponding to 15 psi on the pressure cooker, and removing it after full pressure is attained, the air dissolved in water is forced out along with the steam through the chamber due to rapid depressurization of the water. At 15 psi, the water is degassed to a saturation temperature of 121 °C. During the experiment, if the degassed water temperature remains below of 121 °C, the remaining dissolved air will not precipitate from the degassed water. The water is then cooled to room temperature using a plate heat exchanger. The degassed water is then contained in an air-sealed water pouch that delivers a regulated continuous supply of degassed water to the dispensing needle. The water mass flow rate is regulated by a flow meter with attached regulator valve. Using a digital scale that is accurate to three decimal places and a stop watch, the water mass flow rates that correspond to the flow meter readings are determined. Before the start of each data taking sessions, the water mass flow rate is turned to its maximum for 3 to 5 minutes to purge out any air that might exist in the water feeding tubes.

5.2 Stationary and Rotating Test Sections

The top surface of the copper block is polished with a 1 micron slurry each time prior to each data taking session. After that, the stationary and rotating copper blocks are heated with a cartridge heater and a hot air blower respectively. The stationary test section is heated to the desire temperature by adjusting the current supplied to the cartridge heater. The rotating test section is heated to the desire temperature by adjusting the temperature of an electric blower that blows hot air over the cylindrical surface of the copper block. The steady state temperature of the test sections are measured using thermocouple probes. Water droplets are delivered to the top surface of the copper blocks as soon as the desired steady state temperature is achieved. The water mass flow rate can be changed using the regulator valve which is attached to the flow meter.

In addition, for the rotating test section, prior to each data taking session, the needle height and needle position are adjusted to a certain height from the top surface of the copper block and the same radial distance from the center of rotation respectively. This procedure is done using the vision software (Encore 2.20) and the images captured by the high speed cameras. The needle height, is set to 0.9 mm above the heater surface. The constant radial distance of the meniscus from the axis of rotation provides a consistent range of the relative meniscus surface velocities through out the experiments. The rotational speed can be closely controlled by supplying voltage from a digitally regulated power source. The rotational speeds that correspond to the supplying voltages are determined using a marking on the cylindrical surface of the copper block, the vision software, and the timed images captured by a high speed camera. Finally, the images of the meniscus are obtained using two high speed

cameras that are mounted on tripods. The cameras are located at an angle of 90 degrees angle apart from each other as shown in picture A4 in Appendix A.

5.3 Advancing and Receding Contact Lines Angles

The advancing and receding contact lines angles are measured using PRO-Engineering software program. The images of the meniscus captured by the high speed cameras are first imported into the vision software program, and then the angles are measured by drawing lines from the edge of the meniscus using the top surface where the meniscus sits on as the line of reference.

6. Experimental Uncertainties

The velocity of the rotating surface, the heater surface temperature, and the flow rate of water are three major parameters in this study. The flow rate of water is measured using a precision flow meter that is calibrated by actual measurement of flow using a chemical weighing scale over a 5-minute period. The accuracy of flow measurement is within ± 2 percent. The temperature measurement is accurate to within ± 0.1 °C. The rotational speed is measured by calibrating the speed versus supply voltage. This is done in the vision software using the time steps with an indicator located on the rotating copper block. The error in measuring the distance of meniscus from the center of rotation is estimated to be 0.5 mm. The overall error in velocity measurement is estimated to be ± 3 percent.

The accuracy of combined advancing contact line angle and receding contact line angle measurement is within ± 3° angle. The error is measuring the area of meniscus that is in contact with the heated surface is estimated to be ± 8 percent. As a result, the error in measuring the heat transfer coefficient is estimated to be ± 10 percent. The error in measuring the heat flux is estimated to be ± 11 percent.

7. Theoretical Analysis

The heat transfer in the meniscus region is presented by Kandlikar and Kuan (2003). The details are given in this section. It is modeled as consisting of three main features:

1. transient heat conduction between the water and the heater surface,
2. evaporation of water along the receding liquid-vapor interface, and
3. recirculation and mixing of the unevaporated water behind the advancing liquid-vapor interface with the incoming water

The recirculated and fresh incoming water streams are mixed as they flow behind the advancing liquid-vapor interface. The temperature of this mixed stream depends on the recirculation rate and the temperature of the incoming water. Since only a fraction of the water stream flowing behind the receding interface is evaporated, the water temperature of the mixed stream is expected to be close to the saturation temperature of the water.

Figure 12 identifies different flow regions considered in the present model. The inlet stream is identified as stream **A**, the mixed stream is identified as stream **B**, while stream **C** represents the water flowing over the heater surface encountering transient heat conduction, stream **D** is the fluid flow behind the receding interface, and stream **E** represents the evaporating water. Since the meniscus is stable, the inlet and the evaporating streams, **A** and **E** are equal.

The transient heat transfer between the heater surface and water is dictated by the relative thermal diffusivities of water and the heated copper block. The instantaneous temperature of the interface of two semi-infinite solids is given by:

$$T_{i,S-W} = \frac{\left(k\rho c_p\right)_S^{1/2} T_{S,i} + \left(k\rho c_p\right)_W^{1/2} T_{W,i}}{\left(k\rho c_p\right)_S^{1/2} + \left(k\rho c_p\right)_W^{1/2}} \quad (1)$$

For an initial surface temperature of copper block of 108 °C, and a water temperature of 100 °C, using equation (1) we obtain $T_{i,S\text{-}W}$= 107.65 °C. Because of the large thermal diffusivity of copper, the surface temperature is found to be close to the initial temperature of the copper block. With the large copper block, heat transfer under the meniscus will be three-dimensional in the copper block; the interface temperature will be even closer to $T_{S,i}$. Therefore, the interface temperature is taken as the same as the initial temperature of the copper block and the transient heat transfer is modeled as the semi-infinite medium in water coming in contact with a constant temperature of the heater surface. The resulting instantaneous heat flux at time t after initial contact is given by:

$$q'' = \frac{k\left(T_S - T_{W,i}\right)}{\sqrt{\pi \alpha t}} \quad (2)$$

As water flows over the heater surface from the advancing contact point to the receding contact point, the heat transfer is modeled as transient conduction in water. The time over which water contacts the heater surface is given by

$$t_{\max} = \frac{L}{V} \quad (3)$$

where L is the length of the meniscus along the heater surface in the flow direction, and V is the relative velocity between the meniscus and the heater surface.

The average heat flux between the meniscus and the heater surface is found by integrating equation (2) and dividing by $t_{max.}$ The resulting heat flux is the average heat flux over the heater surface area covered by the meniscus and is given by:

$$q''_m = \frac{2k(T_S - T_{W,i})}{\sqrt{\pi \alpha_{water} t_{max}}} \qquad (4)$$

One of the unknowns in equation (4) is the initial liquid temperature, $T_{W,i}$.

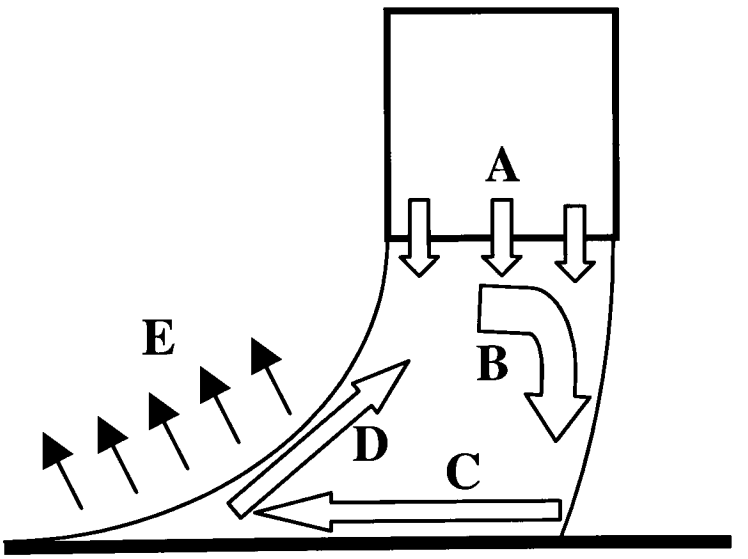

Figure 12: Identifying various streams in a meniscus flowing over a moving heater surface, **A** – fresh water inlet, **B** – recirculating mixed stream, **C** – water stream in transient heat conduction with the heater surface, **D** – water stream flowing behind the receding interface, and **E** – evaporating water stream, Kandlikar and Kuan (2003).

8. Results and Discussion

8.1 Contact Line Angles

The contact angles and heat transfer results for stationary and moving menisci are presented in this section. For the stationary meniscus, the contact angles are representative of the equilibrium contact angle. These are expected to fall between the advancing and the receding contact angle values. For the stationary meniscus, the contact angle was found to be almost independent of the flow rate and heat flux.

In the case of the rotating heater, the moving meniscus presents dynamic advancing and dynamic receding contact angles. As mentioned earlier, these are measured from the images obtained with the high speed camera. These images are transported into PRO-Engineering software program and then the respective angles are measured. These angles are plotted in Figures 13 18. Also, the images that are being transported into PRO-Engineering software program can be found in the Appendix C.

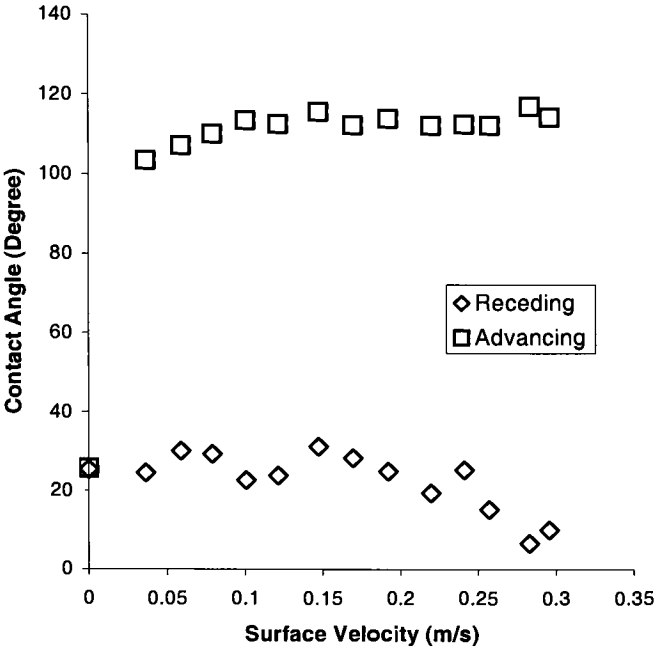

Figure 13: Plot of receding and advancing contact angles verses surface velocity at 2.7E-07 kg/s and surface temperature of 105.5°C

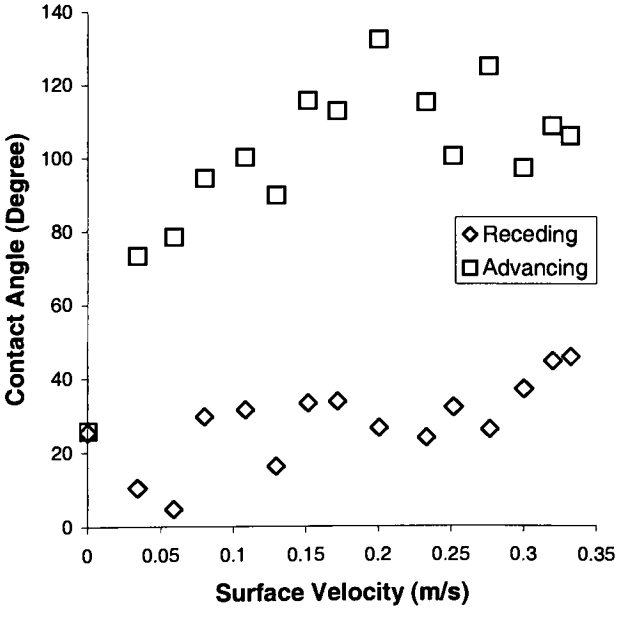

Figure 14: Plot of receding and advancing contact angles verses surface velocity at 2.7E-07 kg/s and surface temperature of 108°C

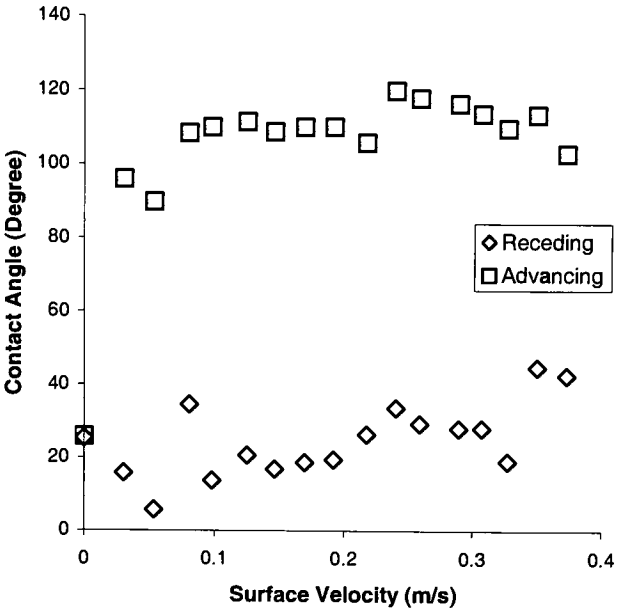

Figure 15: Plot of receding and advancing contact angles verses surface velocity at 2.7E-07 kg/s and surface temperature of 102.5°C

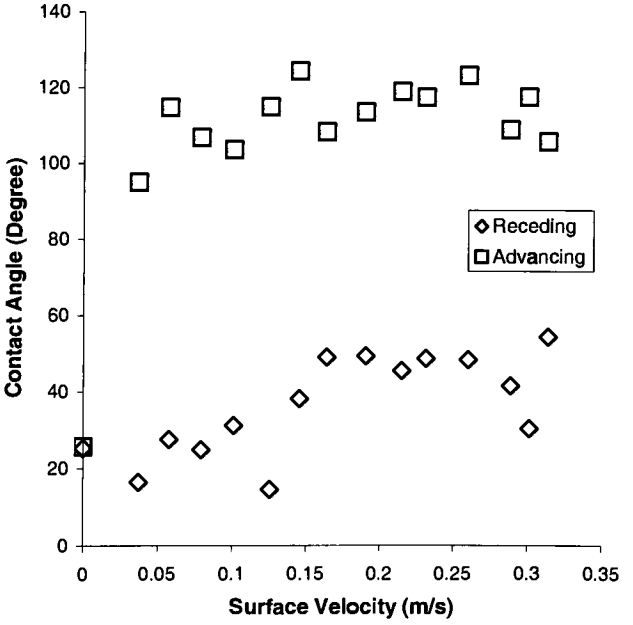

Figure 16: Plot of receding and advancing contact angles verses surface velocity at 3.6E-07 kg/s and surface temperature of 107.0 °C

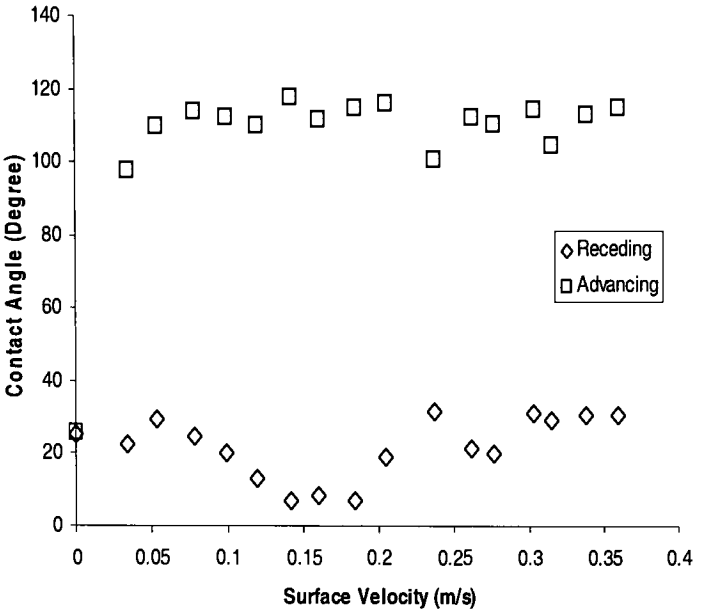

Figure 17: Plot of receding and advancing contact angles verses surface velocity at 3.3E-07 kg/s and surface temperature of 107.0 °C

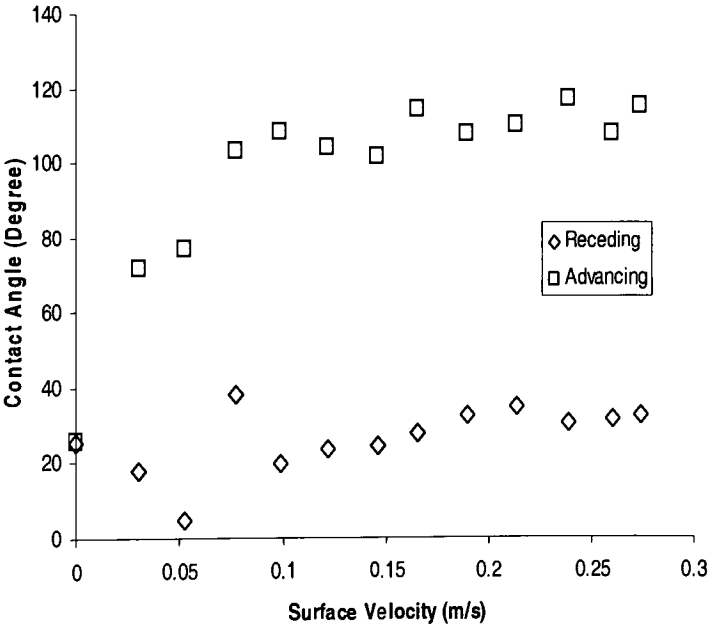

Figure 18: Plot of receding and advancing contact angles verses surface velocity at 4.1E-07 kg/s and surface temperature of 107.0 °C

Figures 13-15 show plots of the advancing and receding contact angles as a function of the relative surface velocity. The water mass flow rate is at a constant value of 2.7E-07 kg/s for Figures 13-15, and the surface temperatures are 105.5°C, 108°C, and 102.5°C respectively. The zero velocity point corresponds to the stationary meniscus. In Figure 13, as the surface velocity increases, the receding contact angle remains almost constant in the beginning and then decreases for higher velocities. The advancing contact angle is seen to be almost constant at an angle of 110°. Figure 14 shows that the advancing contact angle increases as the surface velocity increases. But at higher surface velocities, the advancing contact angle decreases with increasing surface velocities. The receding contact angle drops to a lower value and then remains almost constant for higher velocities. The advancing contact angle in Figure 15 is similar to that in Figure 13, but in Figure 15 the receding contact angle is again seen to drop to a lower value and then remain almost constant for higher velocities. Figures 16-18 also show the plots of the advancing and receding contact angles as a function of the relative surface velocity. The water mass flow rate is set at values of 3.6E-07 kg/s, 3.3E-07 kg/s, and 4.1E-07 kg/s respectively. The surface temperature is at a constant value of 107°C for Figures 16-18. It was difficult to accurately measure the lower contact angle values. The advancing contact angle does not change appreciably with the relative surface velocity except in Figure 14. In this case, the surface temperature is 108.0 °C, which is the highest in these tests. The interface is observed to become somewhat unstable leading to scatter in the contact angles measurements as seen in Figure 14.

8.2 Heat Transfer Results

The heat transfer results for stationary and moving menisci are presented in this section. The heat transfer rates in terms of heat flux and heat transfer rate per unit contact line length is calculated as follows: The surface heat flux under the meniscus area is calculated from the known water flow rate and the inlet temperature. Heat transferred in this region goes in heating the water from its inlet temperature to the saturation temperature corresponding to the atmospheric pressure, and then evaporating it into steam. Thus q" is given by:

Heat Flux Calculation:

$$q'' = \frac{\left[\dot{m} h_{fg} + \dot{m} C_p (T_{sat} - T_{in})\right]}{A} \qquad (5)$$

where A is the footprint area of the meniscus.

The inlet temperature of water T_{in} is 21°C for all tests. The area for stationary meniscus is πr^2 where r is the radius of the wetted region under the meniscus, and for the moving meniscus, the rectangular surface area is calculated from the measured length and width of the meniscus. The calculated heat flux values and the images that are used in measuring the length and width of menisci are included in Appendix B and Appendix C respectively. Please note that the outer diameter and inner diameter of the dispensing needle is 1.65 mm and 1.08 mm respectively, and it is used as a scale for calibration purpose in the vision software.

The heat transfer rate per unit length of the meniscus is calculated using only the latent heat part as the sensible heating is believed to take place in the inside region of the meniscus, while evaporation occurs at the interface.

Heat Transfer Per Unit Contact Line Length Calculation:

$$q' = \frac{\left(\dot{m} h_{fg} \right)}{P} \qquad (6)$$

where P is the length of the interline (junction of solid-liquid-vapor).

The heat transfer results are presented in terms of the measured heat flux as a function of surface velocity. Figures 19-21 show this variation for three different heater surface temperatures at a constant mass flow rate of 2.7E-07 kg/s. It can be seen that there is a systematic dependence of heat flux on the surface velocity and surface temperature. At lower velocities, the heat flux is relatively insensitive to velocity, but it increases almost linearly with velocity at higher velocities.

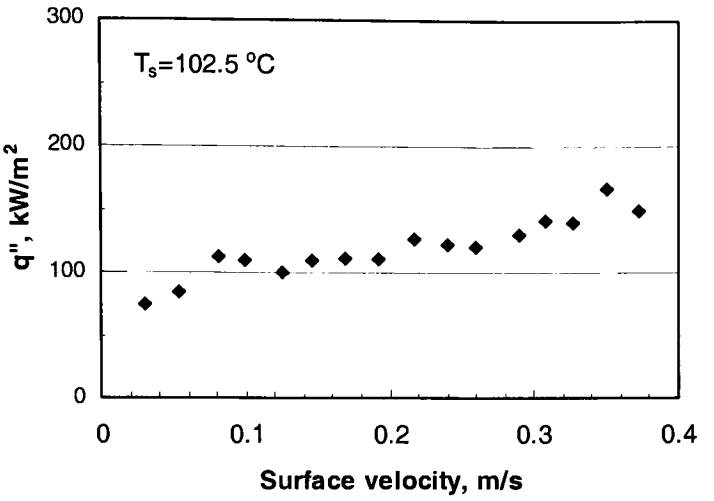

Figure 19: Variation of measured heat flux with surface velocity for heater surface temperature of 102.5 °C at mass flow rate of 2.7E-07 kg/s

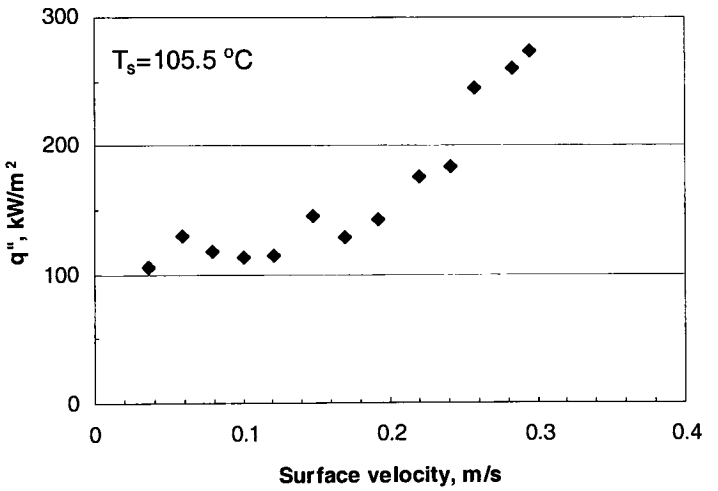

Figure 20: Variation of measured heat flux with surface velocity for heater surface temperature of 105.5 °C at mass flow rate of 2.7E-07 kg/s

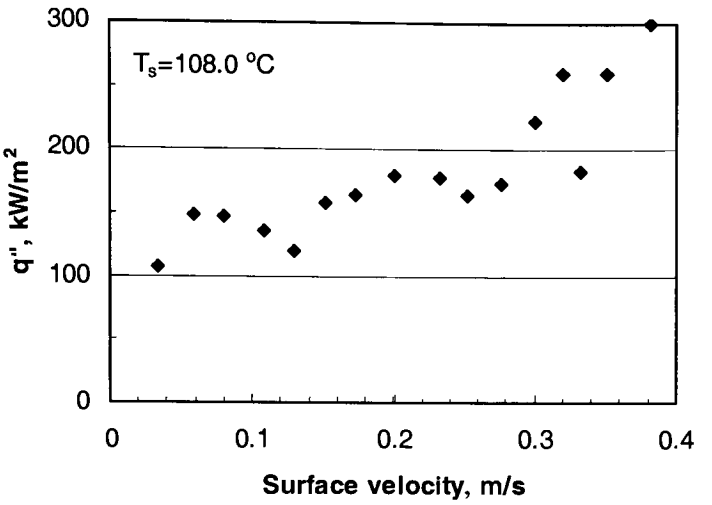

Figure 21: Variation of measured heat flux with surface velocity for heater surface temperature of 108.0 °C at mass flow rate of 2.7E-07 kg/s

Figures 22-24 show the measured heat flux as a function of surface velocity for three different water mass flow rates at a constant surface temperature of 107°C. It can also be seen that there is a systematic dependence of heat flux on the surface velocity and water mass flow rate. At lower velocities, the heat flux is also relatively insensitive to velocity, but it increases almost linearly with velocity at higher velocities.

As the surface velocity increases, the transient conduction process becomes more efficient, but the mixed stream temperature also increases as the recirculated stream becomes larger. In addition, the complex fluid flow behavior behind the receding interface, not modeled in this study, plays an important role.

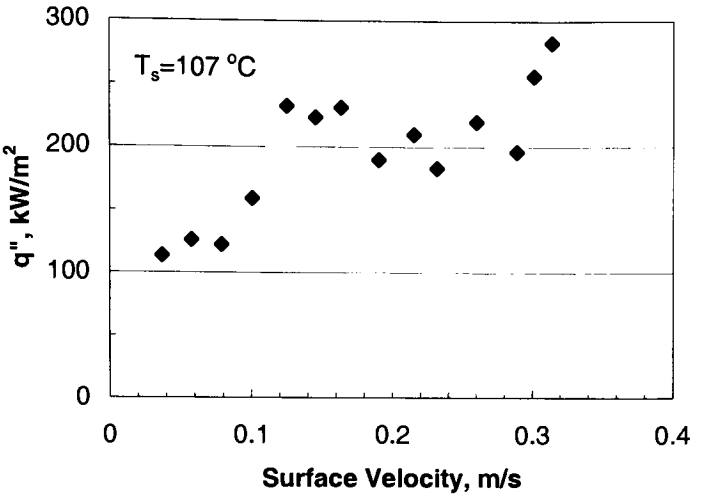

Figure 22: Variation of measured heat flux with surface velocity for heater surface temperature of 107 °C at a mass flow rate of 3.55E-07 kg/s

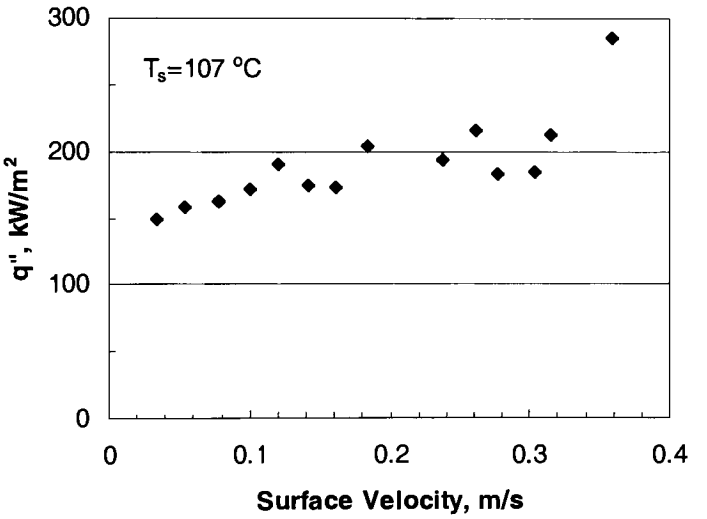

Figure 23: Variation of measured heat flux with surface velocity for heater surface temperature of 107 °C at a mass flow rate of 3.29E-07 kg/s

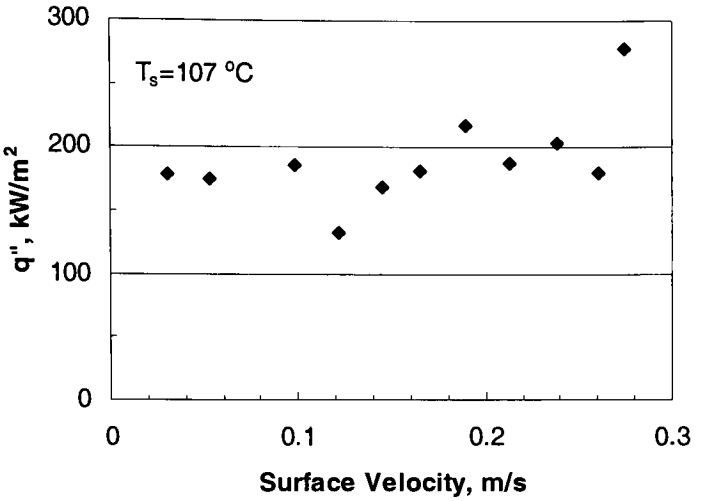

Figure 24: Variation of measured heat flux with surface velocity for heater surface temperature of 107 °C at a mass flow rate of 4.08E-07 kg/s

8.3 Calculated Initial Water Temperature

Figures 25-30 show the variation of the calculated initial water temperature of the stream **C** at the beginning of the transient conduction phase. Equation (4) is used with the measured value of heat flux in calculating $T_{W,i}$. The calculated values $T_{W,I}$ is shown in Appendix B. In general, as the surface velocity increases, $T_{W,i}$ increases and then becomes somewhat flat. Only for the surface temperature of 105.5°C shown in Figure 26, $T_{W,i}$ drops off beyond a velocity of about 0.2 m/s. Since the heat flux and recirculation patterns are complex functions of the meniscus shape as well as the evaporation characteristics in the meniscus region, it is difficult to draw any specific conclusions from this observation at this stage.

Experimental verification of $T_{W,i}$ was not readily possible due to small gaps between the needle and the heater surface. However, a small thermocouple, 0.5 mm diameter was fabricated and the temperature of the water stream as it enters the transient heating zone was measured. For a wall temperature of 105.5 °C, a flow rate of 2.7E-7 kg/s, and surface velocities of 0.036 m/s and 0.079 m/s, temperatures of 90 °C and 88 °C were recorded respectively. Looking at Figure 26, these values are in close agreement with the calculated values of 87 °C and 93 °C respectively using equation (4) and the measured heat flux. As the measured values suggest, the transient heat conduction plays a major role in the heat transfer process from a moving meniscus.

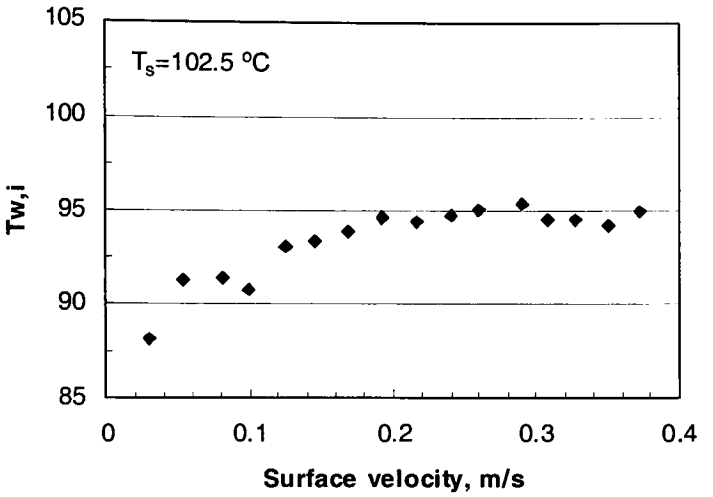

Figure 25: Variation of calculated initial water temperature with surface velocity for heater surface temperature of 102.5 °C at mass flow rate of 2.7E-07 kg/s

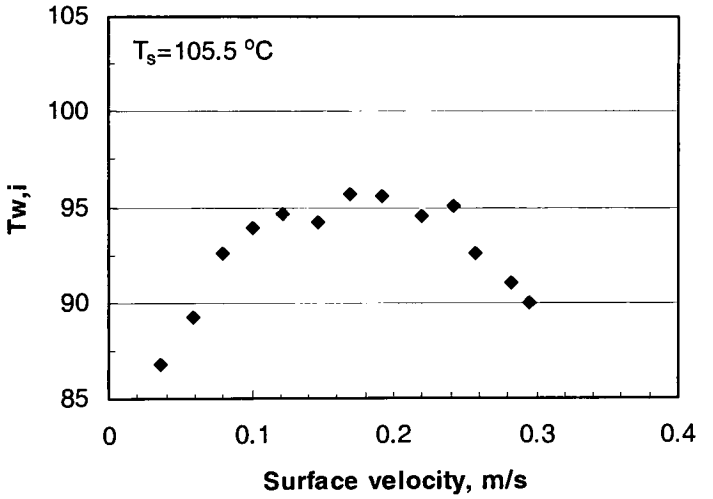

Figure 26: Variation of calculated initial water temperature with surface velocity for heater surface temperature of 105.5 °C at mass flow rate of 2.7E-07 kg/s

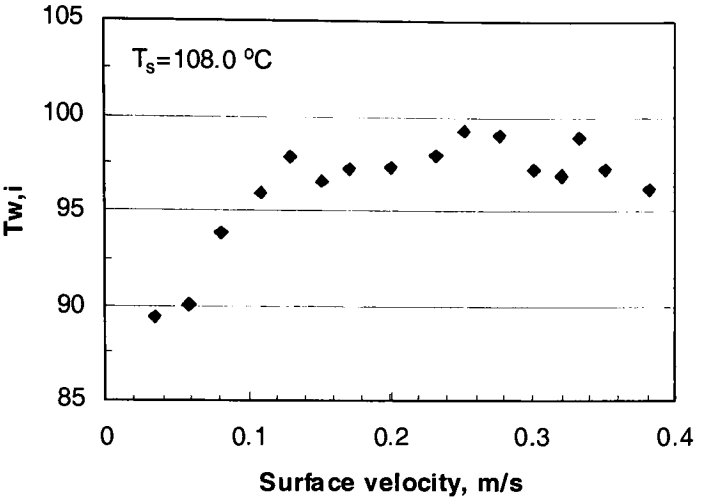

Figure 27: Variation of calculated initial water temperature with surface velocity for heater surface temperature of 108.0 °C at mass flow rate of 2.7E-07 kg/s

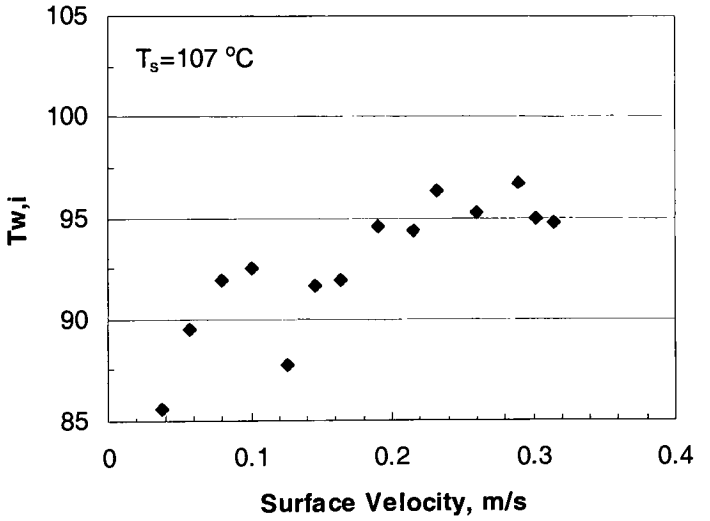

Figure 28: Variation of calculated initial water temperature with surface velocity for heater surface temperature of 107°C at a mass flow rate of 3.55E-07 kg/s

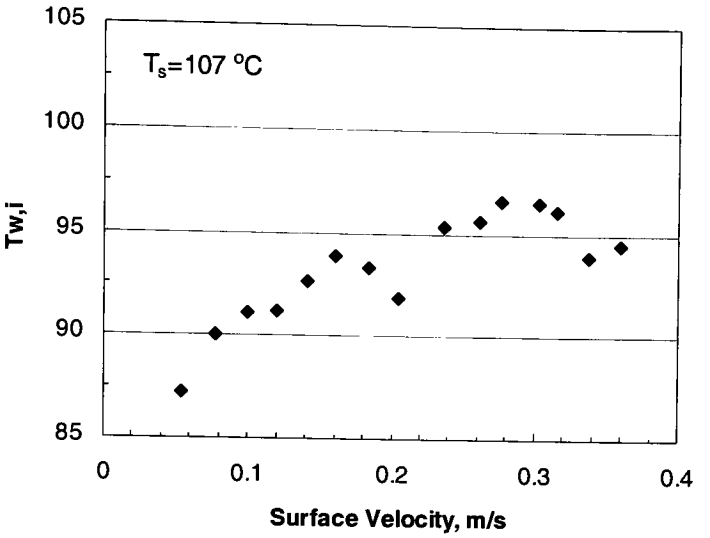

Figure 29: Variation of calculated initial water temperature with surface velocity for heater surface temperature of 107°C at a mass flow rate of 3.29E-07 kg/s

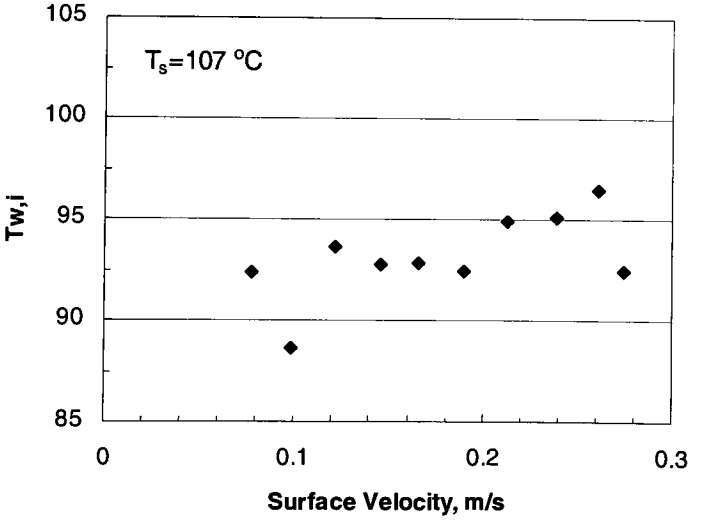

Figure 30: Variation of calculated initial water temperature with surface velocity for heater surface temperature of 107°C at a mass flow rate of 4.08E-07 kg/s

8.4 Breaking of a Meniscus

The breaking of a meniscus from the dispensing needle is shown in Figure 31. As the flow rate decreases, or as the surface velocity increases, the meniscus is breaks down and is pulled along the heater surface. In this case, the evaporation rate of water is not high enough to maintain the shape of the meniscus like the one in frame (a). It is interesting to note that as the meniscus breaks off, the water droplet traveling along with the heater surface does not evaporate as rapidly, thereby indicating that the heat transfer rate is low for stationary droplets.

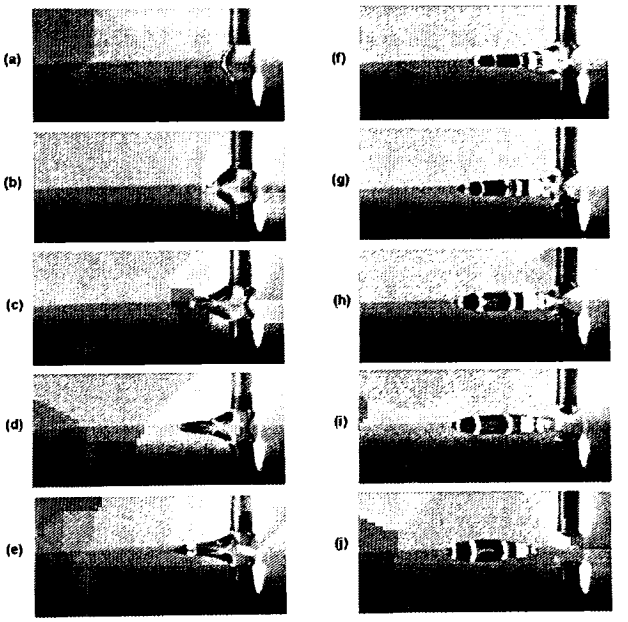

Figure 31: Pictures of Meniscus Breaking

8.5 Comparison with Bubble Dynamics in Pool Boiling

The interfacial velocity reported by Hahne (1977) for saturation pressure of atmospheric conditions is 0.08 m/s. Other reported interfacial velocities for saturation pressures of 0.1 bar, 0.2 bar, 8.0 bar, and 15 bar are 1.889 m/s, 2 m/s, 0.0375 m/s, and 0.008 m/s respectively. The excess temperature is 8.5 K for the reported interfacial velocity at 1 bar. Looking at Table 4, for the relative surface velocity of 0.08 m/s and with similar excess temperature, the experimentally obtained heat flux value is 146.5 kW/m^2. The heat flux values taken from the boiling curve (Figure 29) in Appendix B for 108 °C is 60 kW/m^2. Thus, the advancing and receding motion of the meniscus provides heat transfer rates that are higher than the nucleate boiling values.

9. Conclusions

An experimental investigation is conducted to study the characteristics of an evaporating meniscus on a smooth heated surface. The heat transfer characteristics are also investigated for both stationary and moving menisci. The study provides an important insight on the role of transient conduction around a nucleating bubble in pool boiling. The following conclusions are drawn from the present study.

1. For the stationary meniscus, the contact angle is almost independent of the water flow rate and the heat flux in the range of parameters investigated. It is seen to be almost constant at an angle of 26° for deionized water on polished copper surface (average surface roughness of 0.04 μm).
2. In the case of a moving meniscus, as the surface velocity increases, the receding contact angle drops to a lower value and then remains almost constant for higher velocities.
3. The advancing contact angle in a case of a moving meniscus does not change appreciably with the relative surface velocity. It is seen to be almost constant at an angle of 110°. Figure 14, the case of surface temperature of 108°C with the water mass flow rate of 2.7E-7 kg/s shows some changes in the advancing contact angle with the relative surface velocity. This inconsistency with the rest of the plots might be caused by instabilities and experimental uncertainties.
4. There is a systematic dependence of heat flux on the surface velocity and surface temperature as seen from Figures 19–21. At lower velocities, the heat flux is relatively insensitive to velocity, but it increases somewhat linearly with velocity at higher velocities. In the same figures, for the range of relative surface velocities

investigated, the average heat flux increases with increasing surface temperature. The average heat flux values are 120 kW/m^2, 164 kW/m^2 and 182 kW/m^2 for surface temperatures of 102.5 °C, 105.5 °C and 108 °C respectively.

5. Since the heat flux and recirculation patterns are complex functions of the meniscus shape as well as the evaporation characteristics in the meniscus region, it is difficult to draw any specific conclusions from this observation at this stage.
6. For a wall temperature of 105.5 °C, a flow rate of 2.7E-7 kg/s, and a surface velocities of 0.036 m/s and 0.079 m/s, the experimental verification of $T_{w,I}$ is in close agreement with the calculated value using equation (4) and the measured heat flux.
7. The advancing and receding motion of the meniscus provides heat transfer rates that are higher than the nucleate boiling values. The average heat flux values for surface temperatures of 105.5 °C and 108 °C are 164 kW/m^2 and 182 kW/m^2 respectively, while the heat flux values taken from the boiling curve (Figure 36) in Appendix B for 105.5 °C and 108 °C are 13 kW/m^2 and 60 kW/m^2 respectively.

10. References

1. DasGupta, S., Schonberg, J.A., and Wayner, P.C., 1993, "Investigation of an Evaporating Extended Meniscus Based on the Augmented Young-Laplace Equation," Journal of Heat Transfer, Vol. 115, pp. 201-208.
2. Derjaguin, B.V., 1940, "A Theory of Capillary Condensation in the Pores of Sorbents and Other Capillary Phenomena Taking into Account the Disjoining Action of Polymolecular Liquid Films," *Acta Physiocochimica* (USSR), Vol. 12, No. 1, pp. 181-200.
3. Derjaguin, B.V., Nerpin, S.V., and Churaev, N.V., 1965, "Effect of Film Transfer upon Evaporating Liquids from Capillaries," RILEM Bulletin, Vol. 29, No. 1, pp. 93-98.
4. Hahne, E., and Grigull, U., 1977, Nucleate Boiling: Bubble Growth and Dynamics, Chapter 2, Section 3.1, in *Heat Transfer in Boiling.*
5. Hallinan, K.P., and Chebaro, H.C., Kim, S.J., and Chang, W.S., 1994, "Evaporation from an Extended Meniscus for Non-isothermal Interfacial Conditions," *Journal of Thermophysics and Heat Transfer*, Vol. 8, No. 4, 709-716.
6. Holm, F.W., Golpen, S. P., 1979, "Heat Transfer In The Meniscus Thin Film Transition Region," ASME Journal of Heat Transfer, Vol. 101, pp. 543-547.
7. Incropera, F. P., and DeWitt, D.P., 2002, Pool Boiling, Chapter 10, Section 10.3.2, in *Fundamentals of Heat and Mass Transfer.*
8. Kandlikar, S. G., and Kuan, W. K., 2003, "Circular Evaporating Meniscus – A New Way to Study Heat Transfer Mechanism During Nucleate Boiling," 5th International Conference on Boiling Heat Transfer 2003, Jamaica, May 4-8.

9. Kandlikar, S. G., and Kuan, W. K., 2003, "Heat Transfer from a Moving and Evaporating Meniscus on a Heated Surface," ASME Summer Heat Transfer Conference 2003, Las Vegas, July 20-23.

10. Kandlikar, S. G., Steinke, M. E., and Balasubramanian, P., 2002, "Single-Phase Flow Characteristics and Effect of Dissolved Gases on Heat Transfer Near Saturation Conditions in Microchannels," ASME International Mechanical Engineering Congress and Exposition, New Orleans, November 17-22.

11. Khrustalev, D; Faghri, A., 1996, "Fluid Flow Effects In Evaporation From Liquid Vapor Meniscus," Journal of Heat Transfer, 118, no. 3, pp. 725-731.

12. Kim, I Y, Wayner Jr., P.C. 1996, "Shape Of An Evaporating Completely Wetting Extended Meniscus," Journal of Thermophysics And Heat Transfer, 10, no. 2, pp. 320-326.

13. Lay, J.H., and Dhir, V.K., 1995, "Shape of a Vapor Stem During Nucleate Boiling of Saturated Liquids," ASME Journal of Heat Transfer, Vol. 117, pp. 394-401.

14. Nikolayev, V.S., and Beysens, D.A., 1999, "Boiling Crisis and Non-equilibrium Drying Transitions," Europhysics Letters, Vol. 47, No. 3, pp. 345-351.

15. Pierret, R.F., 1996, Semiconductor Device Fundamentals, solutions manual, Addison-Wesley, Reading, MA, pp. 6.12

16. Potash, M., Jr., and Wayner, P. C., Jr., 1972, "Evaporation From A Two-Dimensional Extended Meniscus", Int. J. Heat Mass Transfer, vol. 15, pp. 1851-1863.

17. Schonberg, J.A., 1995, "An Augmented Young-Laplace Model of an Evaporating Meniscus in a Microchannel with High Heat Flux," Experimental Thermal and Fluid Science 1995, Elsevier Science Inc., New York, NY, pp. 163-170.

18. Sefiane, K., Benielli, D., and Steinchen, A., 1998, "A New Mechanism for Pool Boiling Crisis, Recoil Instability, and Contact Angle Influence," Colloids and Surfaces, A: Physiochemical and Engineering Aspects, Vol. 142, pp. 361-373.

19. Shoji, M., Mori, Y.H., and Maruyama, S., 1999, Representation of Solid-liquid-vapor Phase Interactions, Chapter 6, Section 2.2.6, in *Handbook of Phase Change – Boiling and Condensation,* eds. Kandlikar, S.G., Shoji, M., and Dhir, V.K., Taylor and Francis, Philadelphia, PA.

20. Son, G., and Dhir, V.K., and Ramanajapu, N, 1999, "Dynamics and Heat Transfer Associated with a Single Bubble during Nucleate Boiling on a Horizontal Surface," ASME Journal of Heat Transfer, Vol. 121, pp 623-631.

21. Swanson, L. W., Herdt, G. C., 1992, "Model Of The Evaporating Meniscus in a Capillary Tube", Journal of Heat Transfer, 114, no. 2, pp. 434-441.

22. Sujanani, M., Wayner, P.C., Jr., 1992, "Transport Processes And Interfacial Phenomena In An Evaporating Meniscus", Chemical Engineering Communications, 118, pp. 89.

23. Wayner, P.C. Jr., 1978, "The Effect of Thin Film Heat Transfer on Meniscus Profile and Capillary Pressure," AIAA Journal, Vol. 17, No. 7, pp. 772-776.

24. Wayner, P.C., Jr., 1991, "The Effect of Interfacial Mass Transport in Thin Liquid Films," Colloids and Surfaces, Vol. 52, pp. 71-84.

25. Wayner, P.C., Jr., 1992, "Evaporation and Stress in the Contact Line Region," Proceedings of the conference on Pool and External Flow Boiling, Engineering Foundation, Dhir, V.K., and Bergles, A.E., editors, Santa Barabra, CA, p. 251-256.

26. Wayner, P.C., Jr., 1994, "Thermal and Mechanical Effects in the Spreading of a Liquid Film Due to a Change in the Apparent Finite Contact Angle," Transactions of the ASME, Journal of Heat Transfer, Vol. 116, No. 116, pp. 938-945.

27. Wayner, P.C., Jr., DasGupta, S., and Schonberg, J.F., 1991, "Effect of Interfacial Forces on Evaporating Heat Transfer in a Meniscus," *Technical Report WL-TR-91*, Wright-Patterson AFB, Ohio.

28. Wayner, P.C. Jr., Kao, Y.K., and Lacroix, L.V., 1976, "The Interline Heat Transfer Coefficient of an Evaporating Wetting Film," *International Journal of Heat and Mass Transfer,* Vol. 19, No.2, pp. 487-492.

Appendix A (Photographs of Meniscus Testing Experiments)

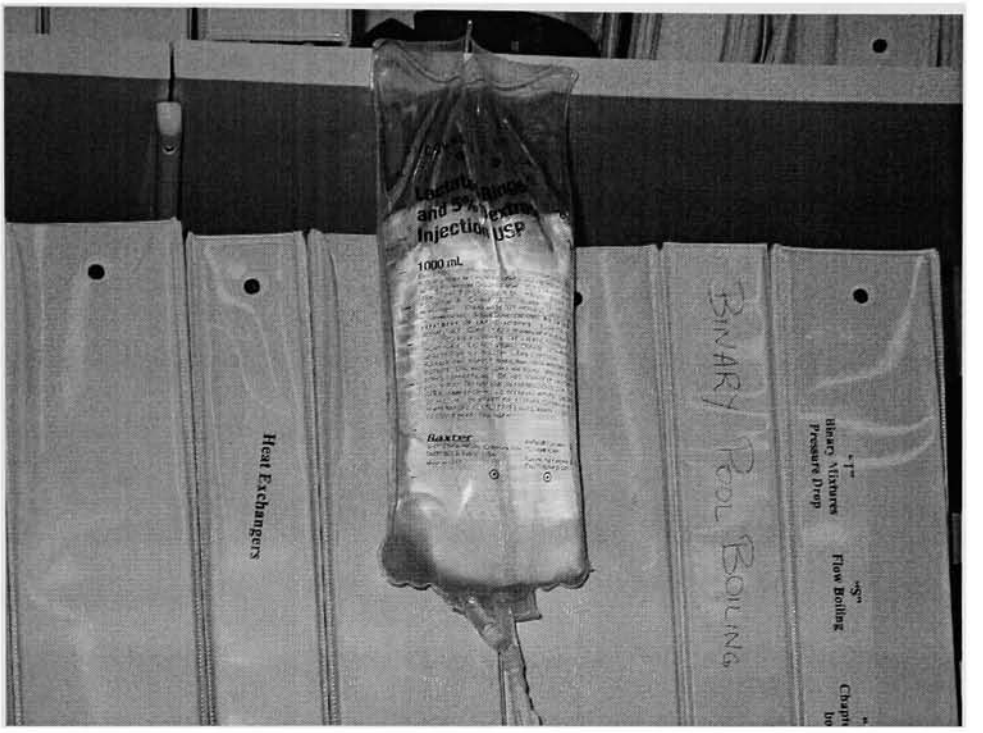

Figure 32: Water Pouch

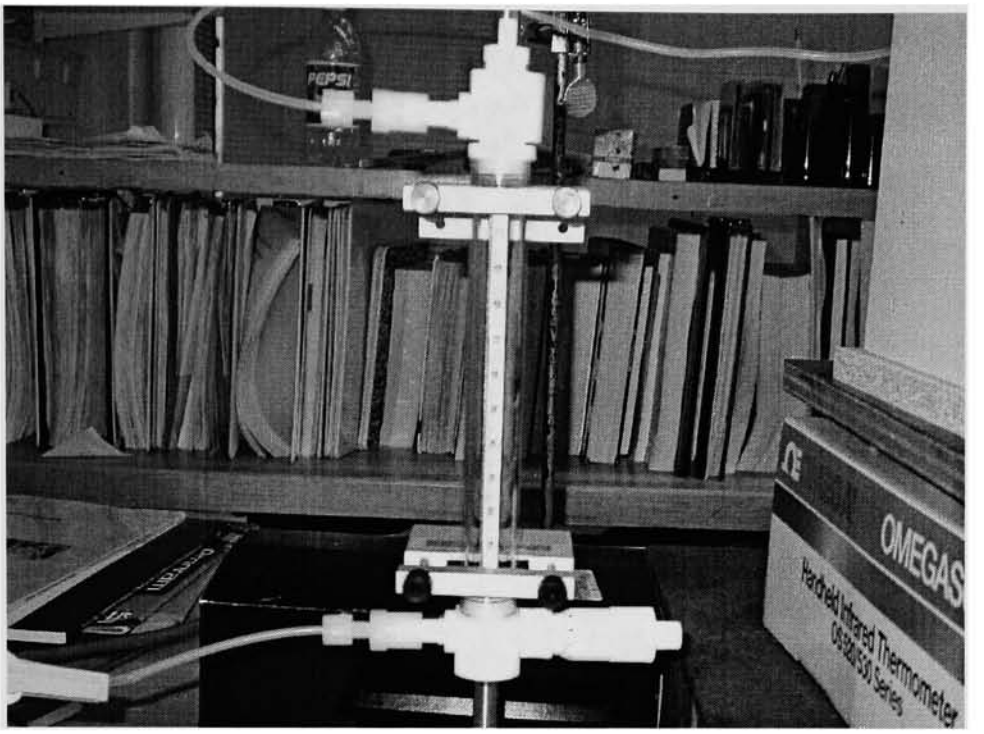

Figure 33: Flowmeter

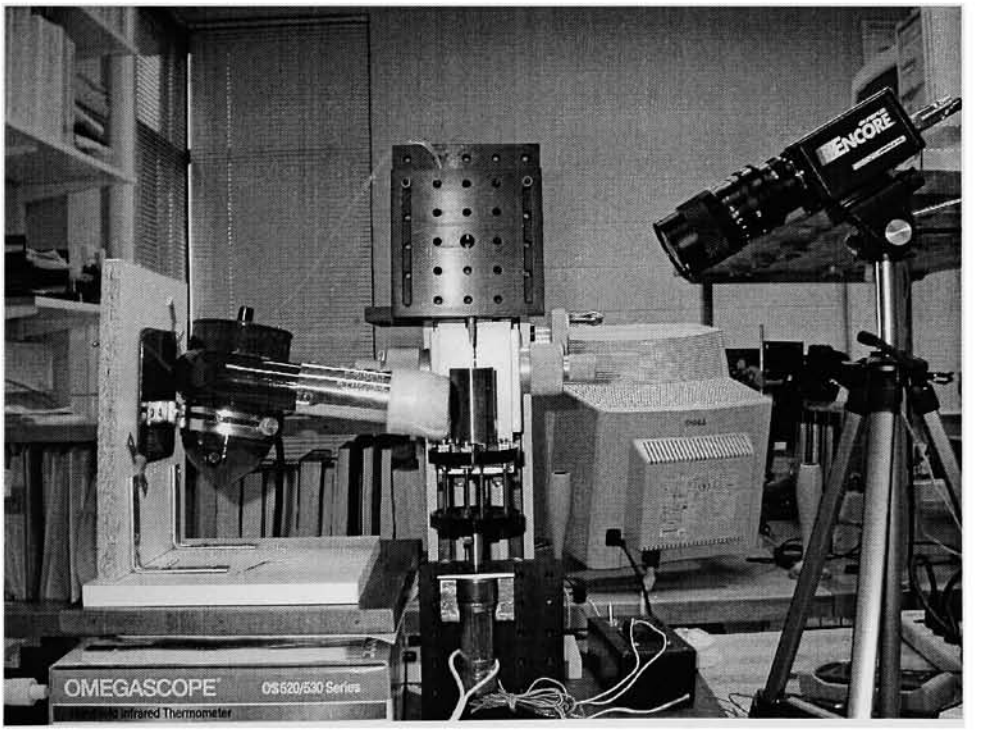

Figure 34: Front View of the Experimental Setup

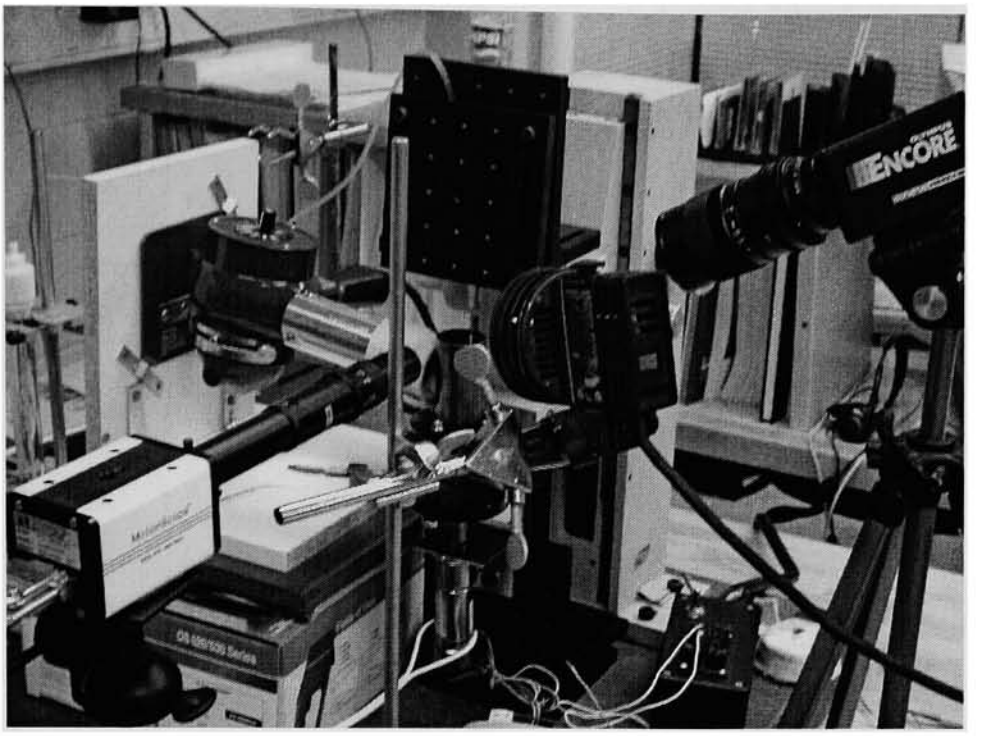

Figure 35: Side View of the Experimental Setup

Appendix B

Table 2: Calculated heat flux and initial water temperature for surface temperature of 102.5 °C and mass flow rate of 2.7E-07 kg/s

File Name	Temperature, C	Distance_needle center to edge, m	RPS	Surface Velocity, m/s	Surface Temperature, K	hfg (kJ/kg)	Mass Flow Rate, kg/s	q=mhfg (W)	Area, m^2	Width, m	Length, m	q", W/m^2	Theta, adv	Theta, rec	t	t*-1/2	Ti	q calc	Tcalc
14_105.5C_2V	105.5	0.006325	0.47244	0.038453781	379	2241.6	2.69629E-07	0.604400345	6.60387E-06	0.001606	0.004112	105.2961628	103.69	24.5377	0.1128	2.9775	90	87291.6	86.803
14_105.3C_2.5V	105.3	0.006101	0.75	0.058926068	379	2241.6	2.69629E-07	0.604400345	5.3707E-06	0.001651	0.003253	129.4732517	107.4801	30.1545	0.0552	4.2561	90	123168	89.2168
14_105.5C_3V	105.5	0.006227	1.0169	0.079090831	379	2241.6	2.69629E-07	0.604400345	5.90129E-06	0.001722	0.003427	117.8321875	110.556	29.493	0.04333	4.804	90	140843	92.5323
14_105.5C_3.5V	105.5	0.006329	1.302	0.100430453	379	2241.6	2.69629E-07	0.604400345	6.1087E-06	0.001651	0.0037	113.8314832	114.0224	22.8198	0.03684	5.2099	90	152742	93.9486
14_105.5C_4V	105.5	0.006403	1.5823	0.121315841	379	2241.6	2.69629E-07	0.604400345	6.04338E-06	0.001562	0.003869	115.0618713	113.1412	23.9144	0.03189	5.5996	90	164168	94.6363
14_105.4C_4.5V	105.4	0.006225	1.8939	0.147324541	379	2241.6	2.69629E-07	0.604400345	4.79979E-06	0.001517	0.003184	144.8735614	116.4207	31.4666	0.02148	6.8237	90	198763	94.1753
14_105.3C_5V	105.3	0.0063	2.1929	0.169550065	379	2241.6	2.69629E-07	0.604400345	5.41619E-06	0.001586	0.003415	128.3858914	113.1586	28.4893	0.02014	7.0462	90	203911	95.6669
14_105.4C_5.5V	105.4	0.006365	2.5	0.192273324	379	2241.6	2.69629E-07	0.604400345	4.87705E-06	0.001477	0.003302	142.5783642	114.7165	25.0789	0.01717	7.6308	90	222274	95.5216
14_105.6C_6V	105.6	0.006294	2.84	0.219689438	379	2241.6	2.69629E-07	0.604400345	0.000003936	0.00128	0.003075	176.6672717	113.1265	19.6121	0.014	8.4524	90	249404	94.5496
14_105.6C_6.5V	105.6	0.006315	3.125	0.241323403	379	2241.6	2.69629E-07	0.604400345	3.78467E-06	0.001321	0.002865	183.7315539	113.6043	25.4414	0.01187	9.1778	90	270806	95.016
14_105.8C_7V	105.8	0.006477	3.378	0.257422561	379	2241.6	2.69629E-07	0.604400345	2.84285E-06	0.001058	0.002687	244.6007914	113.2376	15.3763	0.01044	9.7879	90	292511	92.5879
14_105.7C_7.5V	105.7	0.00635	3.676	0.283065151	379	2241.6	2.69629E-07	0.604400345	2.67624E-06	0.000826	0.00324	259.8281101	118.146	6.684	0.01145	9.347	90	277566	91.0033
14_105.6C_8V	105.6	0.006559	3.90625	0.295665593	379	2241.6	2.69629E-07	0.604400345	2.54435E-06	0.000736	0.003457	273.2964548	115.3561	10.1074	0.01169	9.2481	90	272880	89.9762

Table 3: Calculated heat flux and initial water temperature for surface temperature of 105.5 °C and mass flow rate of 2.7E-07 kg/s

File Name	Temperature, C	Distance_needle center to edge, m	RPS	Surface Velocity, m/s	Surface Temperature, K	hfg (kJ/kg)	Mass Flow Rate, kg/s	q=mhfg (W)	Area, m^2	Width, m	Length, m	q", W/m^2	Theta, adv	Theta, rec	t	t*-1/2	Ti	q calc	Tcalc
14_105.5C_2V	105.5	0.006325	0.47244	0.036453781	379	2241.6	2.69629E-07	0.604400345	6.60387E-06	0.001606	0.004112	105.2961628	103.69	24.5377	0.1128	2.9775	90	87291.6	86.803
14_105.3C_2.5V	105.3	0.006101	0.75	0.058926068	379	2241.6	2.69629E-07	0.604400345	5.3707E-06	0.001651	0.003253	129.4732517	107.4801	30.1545	0.0552	4.2561	90	123168	89.2168
14_105.5C_3V	105.5	0.006227	1.0169	0.079090831	379	2241.6	2.69629E-07	0.604400345	5.90129E-06	0.001722	0.003427	117.8321875	110.556	29.493	0.04333	4.804	90	140843	92.5323
14_105.5C_3.5V	105.5	0.006329	1.302	0.100430453	379	2241.6	2.69629E-07	0.604400345	6.1087E-06	0.001651	0.0037	113.8314832	114.0224	22.8198	0.03684	5.2099	90	152742	93.9486
14_105.5C_4V	105.5	0.006403	1.5823	0.121315841	379	2241.6	2.69629E-07	0.604400345	6.04338E-06	0.001562	0.003869	115.0618713	113.1412	23.9144	0.03189	5.5996	90	164168	94.6363
14_105.4C_4.5V	105.4	0.006225	1.8939	0.147324541	379	2241.6	2.69629E-07	0.604400345	4.79979E-06	0.001517	0.003164	144.8735614	116.4207	31.4666	0.02148	6.8237	90	198763	94.1753
14_105.3C_5V	105.3	0.0063	2.1929	0.169550065	379	2241.6	2.69629E-07	0.604400345	5.41619E-06	0.001586	0.003415	128.3858914	113.1586	28.4893	0.02014	7.0462	90	203911	95.6669
14_105.4C_5.5V	105.4	0.006365	2.5	0.192273324	379	2241.6	2.69629E-07	0.604400345	4.87705E-06	0.001477	0.003302	142.5783642	114.7165	25.0789	0.01717	7.6308	90	222274	95.5216
14_105.6C_6V	105.6	0.006294	2.84	0.219689438	379	2241.6	2.69629E-07	0.604400345	0.000003936	0.00128	0.003075	176.6672717	113.1265	19.6121	0.014	8.4524	90	249404	94.5496
14_105.6C_6.5V	105.6	0.006315	3.125	0.241323403	379	2241.6	2.69629E-07	0.604400345	3.78467E-06	0.001321	0.002865	183.7315539	113.6043	25.4414	0.01187	9.1778	90	270806	95.016
14_105.8C_7V	105.8	0.006477	3.378	0.257422561	379	2241.6	2.69629E-07	0.604400345	2.84285E-06	0.001058	0.002687	244.6007914	113.2376	15.3763	0.01044	9.7879	90	292511	92.5879
14_105.7C_7.5V	105.7	0.00635	3.676	0.283065151	379	2241.6	2.69629E-07	0.604400345	2.67624E-06	0.000826	0.00324	259.8281101	118.146	6.684	0.01145	9.347	90	277566	91.0033
14_105.6C_8V	105.6	0.006559	3.90625	0.295665593	379	2241.6	2.69629E-07	0.604400345	2.54435E-06	0.000736	0.003457	273.2964548	115.3561	10.1074	0.01169	9.2481	90	272880	89.9762
14_105.5C_8.5V	105.5	0.00643	4.3103	0.329741927	379	2241.6	2.69629E-07	0.604400345	3.56592E-06	0.001173	0.00304	195.0022382	117.646	18.1809	0.00922	10.415	90	305336	95.601
14_105.4C_9V	105.4	0.006422	4.6296	0.354401381	379	2241.6	2.69629E-07	0.604400345	3.56044E-06	0.001188	0.002997	195.3025925	111.0141	13.6075	0.00846	10.874	90	316753	95.9047

Table 4: Calculated heat flux and initial water temperature for surface temperature of 108.0 °C and mass flow rate of 2.7E-07 kg/s

File Name	Temperature, C	Distance_needle center to edge, m	RPS	Surface Velocity, m/s	Surface Temperature, K	hfg (kJ/kg)	Mass Flow Rate, kg/s	q=mhfg (W)	Area, m^2	Width, m	Length, m	q", W/m^2	Theta, adv	Theta, rec	t	t^-1/2	Ti	q calc	Tcalc
14_107.7C_2V	107.7	0.006365	0.44444	0.034181583	381.15	2235.78	2.69629E-07	0.602831104	6.50703E-06	0.001803	0.003609	106.6221395	73.3008	10.3921	0.10558	3.0775	90	103032	89.3832
14_107.7C_2.5V	107.7	0.006233	0.75949	0.059041773	381.15	2235.78	2.69629E-07	0.602831104	4.68989E-06	0.001568	0.002991	147.9338399	78.5412	4.7295	0.05066	4.443	90	148745	90.0965
14_107.7C_3V	107.7	0.006274	1.034479	0.08015257	381.15	2235.78	2.69629E-07	0.602831104	4.73535E-06	0.001857	0.00255	146.5135926	94.5636	29.7898	0.03181	5.6065	90	187697	93.8837
14_107.7C_3.5V	107.7	0.006197	1.38888	0.108283897	381.15	2235.78	2.69629E-07	0.602831104	5.08012E-06	0.00178	0.002854	136.5702268	100.2556	31.4578	0.02636	6.1596	90	206217	95.9779
14_107.9C_4V	107.9	0.006228	1.66666	0.129616358	381.15	2235.78	2.69629E-07	0.602831104	5.77703E-06	0.001777	0.003251	120.0951875	90	16.3082	0.02508	6.3142	90	213782	97.8444
14_108C_4.5V	108	0.006237	1.953125	0.151784331	381.15	2235.78	2.69629E-07	0.602831104	4.39142E-06	0.001549	0.002835	157.9885184	115.7332	33.2614	0.01868	7.3171	90	249118	96.5846
14_108.3C_5V	108.3	0.006115	2.19298	0.172105347	381.15	2235.78	2.69629E-07	0.602831104	4.21335E-06	0.001508	0.002794	184.665384	113.0089	33.7631	0.01623	7.8485	90	271663	97.2077
14_108.3C_5.5V	108.3	0.005818	2.5	0.20086558	381.15	2235.78	2.69629E-07	0.602831104	3.86687E-06	0.001429	0.002706	179.4196399	132.6266	26.6116	0.01347	8.6157	90	298220	97.2901
14_108.3C_6V	108.3	0.005523	2.84	0.233447352	381.15	2235.78	2.69629E-07	0.602831104	3.87803E-06	0.001386	0.002798	178.9035924	115.427	23.9554	0.01199	9.1342	90	316168	97.9449
14_108.4C_6.5V	108.4	0.005768	3.125	0.252063723	381.15	2235.78	2.69629E-07	0.602831104	4.23296E-06	0.001508	0.002807	163.9027527	100.5481	32.2041	0.01114	9.4762	90	329798	99.2556
14_108.3C_7V	108.3	0.005584	3.378	0.27680062	381.15	2235.78	2.69629E-07	0.602831104	3.99023E-06	0.001406	0.002838	173.873057	125.2569	26.208	0.01025	9.8759	90	341841	98.9919
14_107.8C_7.5V	107.8	0.005597	3.676	0.300457184	381.15	2235.78	2.69629E-07	0.602831104	3.11036E-06	0.001289	0.002413	223.059006	97.1903	37.0426	0.00803	11.159	90	375689	97.2316
14_107.8C_8V	107.8	0.005956	4.03226	0.320480608	381.15	2235.78	2.69629E-07	0.602831104	2.65593E-06	0.001338	0.001985	261.2241816	108.7795	44.6559	0.00619	12.706	90	427796	96.9308
14_107.5C_8.5V	107.5	0.005891	4.16667	0.332865098	381.15	2235.78	2.69629E-07	0.602831104	3.79439E-06	0.001427	0.002659	182.8469377	106.0736	45.8127	0.00799	11.189	90	370347	98.8599
14_107.8C_9V	107.8	0.006091	4.48429	0.351031241	381.15	2235.78	2.69629E-07	0.602831104	2.66305E-06	0.001294	0.002058	260.5255701	109.2973	37.3144	0.00586	13.06	90	439710	97.2536
14_107.8C_9.5V	107.8	0.005966	4.80769	0.381809051	381.15	2235.78	2.69629E-07	0.602831104	2.30889E-06	0.001123	0.002056	300.4880014	116.4046	32.0054	0.00538	13.627	90	458805	96.1421

Table 5: Calculated heat flux and initial water temperature for surface temperature of 107.0 °C and mass flow rate of 3.29E-07 kg/s

File Name	Temperature, C	Distance_needle center to edge, m	RPS	Surface Velocity, m/s	Surface Temperature, K	hfg (kJ/kg)	Mass Flow Rate, kg/s	q=mhfg (W)	Area, m^2	Width, m	Length, m	q", W/m^2	Theta, adv	Theta, rec	t	t^-1/2	Ti	q calc	Tcalc
15_107.4C_2V	107.4	0.006915	0.46512	0.034184728	380.15	2238.58	3.28804E-07	0.736053361	5.67021E-06	0.00201	0.002821	149.3734047	97.9235	22.4612	0.08257	3.4801	90	114534	84.7071
15_106.8C_2.5V	106.8	0.006947	0.73171	0.053599598	380.15	2238.58	3.28804E-07	0.736053361	5.34139E-06	0.001823	0.00293	158.5689443	109.9231	29.6233	0.05466	4.2771	90	135910	87.1991
15_107.2C_3V	107.2	0.00679	1.0526	0.078143946	380.15	2238.58	3.28804E-07	0.736053361	5.18822E-06	0.001672	0.003103	163.2504455	114.167	24.9755	0.03971	5.0183	90	163261	90.0011
15_106.7C_3.5V	106.7	0.006893	1.35869	0.099988453	380.15	2238.58	3.28804E-07	0.736053361	4.95795E-06	0.001651	0.003003	170.8323119	112.524	20.326	0.03003	5.7703	90	182268	91.0478
15_106.5C_4V	106.5	0.006987	1.64474	0.120067975	380.15	2238.58	3.28804E-07	0.736053361	4.45321E-06	0.001591	0.002799	190.1951095	110.3895	13.1062	0.02331	6.5496	90	204405	91.1471
15_106.6C_4.5V	106.6	0.007054	1.95313	0.141758595	380.15	2238.58	3.28804E-07	0.736053361	4.84373E-06	0.001501	0.003227	174.8609228	118.2256	7.213	0.02276	6.6279	90	208104	92.6517
15_106.9C_5V	106.9	0.006951	2.19298	0.160586187	380.15	2238.58	3.28804E-07	0.736053361	4.90854E-06	0.001508	0.003255	172.5520365	112.3801	8.455	0.02027	7.0239	90	224523	93.9119
15_107.5C_5.5V	107.5	0.006872	2.5	0.184309387	381.15	2235.78	3.28804E-07	0.735132711	0.000004147	0.0013	0.00319	204.0168611	115.7488	7.2121	0.01731	7.6011	90	251601	93.3097
15_107.5C_6V	107.5	0.006886	2.77778	0.204544025	381.15	2235.78	3.28804E-07	0.735132711	2.96915E-06	0.001349	0.002201	284.9496347	116.9442	19.2845	0.01076	9.8401	90	319093	91.8725
15_106.6C_6.5V	106.6	0.006221	3.04878	0.237238098	380.15	2238.58	3.28804E-07	0.736053361	4.3605E-06	0.00153	0.00285	194.2388655	101.6048	32.1523	0.01201	9.1237	90	286467	95.3444
15_106.9C_7V	106.9	0.006274	3.37638	0.261760597	380.15	2238.58	3.28804E-07	0.736053361	3.92134E-06	0.001527	0.002568	215.9923488	113.1873	21.8326	0.00981	10.096	90	322729	95.5894
15_106.6C_7.5V	106.6	0.00627	3.57143	0.276808083	380.15	2238.58	3.28804E-07	0.736053361	4.63858E-06	0.001568	0.002957	182.6732859	111.4854	20.1363	0.01068	9.6753	90	303786	96.6181
15_106.5C_8V	108.5	0.006624	4.03226	0.303556536	380.15	2238.58	3.28804E-07	0.736053361	4.57686E-06	0.001447	0.003163	185.056652	115.7151	31.6689	0.01042	9.7965	90	305739	96.5129
15_106.6C_8.5V	106.6	0.006563	4.16667	0.315272165	380.15	2238.58	3.28804E-07	0.736053361	3.97057E-06	0.001447	0.002744	213.3142092	105.7247	29.5007	0.0087	10.719	90	336554	96.0786
15_106.5C_9V	106.5	0.006563	4.48429	0.337791659	380.15	2238.58	3.28804E-07	0.736053361	2.77721E-06	0.001341	0.002071	304.9745133	114.201	30.8277	0.00613	12.771	90	398579	93.875
15_106.6C_9.5V	106.6	0.006709	4.80769	0.359384799	380.15	2238.58	3.28804E-07	0.736053361	2.96693E-06	0.001275	0.002327	285.4735368	116.2321	30.7729	0.00848	12.427	90	390188	94.4549

Table 6: Calculated heat flux and initial water temperature for surface temperature of 107.0 °C and mass flow rate of 3.55E-07 kg/s

File Name	Temperature, C	Distance_needle center to edge, m	RPS	Surface Velocity, m/s	Surface Temperature, K	hfg (kJ/kg)	Mass Flow Rate, kg/s	q=mhfg (W)	Area, m^2	Width, m	Length, m	q", W/m^2	Theta, adv	Theta, rec	t	t^-1/2	Ti	q calc	Tcalc
16_106.5C_2V	106.5	0.006403	0.48387	0.037098588	380.15	2238.58	3.55316E-07	0.795402217	0.000008064	0.001792	0.0045	113.5009252	95.0253	16.5647	0.1213	2.8713	90	89609.2	85.6007
16_106.3C_2.5V	106.3	0.008519	0.75949	0.057676976	379.15	2241.21	3.55316E-07	0.796336697	7.26748E-06	0.00199	0.003652	126.0692759	114.7534	27.6334	0.06332	3.9741	90	122524	89.5283
16_106.3C_3V	106.3	0.006439	1.034479	0.0790801	379.15	2241.21	3.55316E-07	0.796336697	7.48794E-06	0.001919	0.003902	122.3575757	106.9023	24.9661	0.04934	4.5018	90	138795	91.9304
16_106.8C_3.5V	106.8	0.006498	1.32979	0.101162	380.15	2238.58	3.55316E-07	0.795402217	5.75736E-06	0.001969	0.002924	158.9742689	103.7816	31.2597	0.0289	5.8819	90	186907	92.5107
16_106.9C_4V	106.9	0.006461	1.64474	0.125503767	380.15	2238.58	3.55316E-07	0.795402217	3.93546E-06	0.001284	0.003065	232.5703885	114.972	14.6629	0.02442	6.399	90	204548	87.6848
16_107.1C_4.5V	107.1	0.006563	1.92308	0.145510346	380.15	2238.58	3.55316E-07	0.795402217	4.09778E-06	0.001651	0.002482	223.3577728	124.6027	38.2544	0.01706	7.6568	90	247650	91.6774
16_107.1C_5V	107.1	0.006705	2.19298	0.163975796	380.15	2238.58	3.55316E-07	0.795402217	3.95545E-06	0.001569	0.002521	231.3950859	108.5052	49.161	0.01537	8.065	90	260853	91.9311
16_107C_5.5V	107	0.006465	2.5	0.190702528	380.15	2238.58	3.55316E-07	0.795402217	4.81762E-06	0.001651	0.002918	189.9842331	113.9326	49.4811	0.0153	8.0842	90	259945	94.5753
16_107.2C_6V	107.2	0.006542	2.84091	0.21533304	380.15	2238.58	3.55316E-07	0.795402217	4.35535E-06	0.001506	0.002892	210.1486771	119.1975	45.6636	0.01343	8.6289	90	280725	94.3242
16_107.2C_6.5V	107.2	0.006503	3.04878	0.231836092	380.15	2238.58	3.55316E-07	0.795402217	4.99441E-06	0.001711	0.002919	183.2592127	117.8626	48.9104	0.01259	8.912	90	289933	96.3283
16_107.1C_7V	107.1	0.006342	3.37838	0.260317162	380.15	2238.58	3.55316E-07	0.795402217	4.15548E-06	0.00153	0.002716	220.2564953	123.6454	48.5467	0.01043	9.7901	96	205544	95.2055
16_107C_7.5V	107	0.006094	3.67647	0.289014928	380.15	2238.58	3.55316E-07	0.795402217	4.6618E-06	0.00163	0.00286	196.3343475	109.2624	41.8175	0.0099	10.053	90	323238	96.6742
16_107.6C_8V	107.6	0.006322	3.90625	0.301482448	381.15	2235.78	3.55316E-07	0.794407334	3.56214E-06	0.001369	0.002602	256.6651201	117.951	30.5406	0.00863	10.764	90	358333	94.9935
16_107.3C_8.5V	107.3	0.006604	4.16667	0.314198787	380.15	2238.58	3.55316E-07	0.795402217	3.23619E-06	0.001465	0.002209	282.8242085	106.1246	54.5247	0.00703	11.926	90	390253	94.7624

Table 7: Calculated heat flux and initial water temperature for surface temperature of 107.0 °C and mass flow rate of 3.55E-07 kg/s

File Name	Temperature, C	Distance_needle center to edge, m	RPS	Surface Velocity, m/s	Surface Temperature, K	hfg (kJ/kg)	Mass Flow Rate, kg/s	q=mhfg (W)	Area, m^2	Width, m	Length, m	q", W/m^2	Theta, adv	Theta, rec	t	t^-1/2	Ti	q calc	Tcalc
18_106.6C_2V	106.6	0.006486	0.39735	0.030257831	380.15	2238.58	4.07564E-07	0.912365504	5.90492E-06	0.001769	0.003338	177.7942923	72.0127	17.9873	0.11032	3.0108	90	94532.3	75.3791
18_106.9C_2.5V	106.9	0.006704	0.70589	0.052785981	380.15	2238.58	4.07564E-07	0.912365504	5.96923E-06	0.001691	0.00353	175.8788702	76.9441	4.4882	0.06687	3.867	90	123610	82.8539
18_106.3C_3V	106.3	0.006237	1	0.077713577	379.15	2241.21	4.07564E-07	0.913437398	9.7314E-06	0.0021	0.004634	107.9940525	103.4957	38.0317	0.05963	4.0952	90	126257	92.3577
18_106.4C_3.5V	106.4	0.006374	1.28866	0.099037105	379.15	2241.21	4.07564E-07	0.913437398	5.63531E-06	0.001755	0.003211	186.4909393	108.4349	19.7029	0.03242	5.5537	90	172274	88.6466
18_106.3C_4V	106.3	0.006356	1.58228	0.12178157	379.15	2241.21	4.07564E-07	0.913437398	7.92202E-06	0.001981	0.003999	132.6597831	104.0936	23.2685	0.03284	5.5184	90	170137	93.5905
18_106.2C_4.5V	106.2	0.006377	1.89394	0.145518856	379.15	2241.21	4.07564E-07	0.913437398	6.21353E-06	0.001899	0.003272	169.13633	101.9105	24.5974	0.02249	6.6689	90	204345	92.7913
18_106.1C_5V	106.1	0.006392	2.15517	0.165387064	379.15	2241.21	4.07564E-07	0.913437398	5.78074E-06	0.001841	0.00314	181.7990988	114.4879	27.8489	0.01899	7.2575	90	221008	92.8563
18_106.5C_5.5V	106.5	0.006298	2.45098	0.189535026	380.15	2238.58	4.07564E-07	0.912365504	4.82784E-06	0.001712	0.00282	217.4598636	107.8333	32.4755	0.01488	8.1982	90	255859	92.4763
18_107C_6V	107	0.006383	2.77778	0.213323038	380.15	2238.58	4.07564E-07	0.912365504	5.60306E-06	0.001772	0.003162	187.3727354	110.1943	34.9547	0.01482	8.2137	90	264109	94.9393
18_107.6C_6.5V	107.6	0.006437	3.125	0.238927939	381.15	2235.78	4.07564E-07	0.911224323	5.15624E-06	0.001588	0.003247	203.3887215	117.6236	30.6557	0.01359	8.5781	90	285563	95.0646
18_107.6C_7V	107.6	0.006315	3.37838	0.260890291	381.15	2235.78	4.07564E-07	0.911224323	5.80822E-06	0.001651	0.003518	180.5580038	108.2813	31.5222	0.01348	8.6115	90	286675	96.5149
18_106.6C_7.5V	106.6	0.006368	3.57143	0.274608968	380.15	2238.58	4.07564E-07	0.912365504	3.77441E-06	0.001479	0.002552	278.1526078	115.622	32.5175	0.00929	10.373	90	325703	92.4235

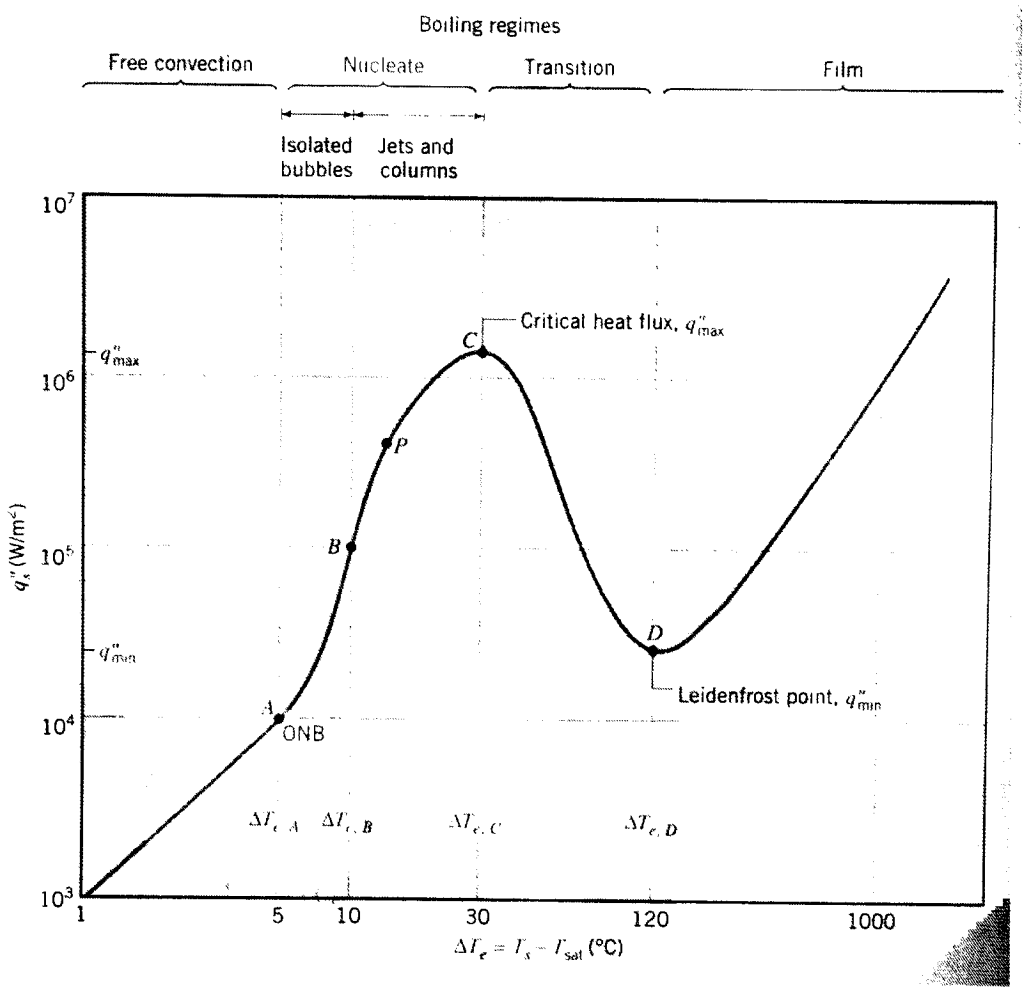

Figure 36: Boiling curve for water at 1 atm.

Appendix C

Images of menisci for surface temperature of 105.5°C and water mass flow rate of 2.7E-7 kg/s with varying surface velocities.

Front View

Side View

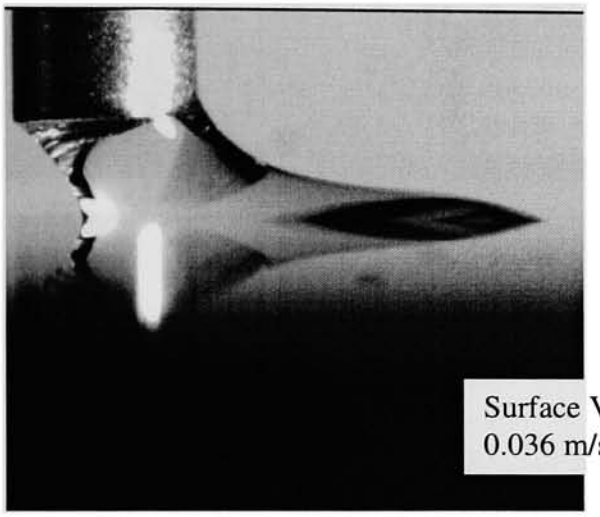

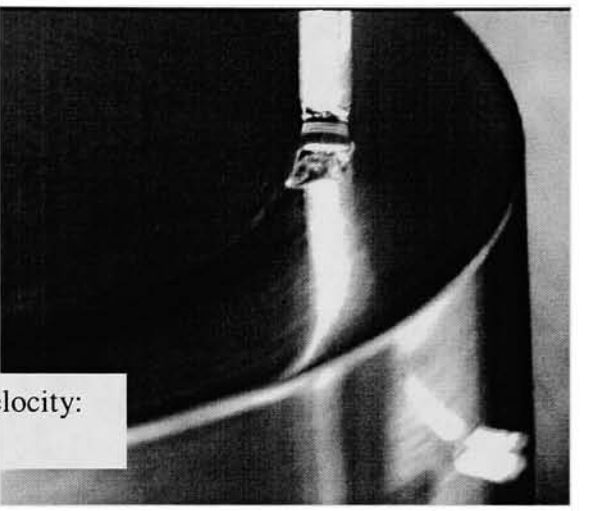

Surface Velocity:
0.036 m/s

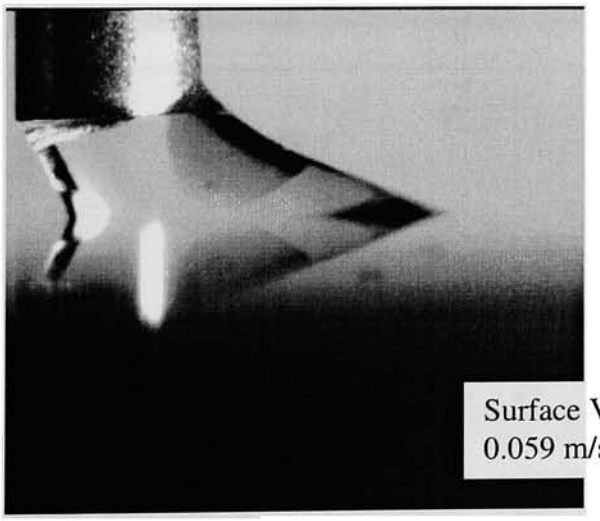

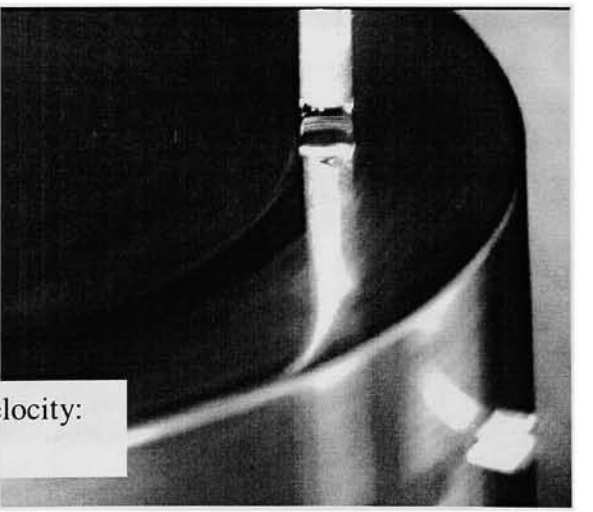

Surface Velocity:
0.059 m/s

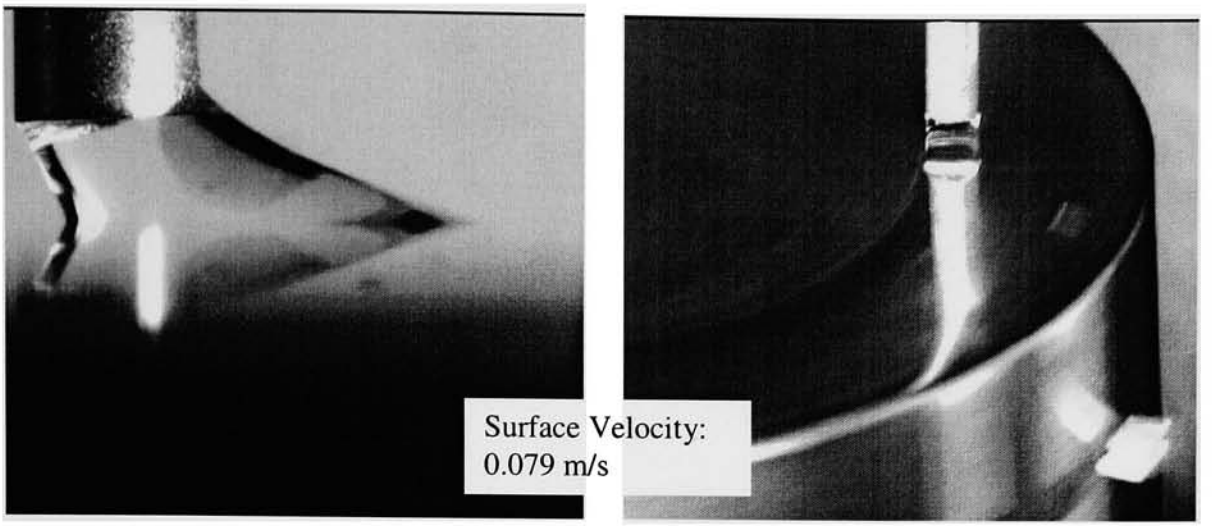
Surface Velocity:
0.079 m/s

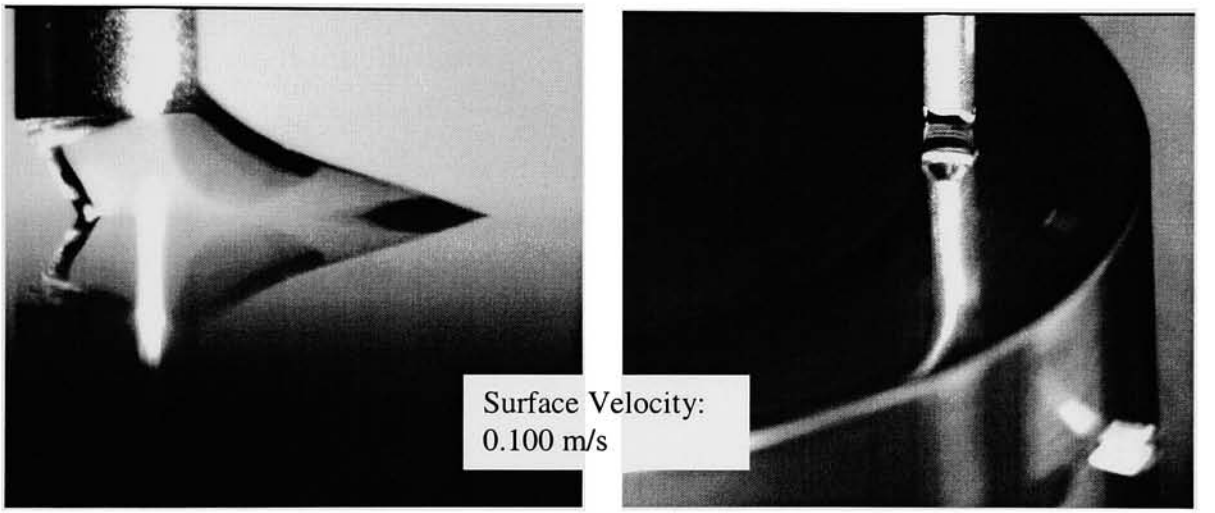
Surface Velocity:
0.100 m/s

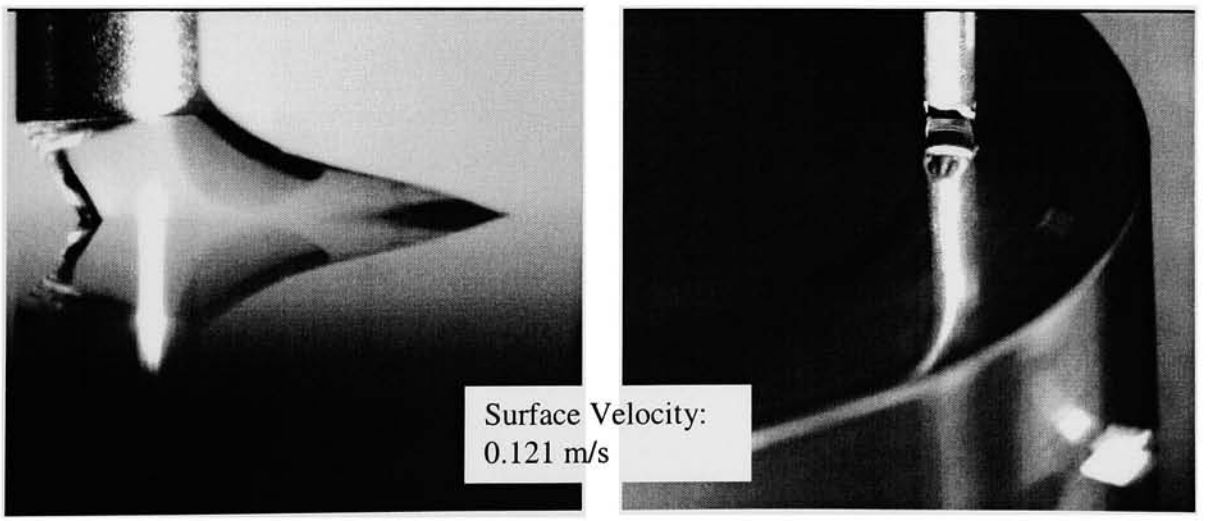
Surface Velocity:
0.121 m/s

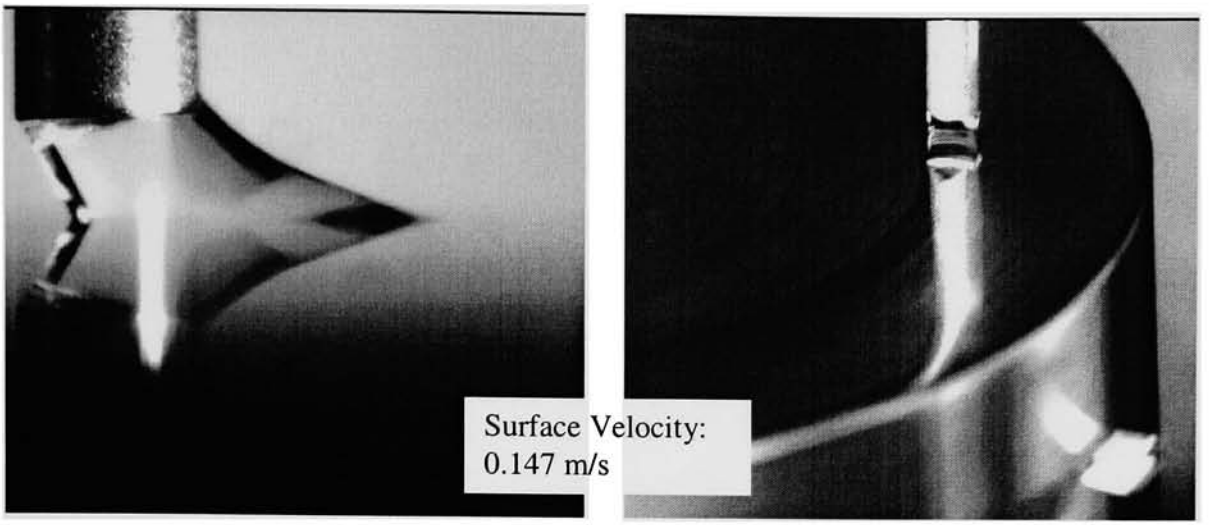
Surface Velocity:
0.147 m/s

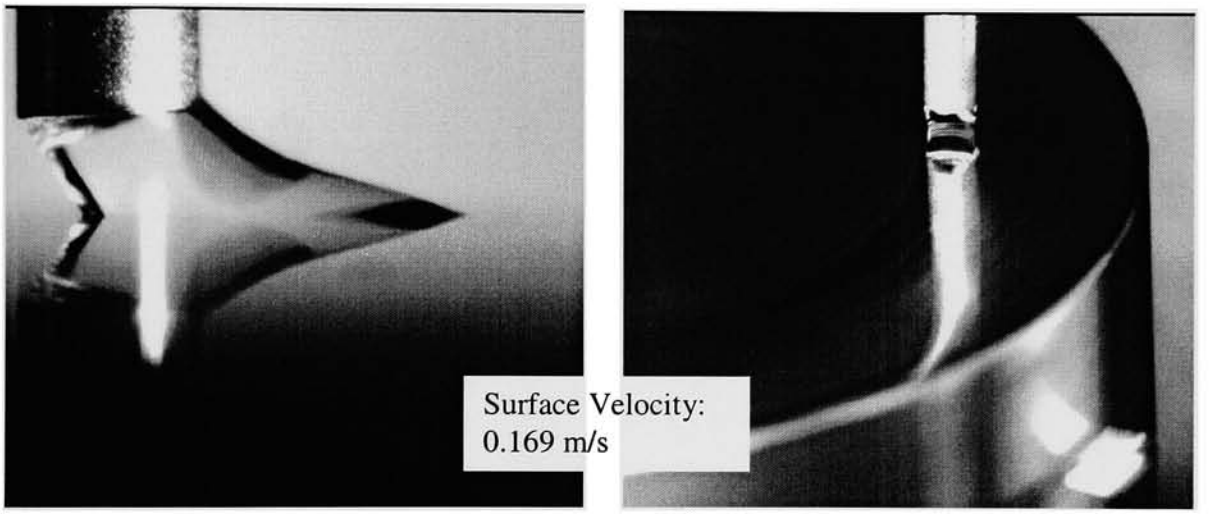
Surface Velocity:
0.169 m/s

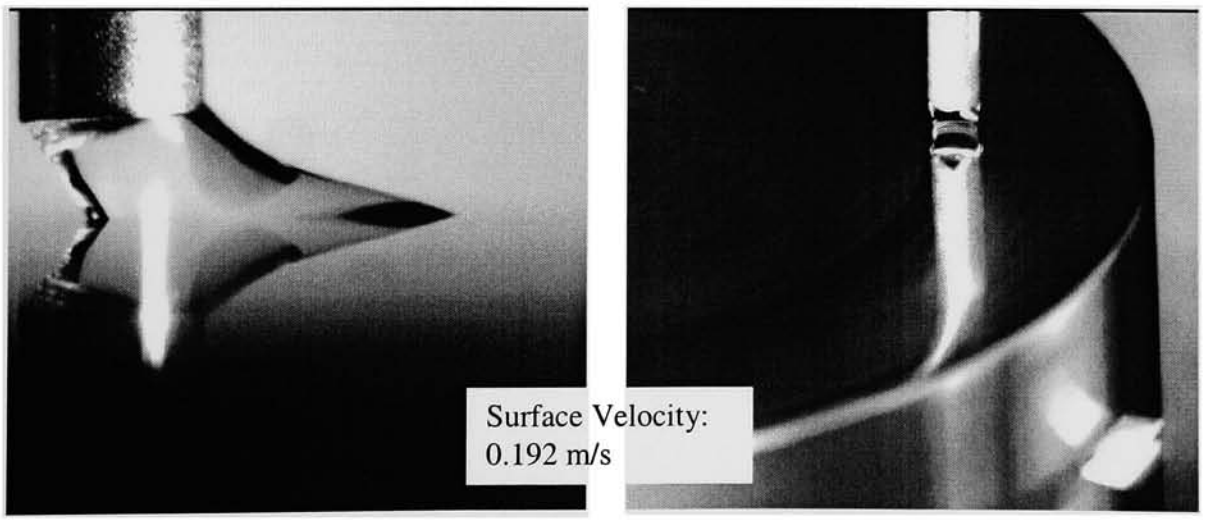
Surface Velocity:
0.192 m/s

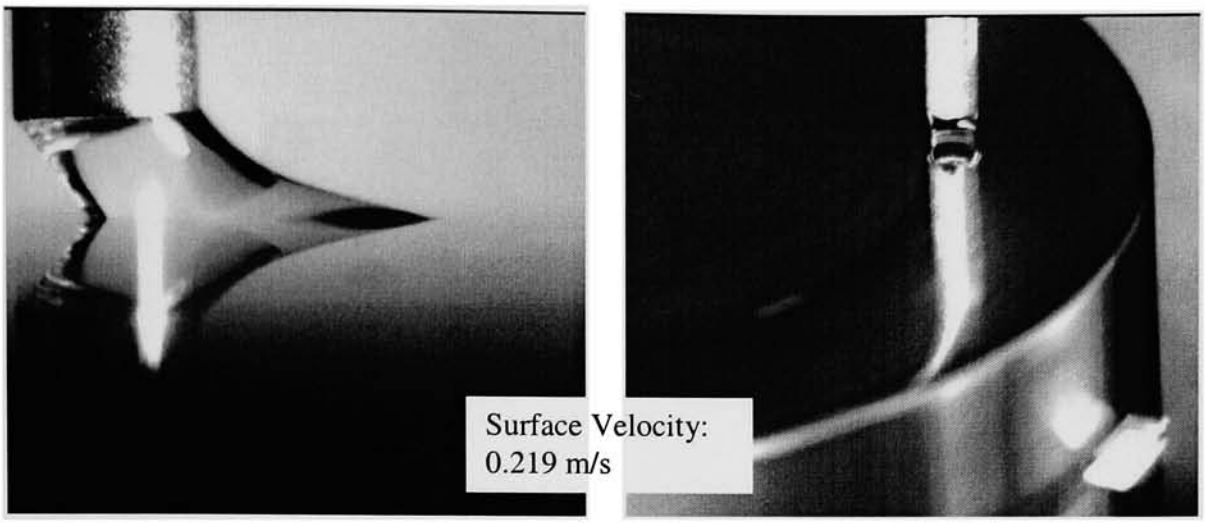
Surface Velocity:
0.219 m/s

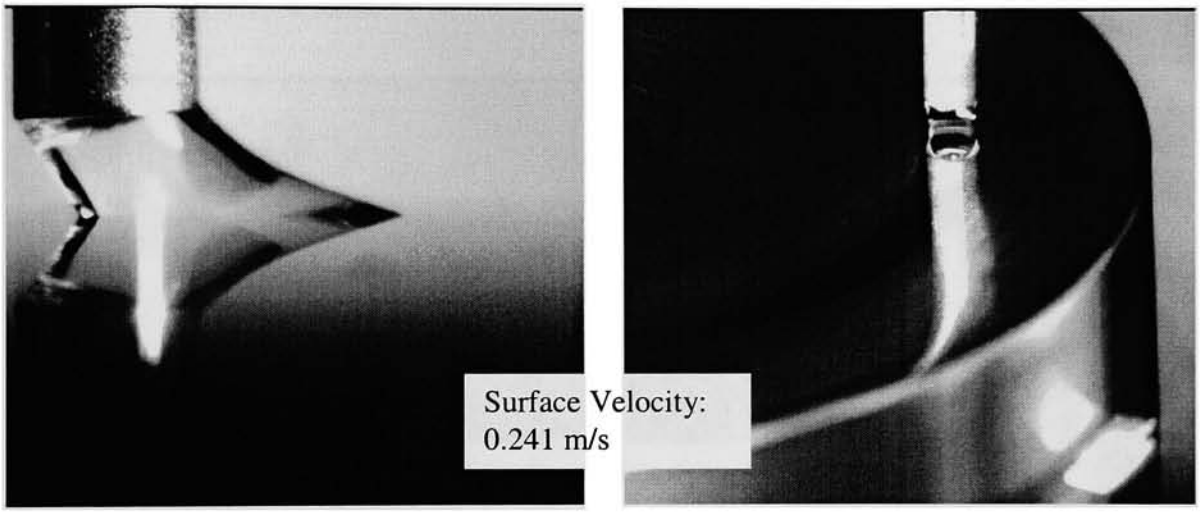
Surface Velocity:
0.241 m/s

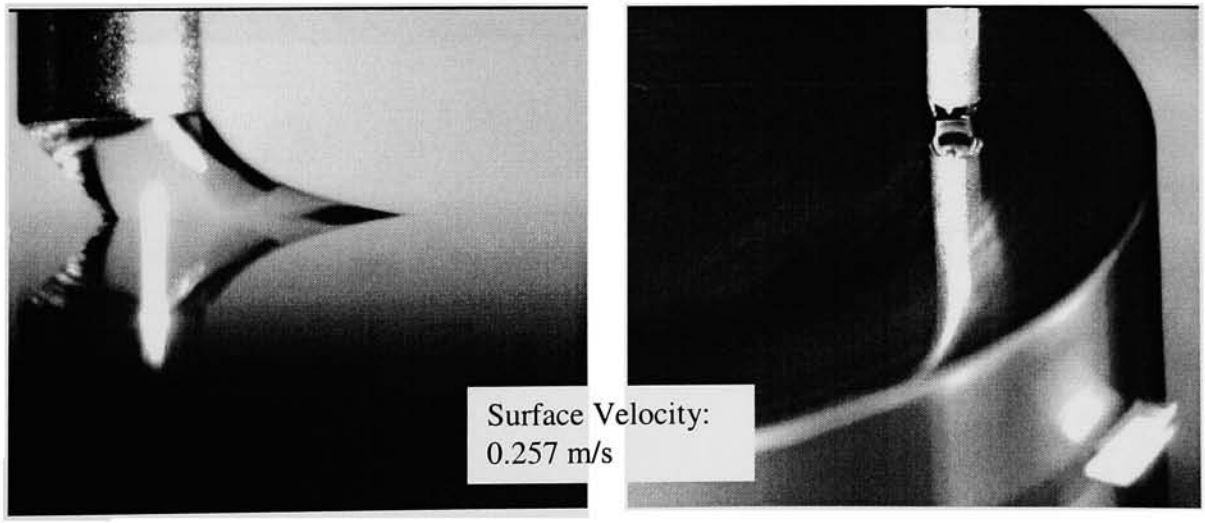
Surface Velocity:
0.257 m/s

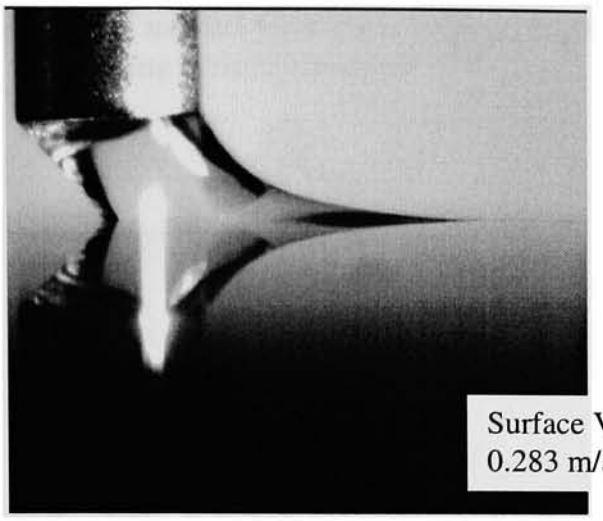

Surface Velocity:
0.283 m/s

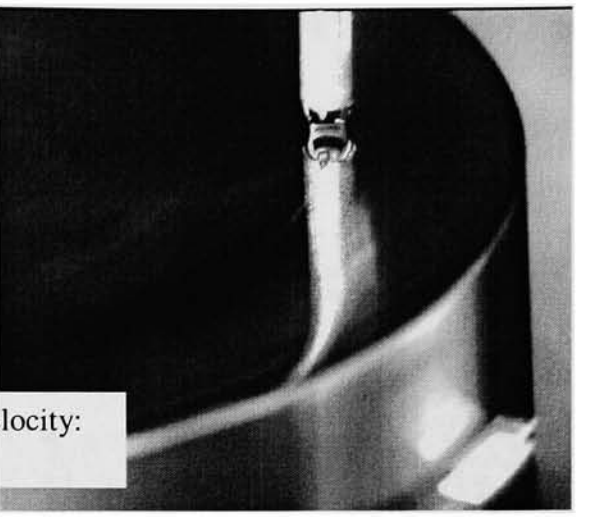

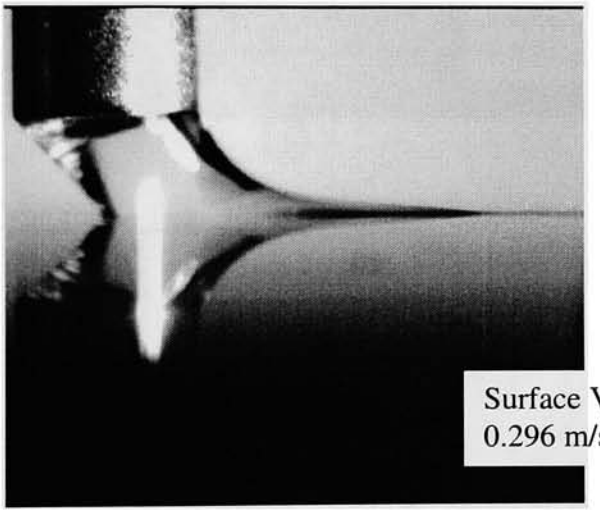

Surface Velocity:
0.296 m/s

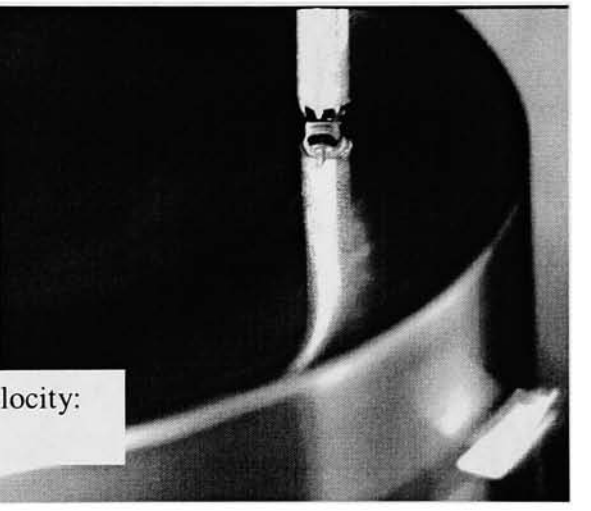

Images of menisci for surface temperature of 108°C and water mass flow rate of 2.7E-7 kg/s with varying surface velocities.

Front View

Side View

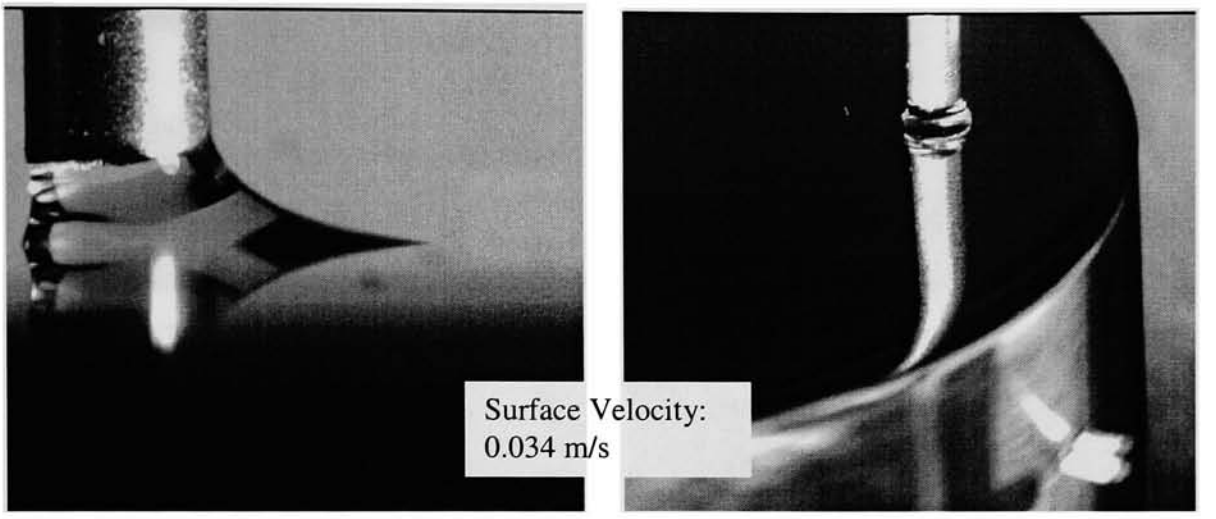

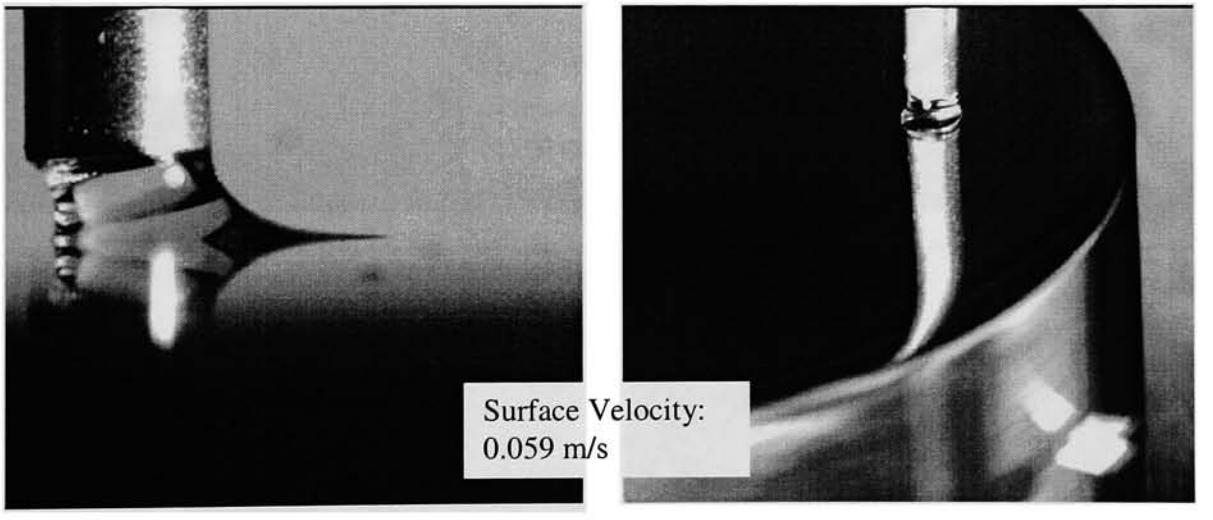

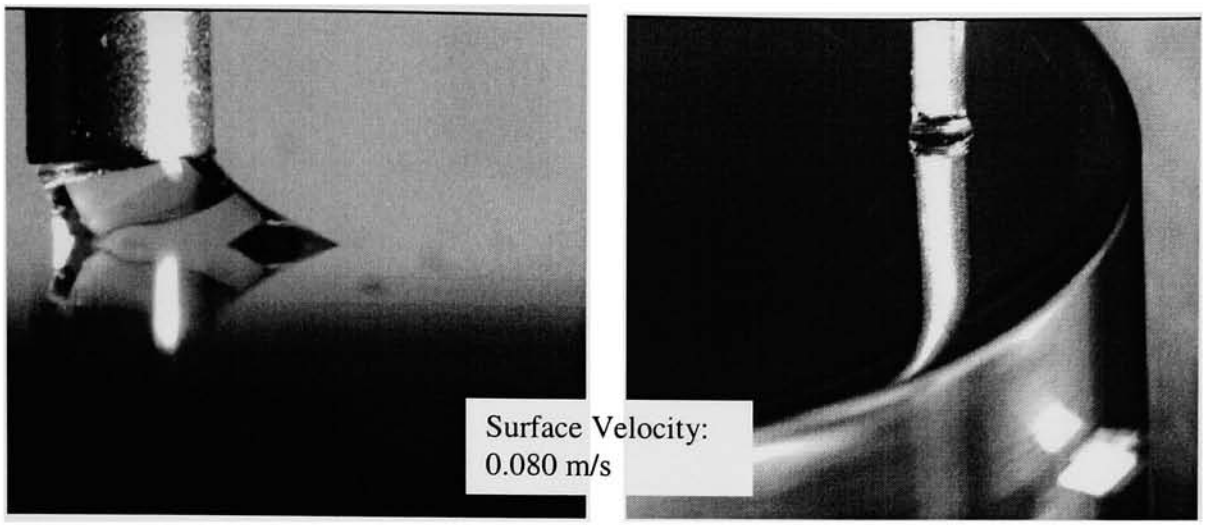
Surface Velocity:
0.080 m/s

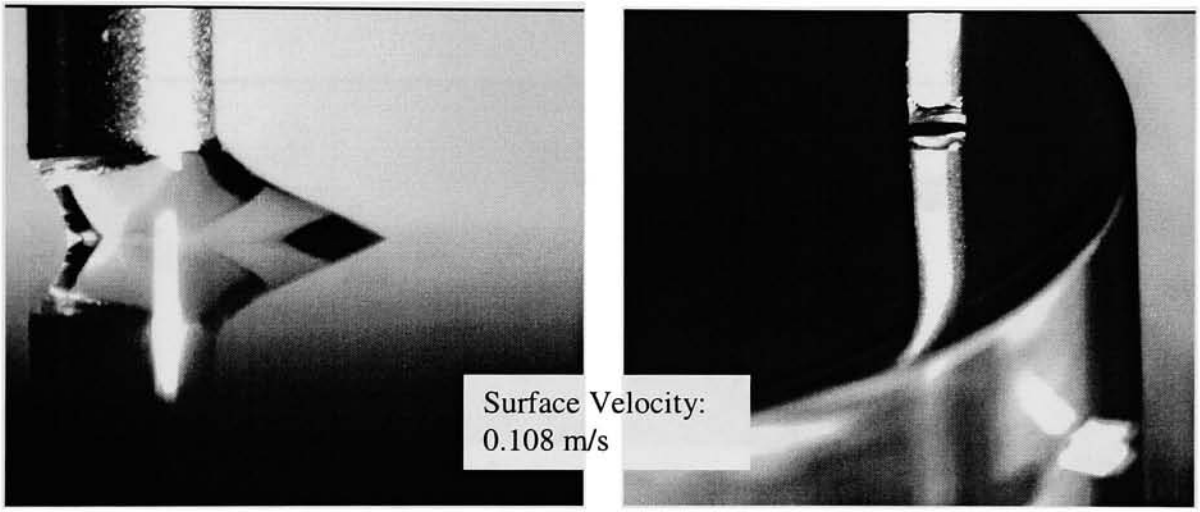
Surface Velocity:
0.108 m/s

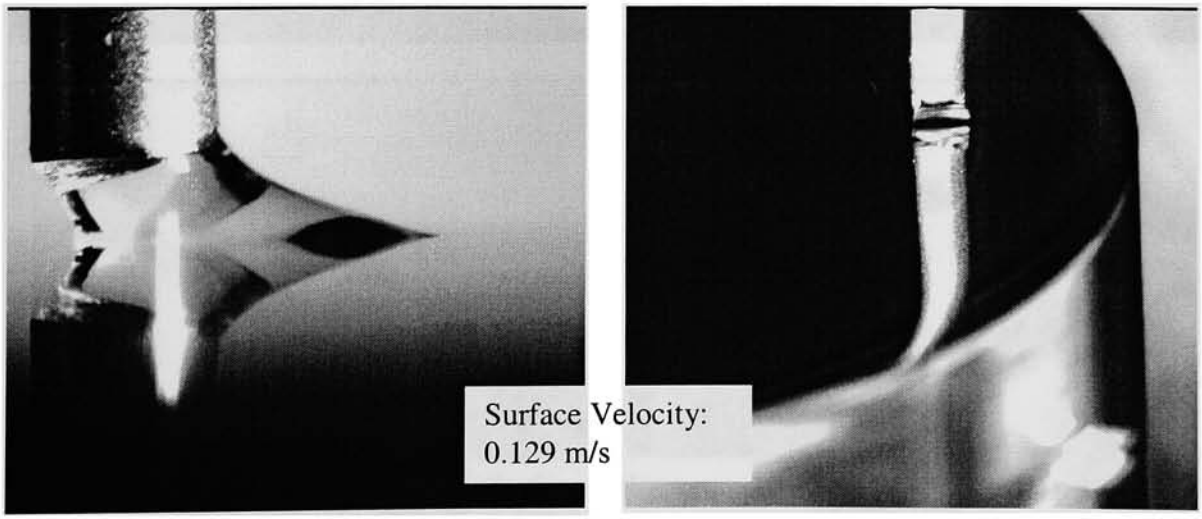
Surface Velocity:
0.129 m/s

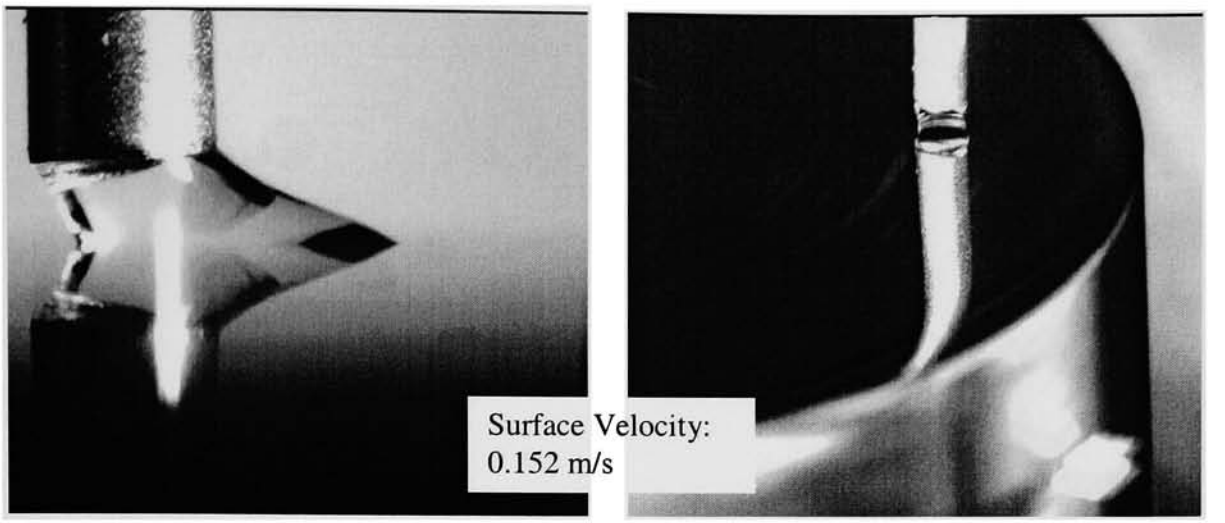
Surface Velocity:
0.152 m/s

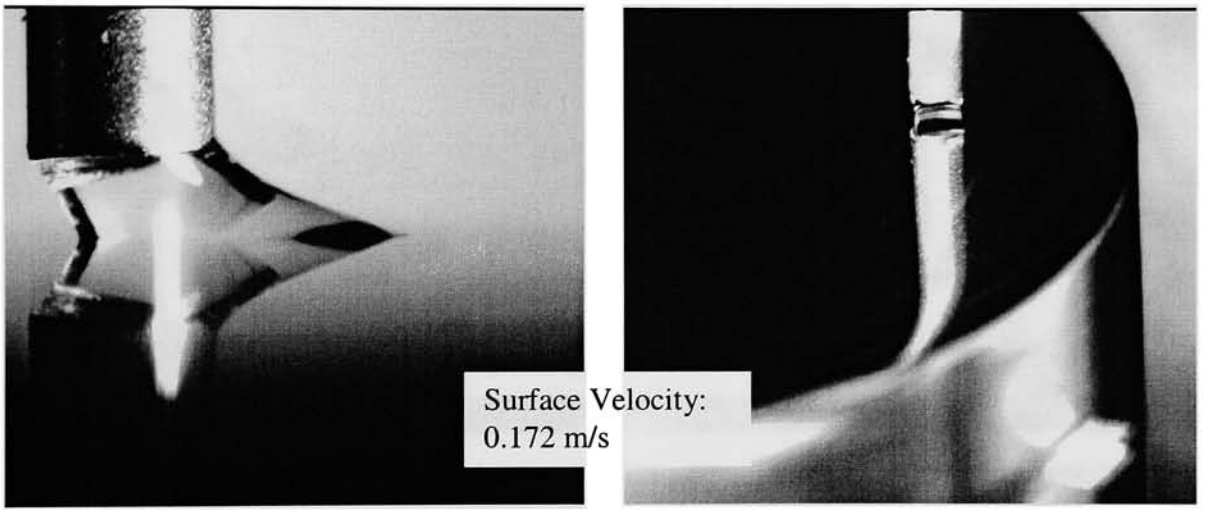
Surface Velocity:
0.172 m/s

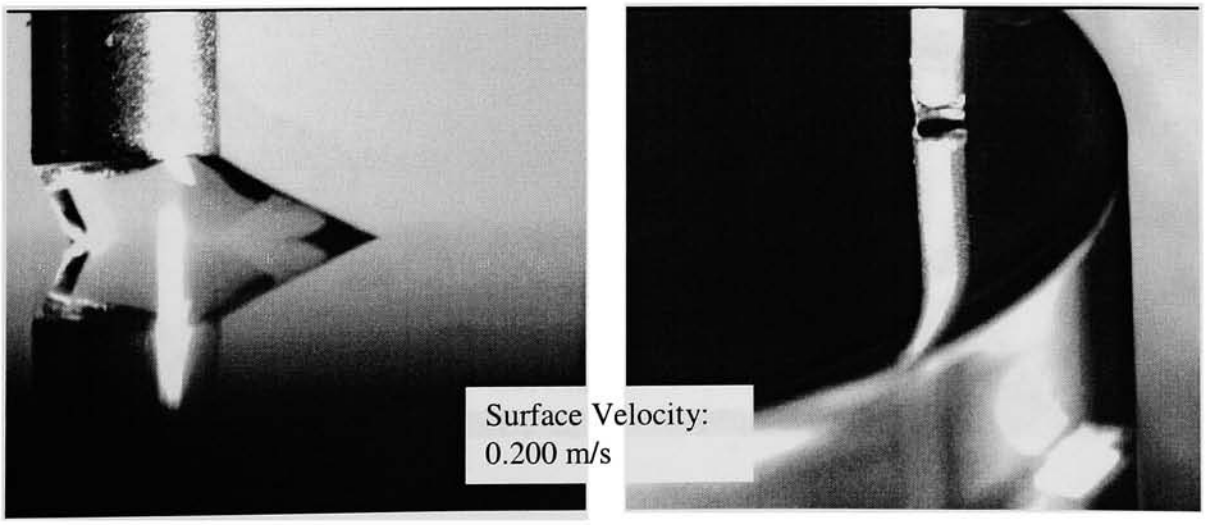
Surface Velocity:
0.200 m/s

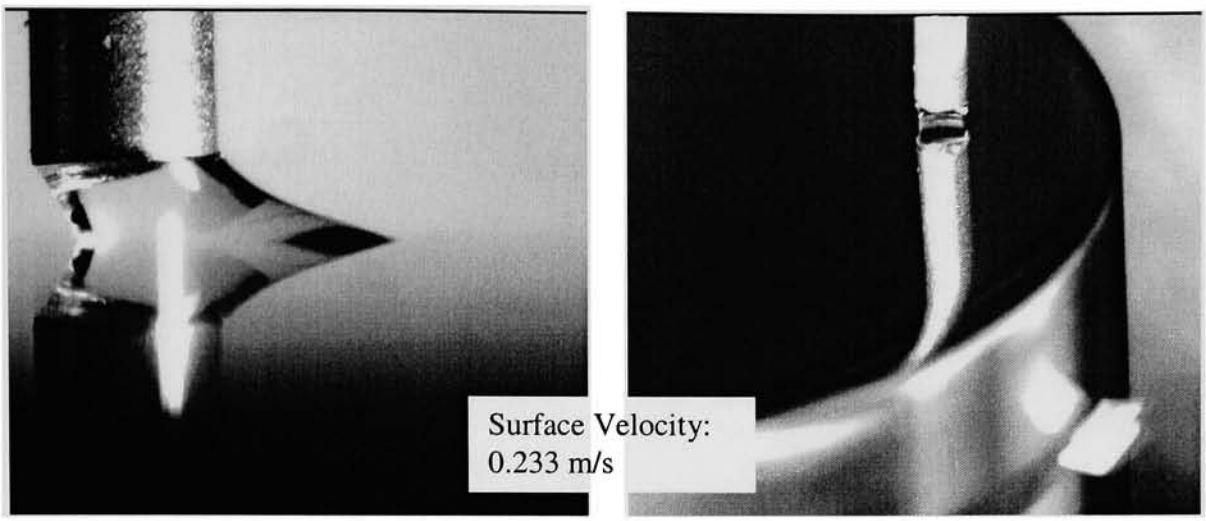
Surface Velocity:
0.233 m/s

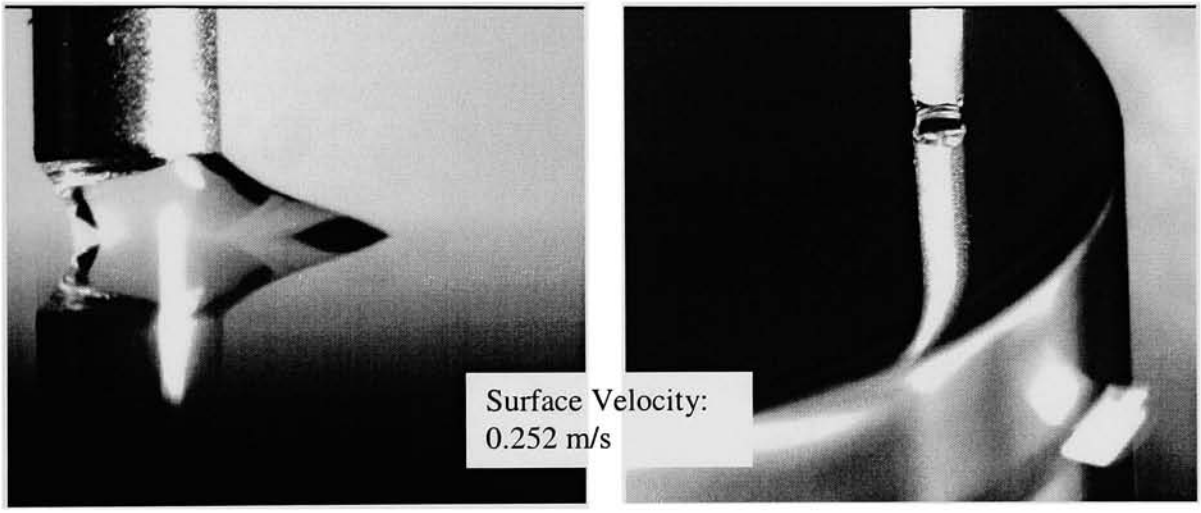
Surface Velocity:
0.252 m/s

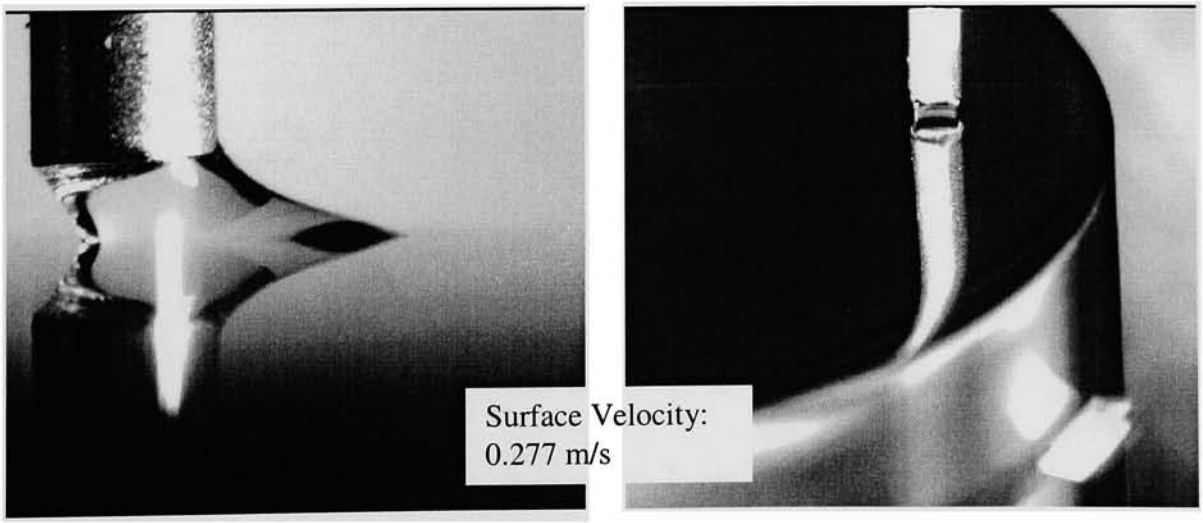
Surface Velocity:
0.277 m/s

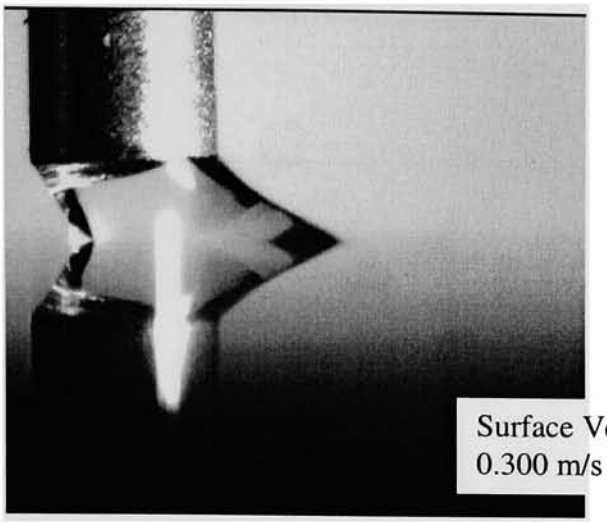
Surface Velocity:
0.300 m/s

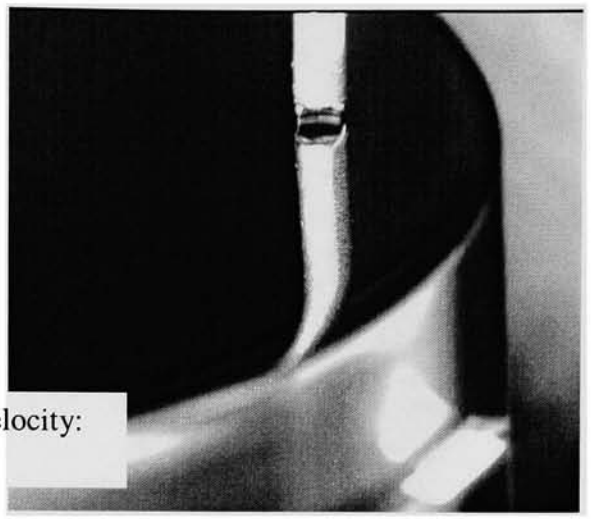

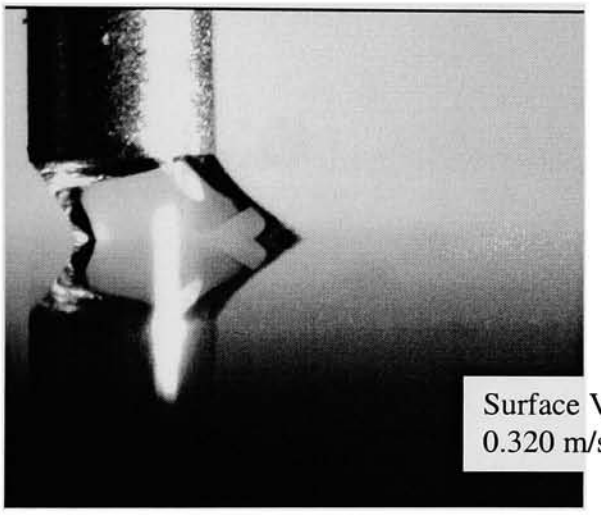
Surface Velocity:
0.320 m/s

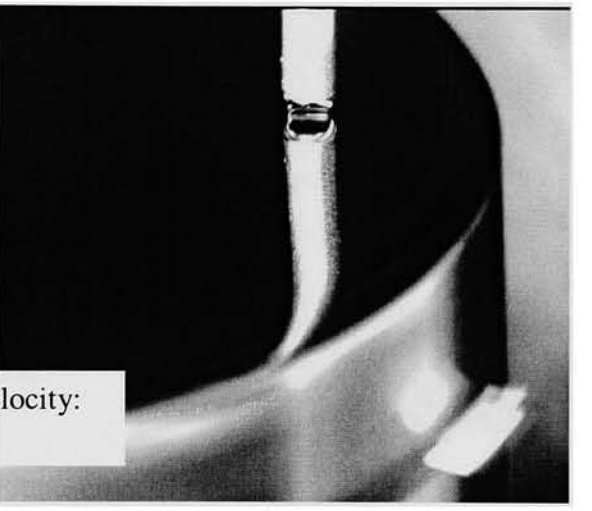

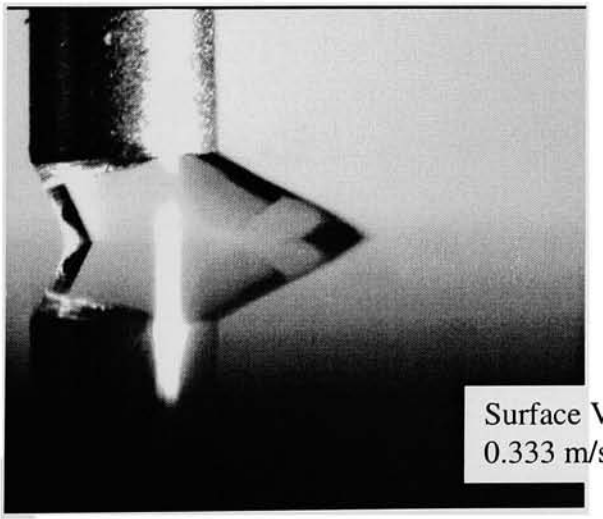
Surface Velocity:
0.333 m/s

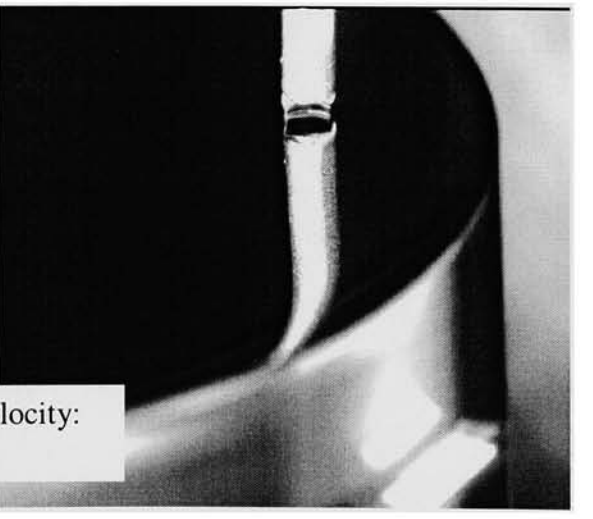

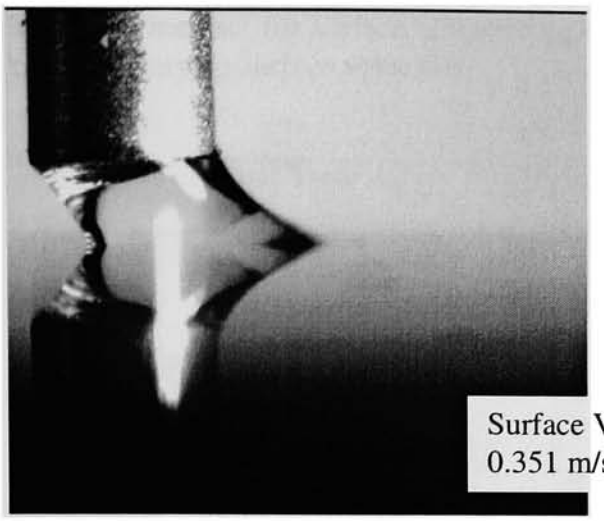

Surface Velocity:
0.351 m/s

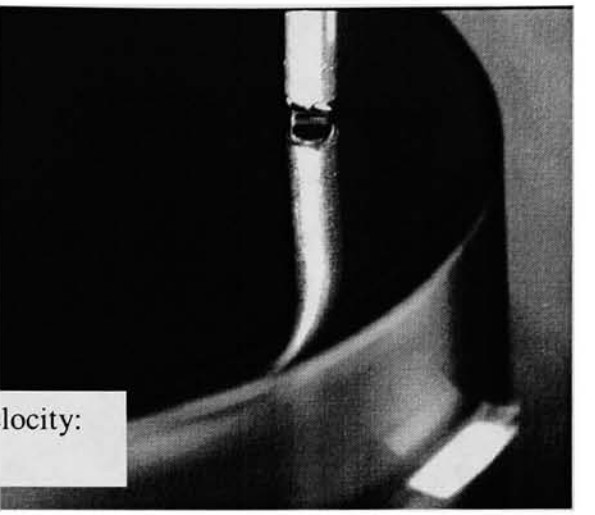

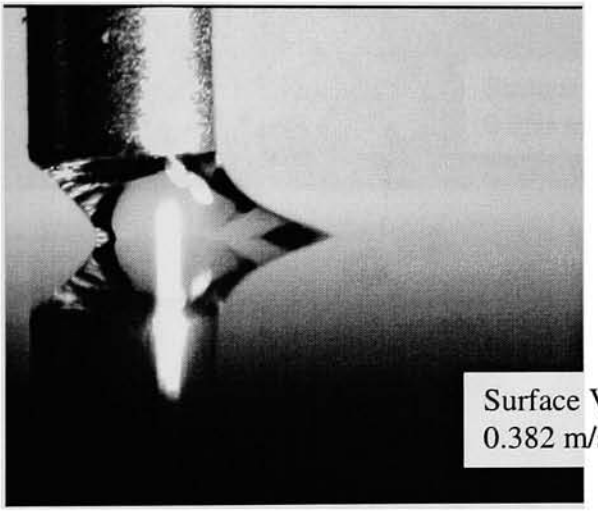

Surface Velocity:
0.382 m/s

Images of menisci for surface temperature of 102.5°C and water mass flow rate of 2.7E-7 kg/s with varying surface velocities.

Front View

Side View

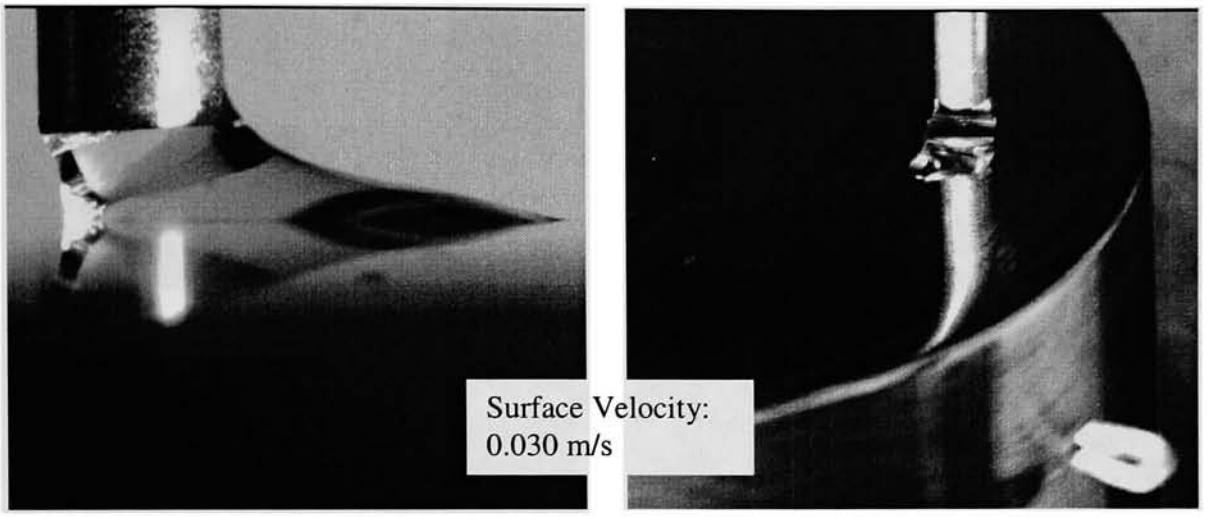

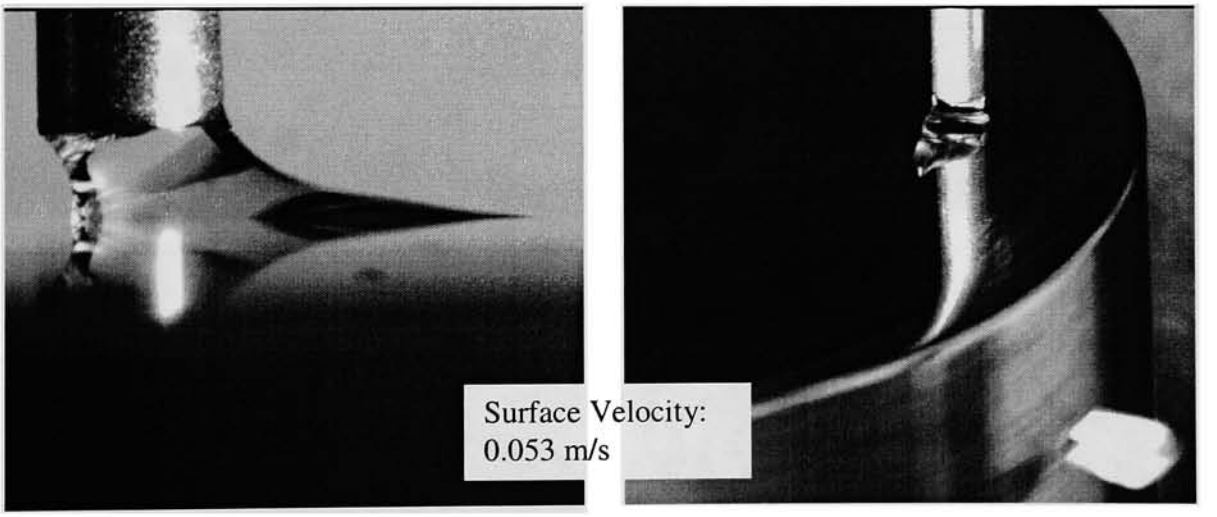

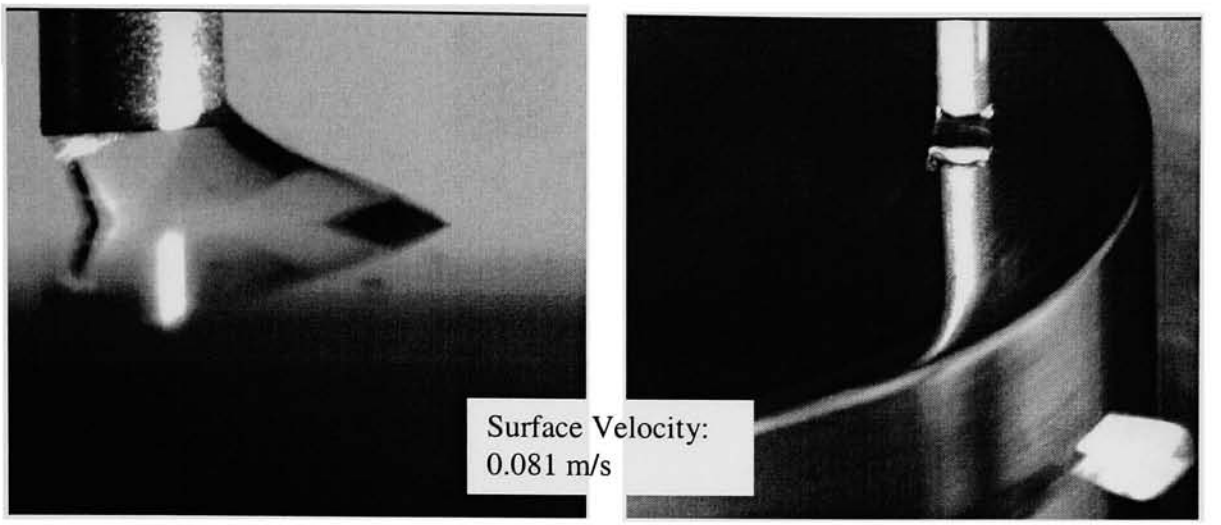
Surface Velocity:
0.081 m/s

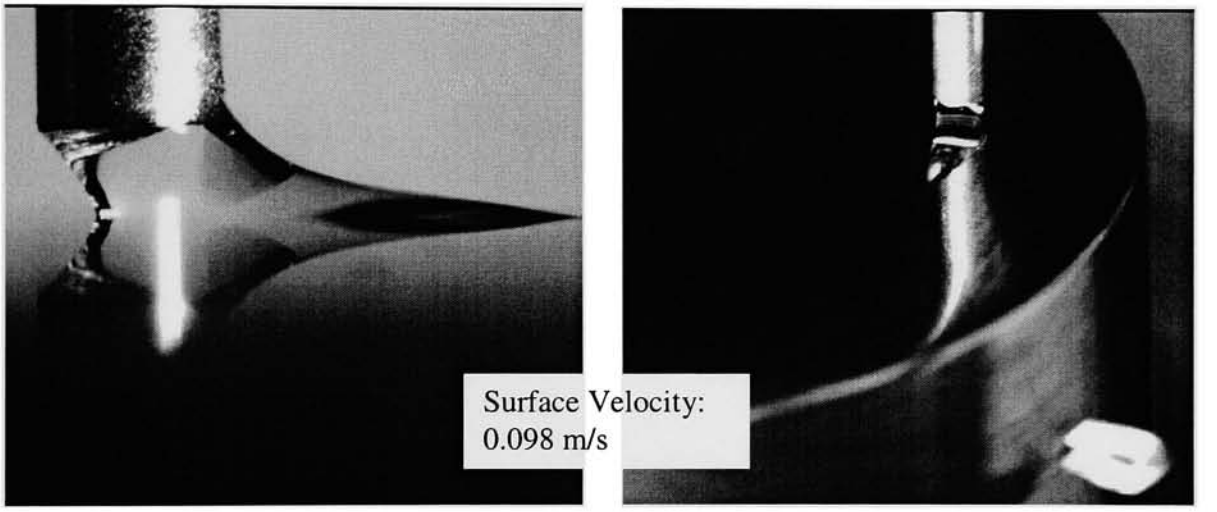
Surface Velocity:
0.098 m/s

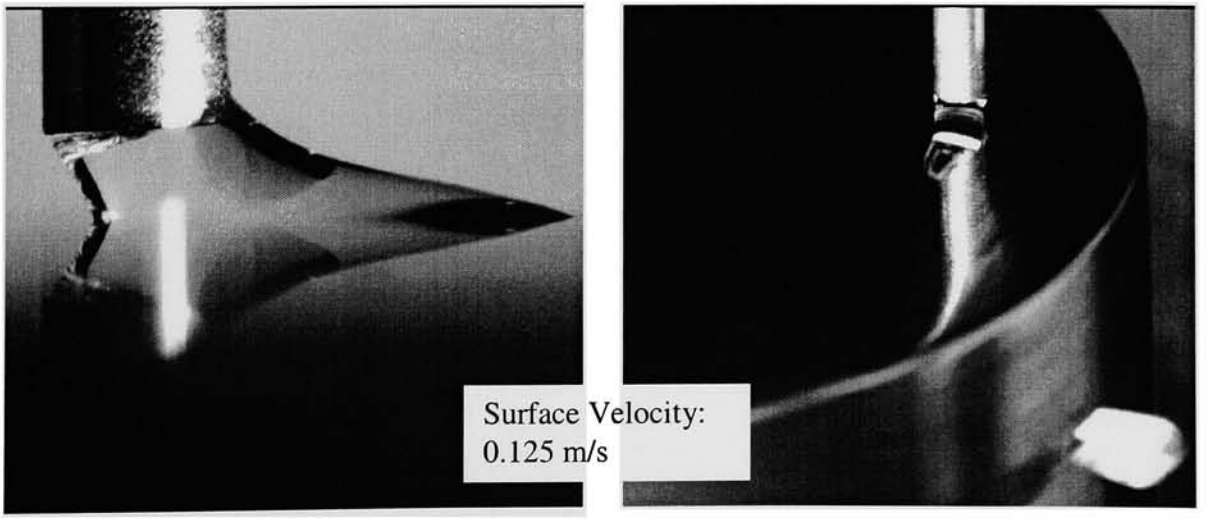
Surface Velocity:
0.125 m/s

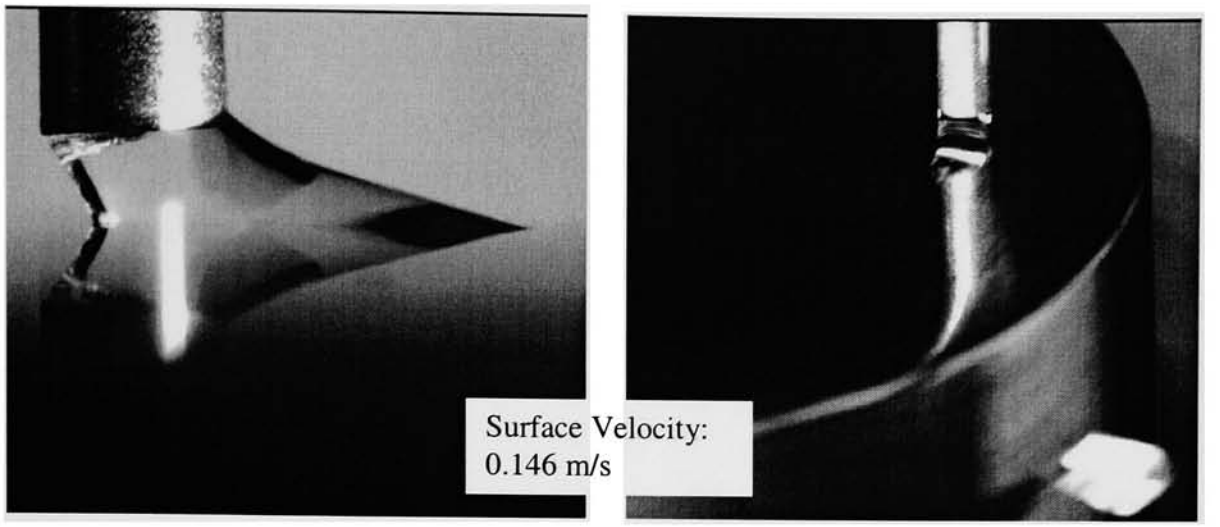
Surface Velocity:
0.146 m/s

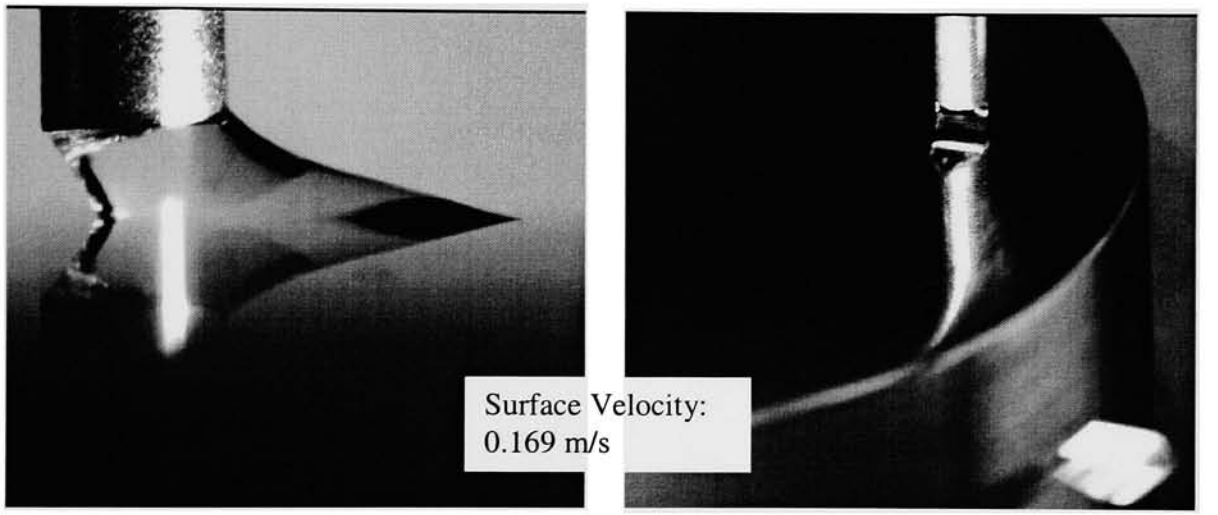
Surface Velocity:
0.169 m/s

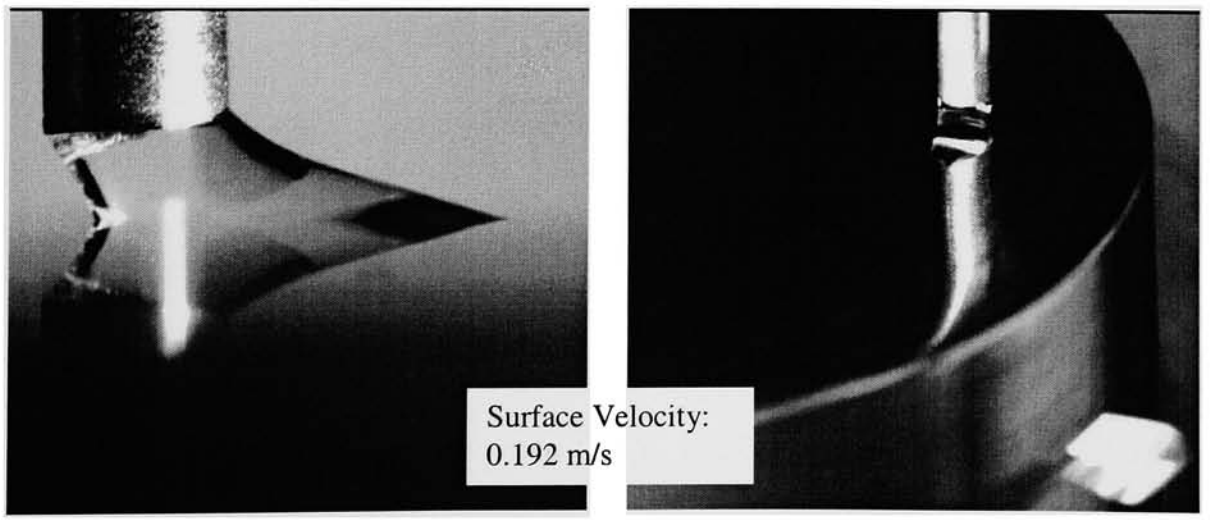
Surface Velocity:
0.192 m/s

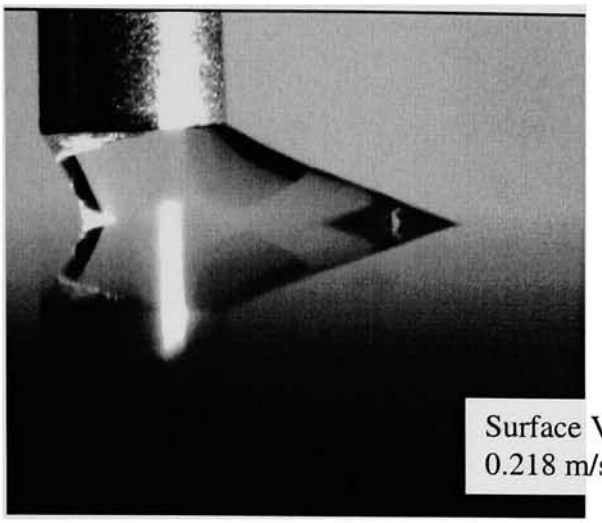
Surface Velocity:
0.218 m/s

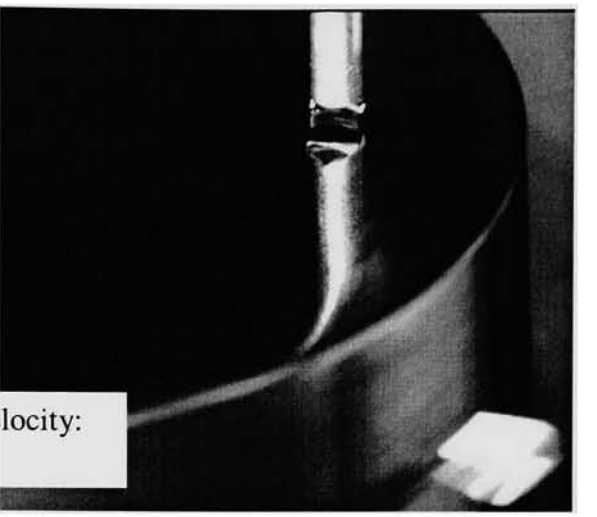

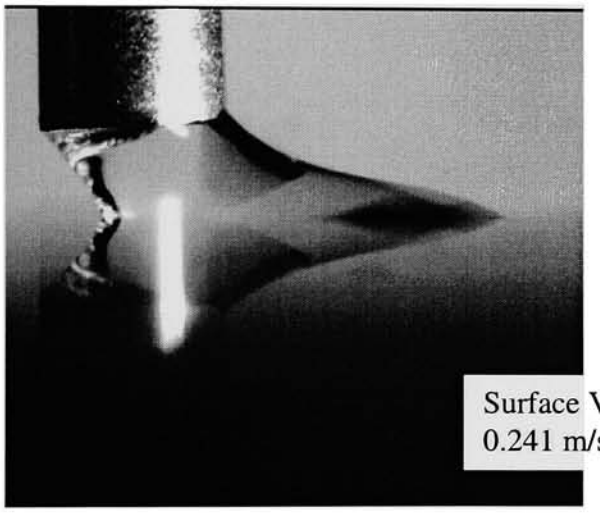
Surface Velocity:
0.241 m/s

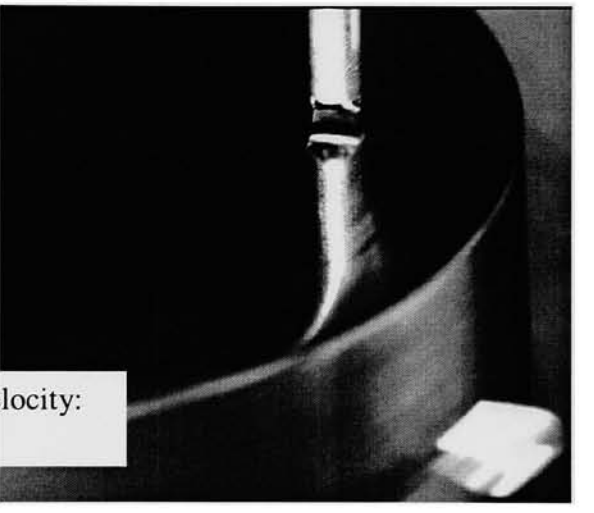

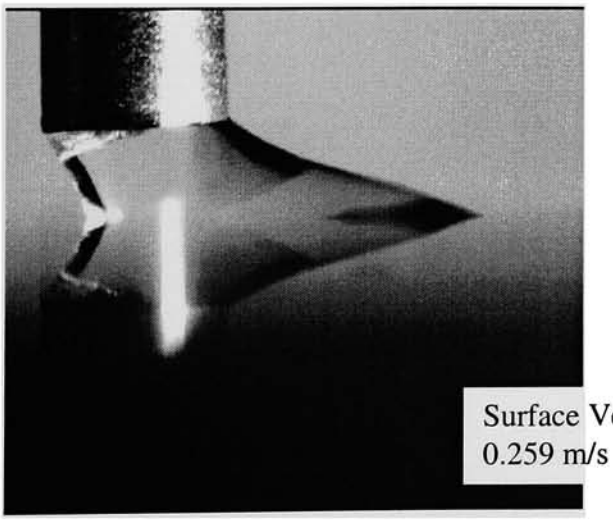
Surface Velocity:
0.259 m/s

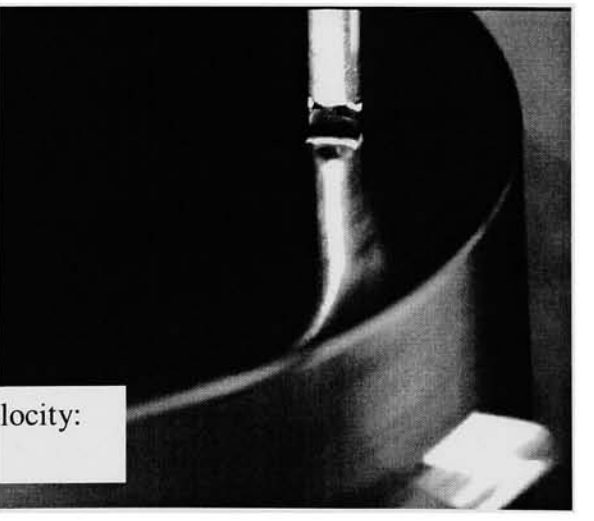

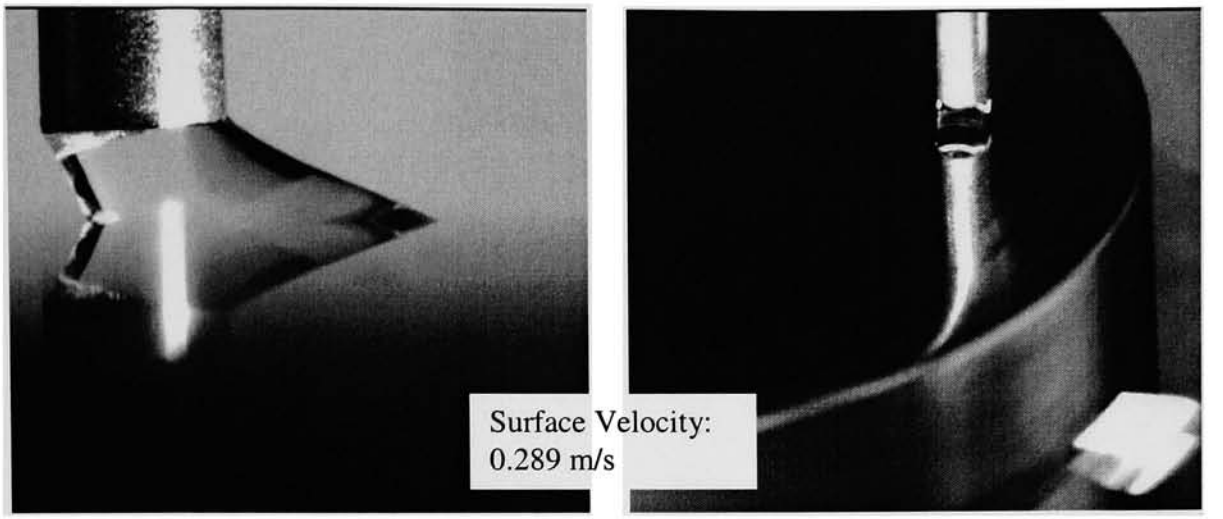
Surface Velocity:
0.289 m/s

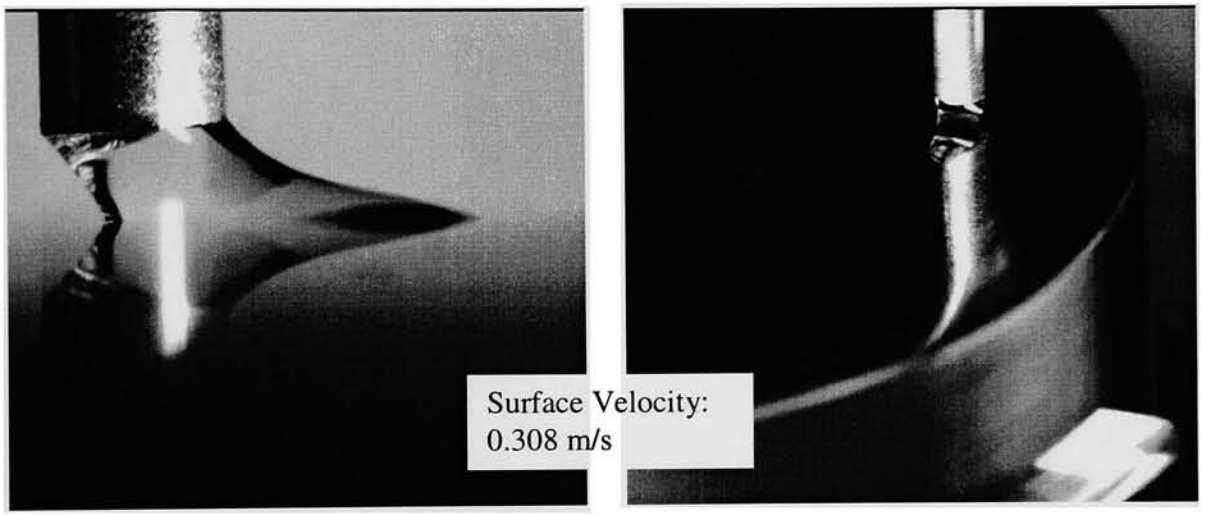
Surface Velocity:
0.308 m/s

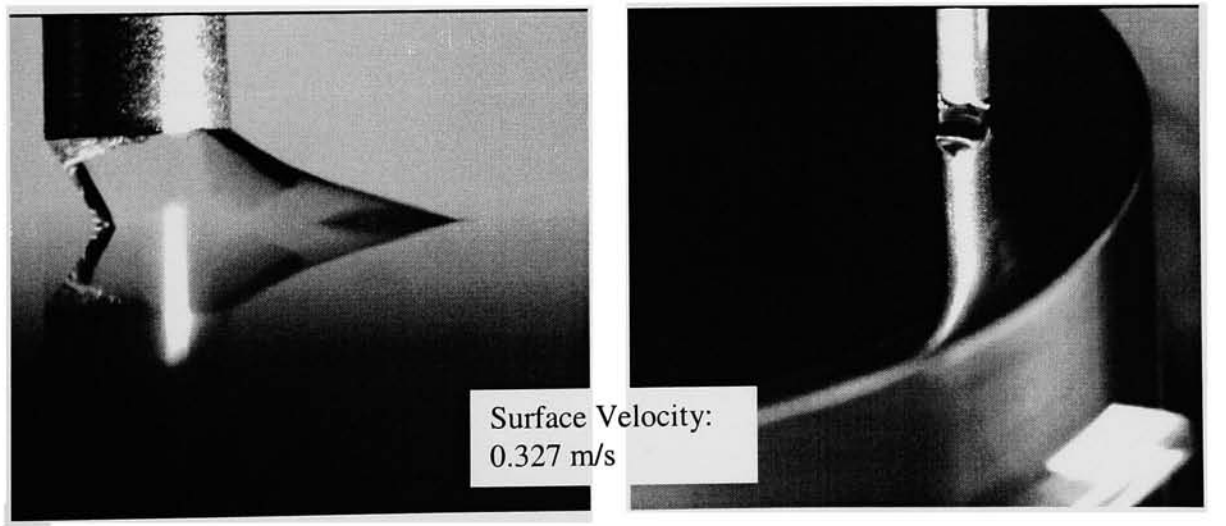
Surface Velocity:
0.327 m/s

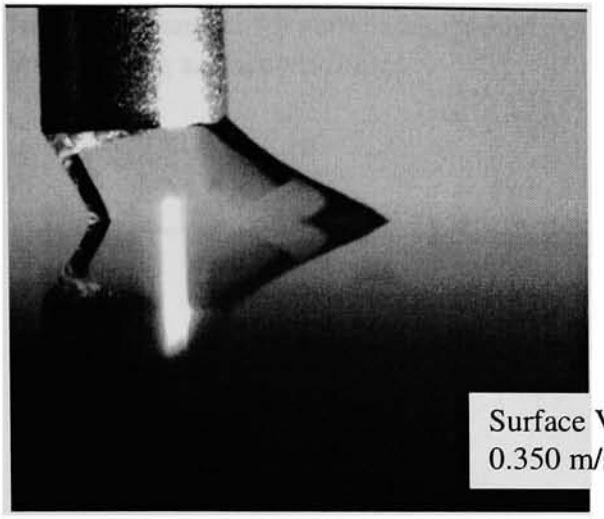

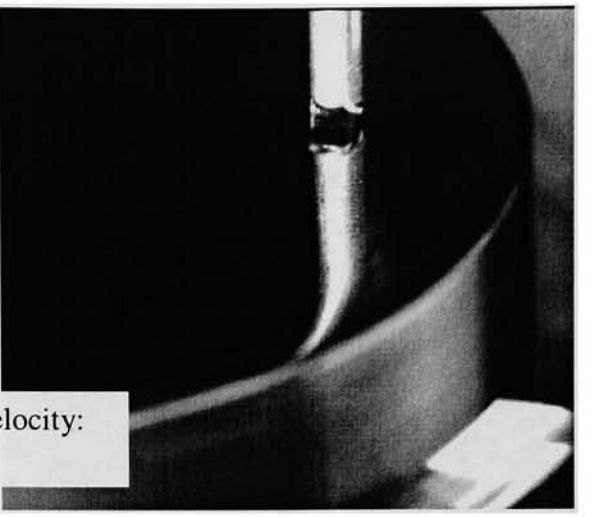

Surface Velocity:
0.350 m/s

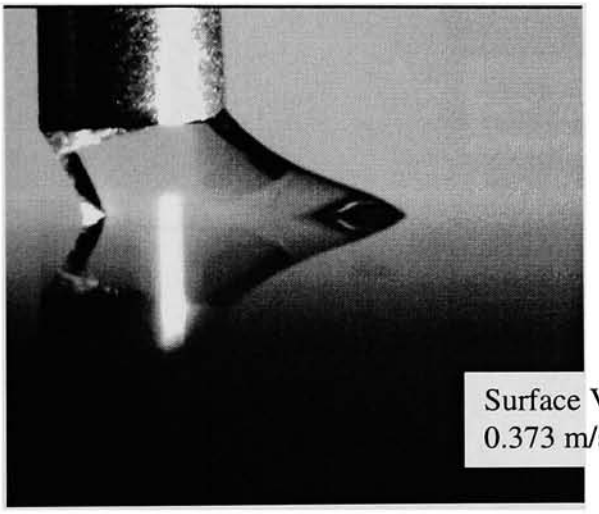

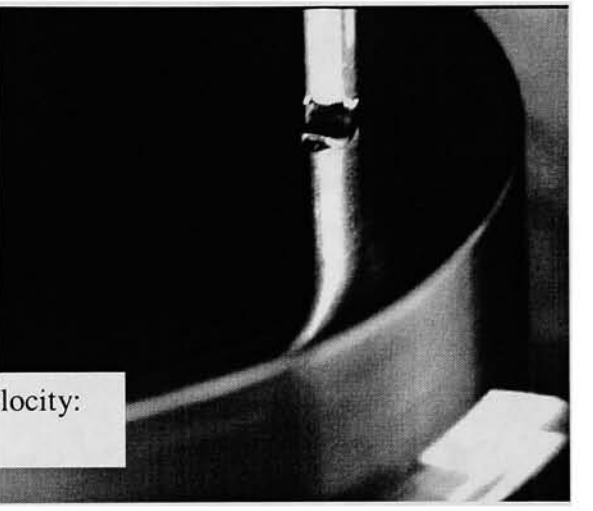

Surface Velocity:
0.373 m/s

Images of menisci for surface temperature of 107°C and water mass flow rate of 3.55E-7 kg/s with varying surface velocities.

Front View

Side View

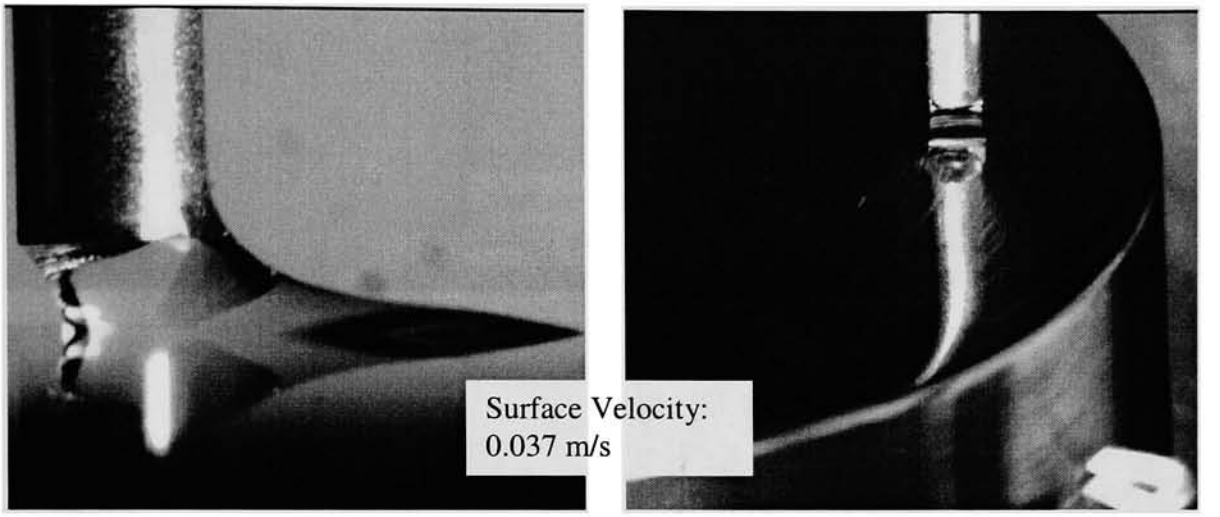

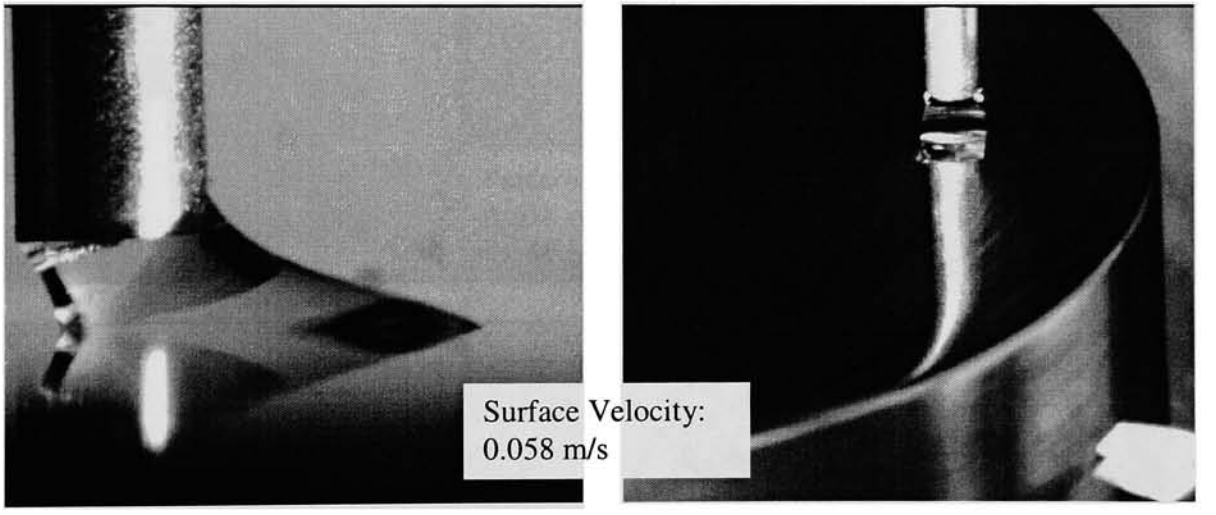

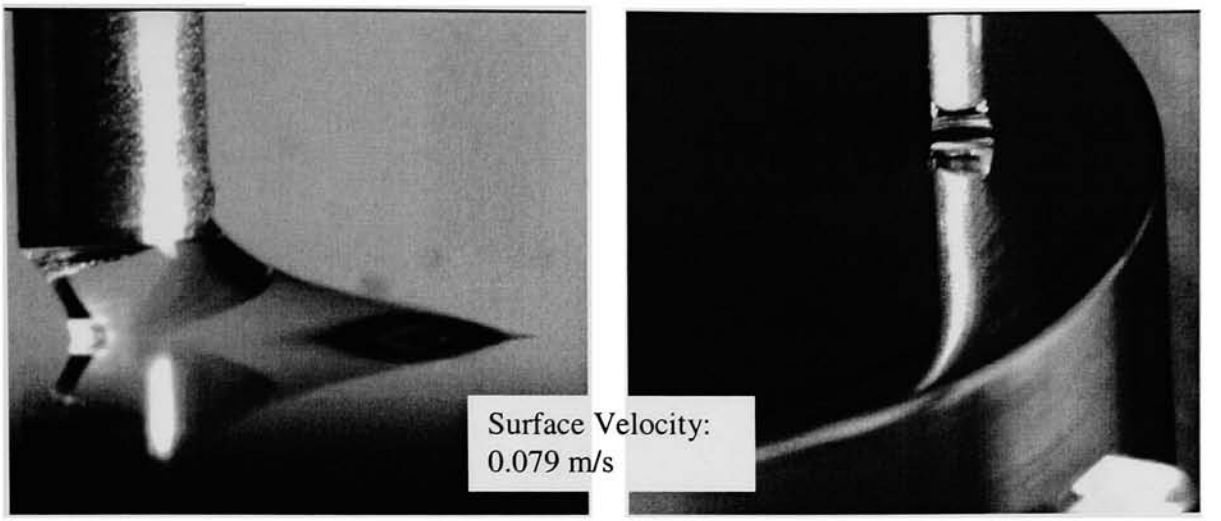
Surface Velocity:
0.079 m/s

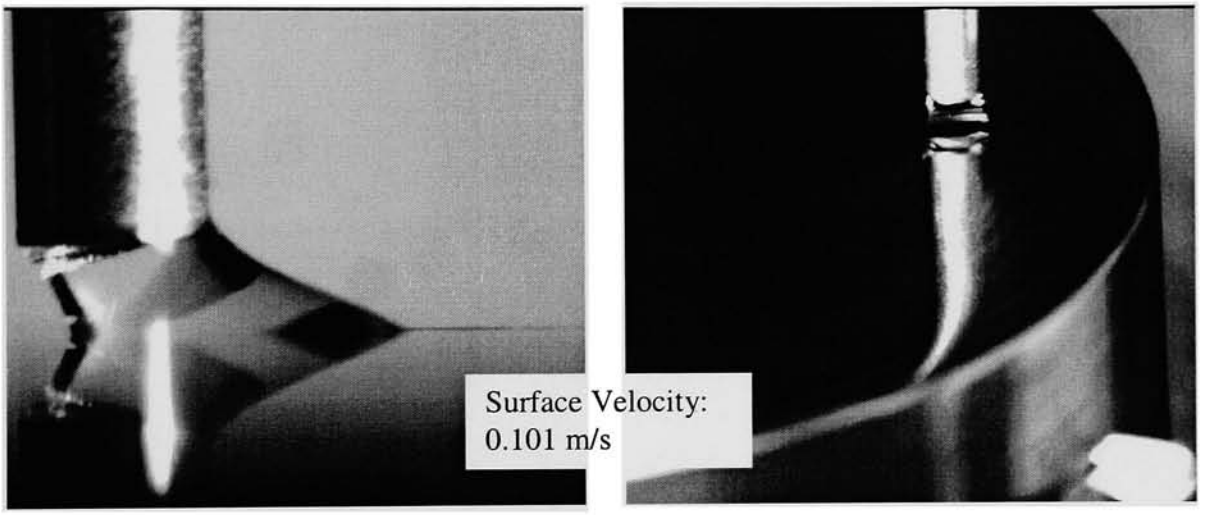
Surface Velocity:
0.101 m/s

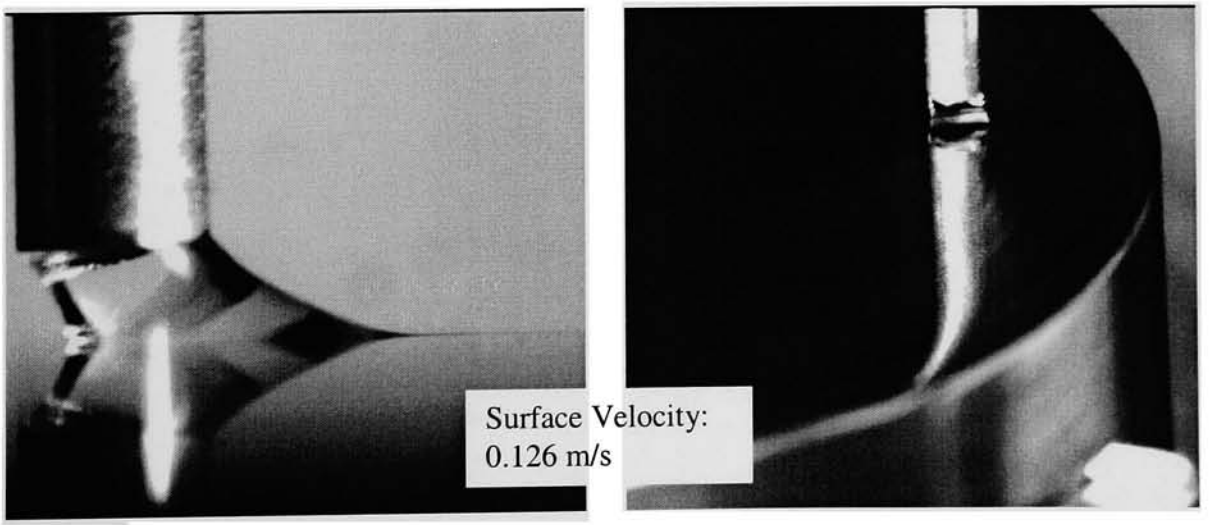
Surface Velocity:
0.126 m/s

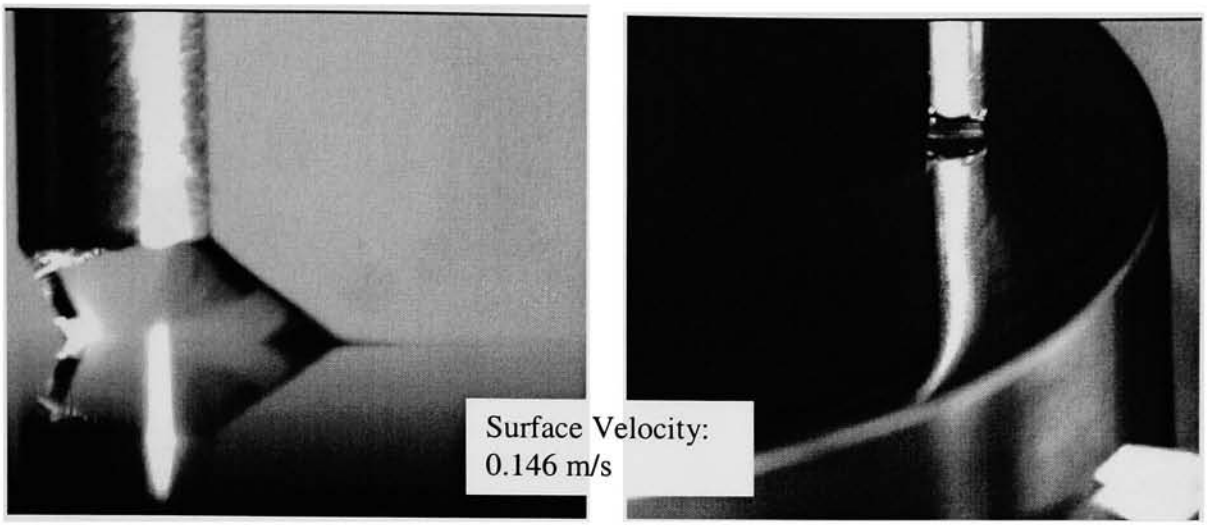
Surface Velocity:
0.146 m/s

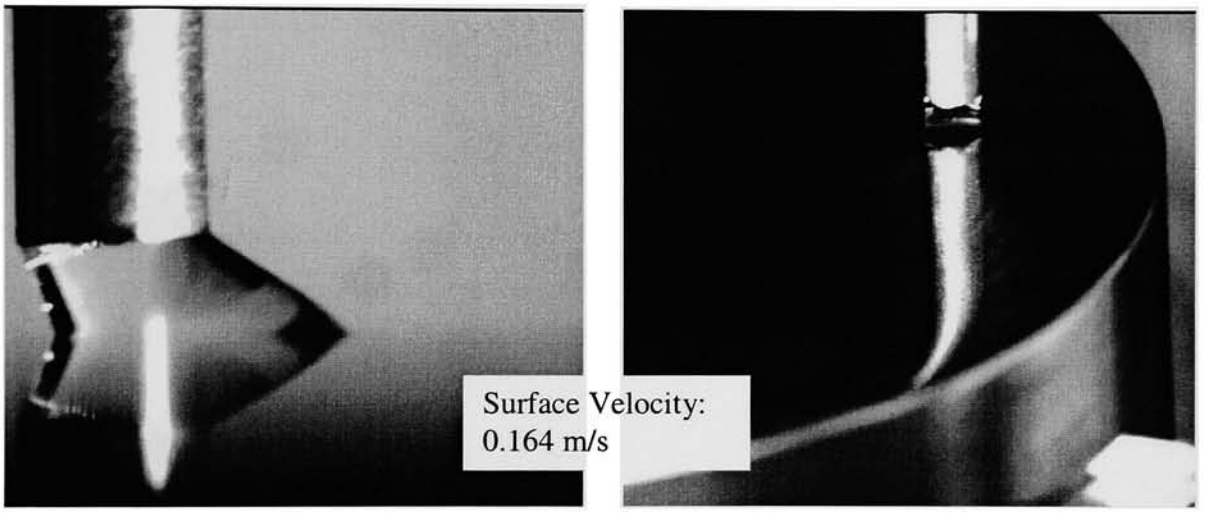
Surface Velocity:
0.164 m/s

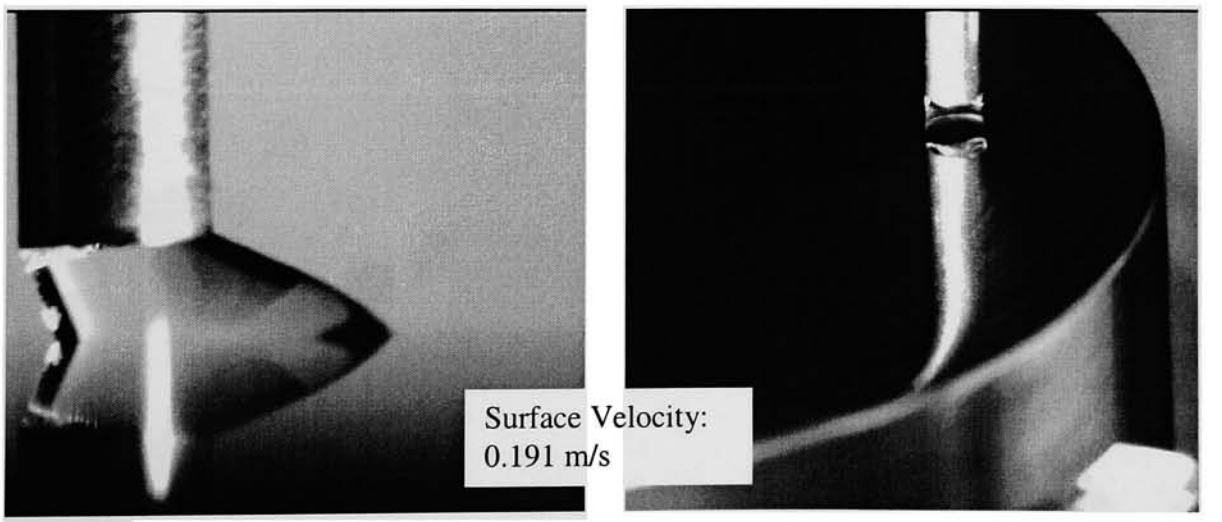
Surface Velocity:
0.191 m/s

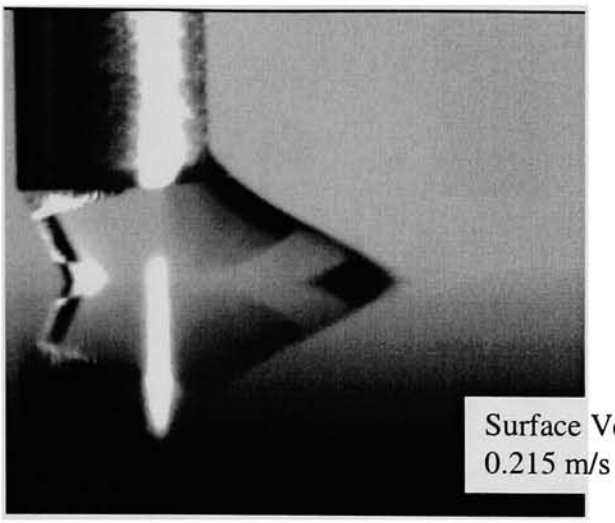
Surface Velocity:
0.215 m/s

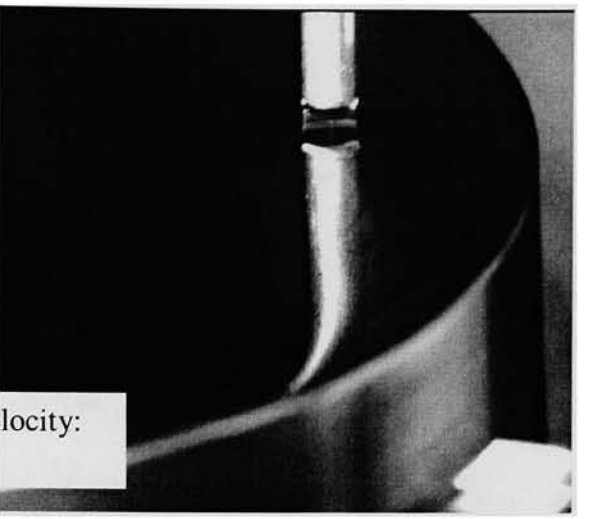

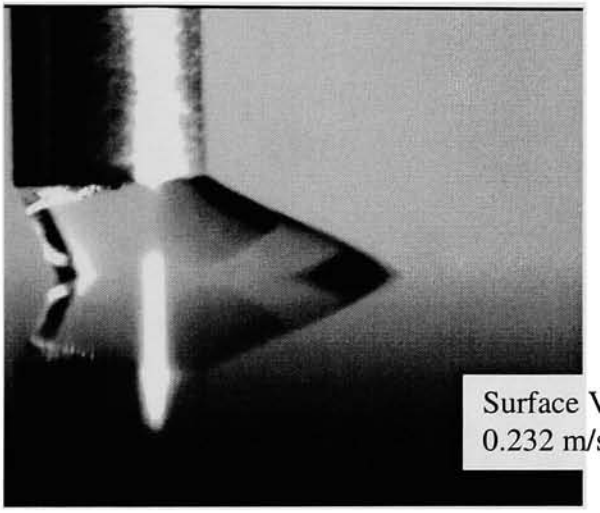
Surface Velocity:
0.232 m/s

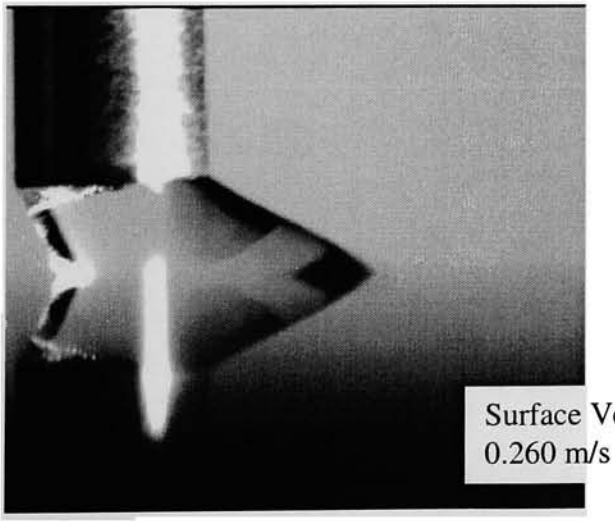
Surface Velocity:
0.260 m/s

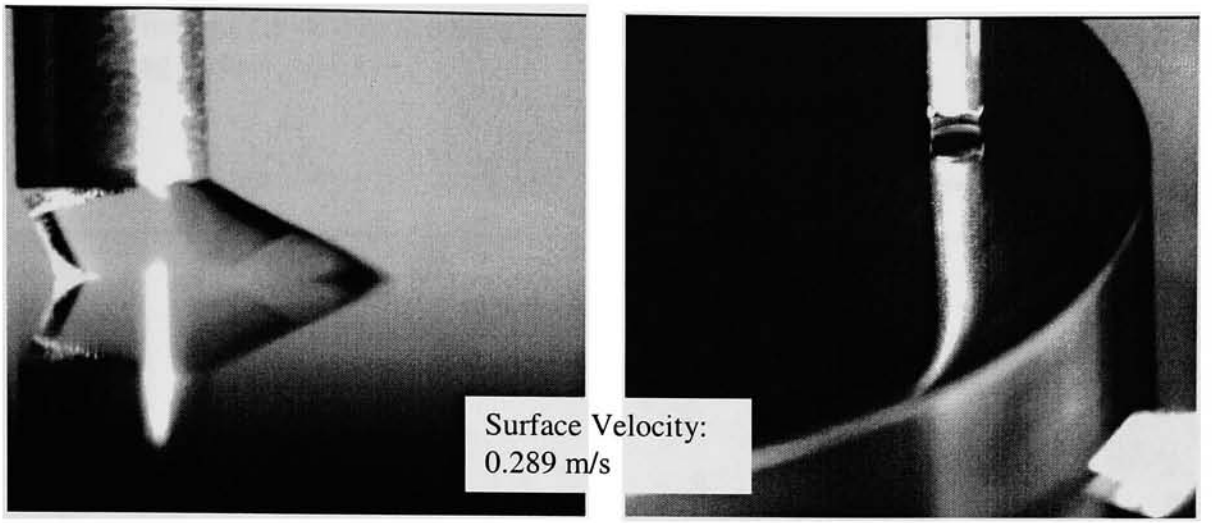
Surface Velocity:
0.289 m/s

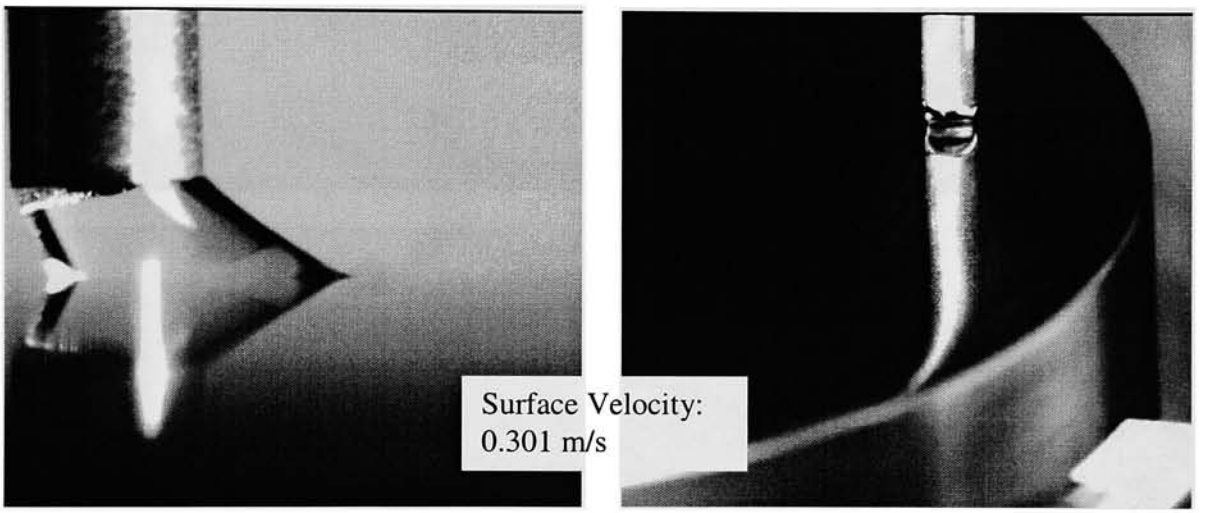
Surface Velocity:
0.301 m/s

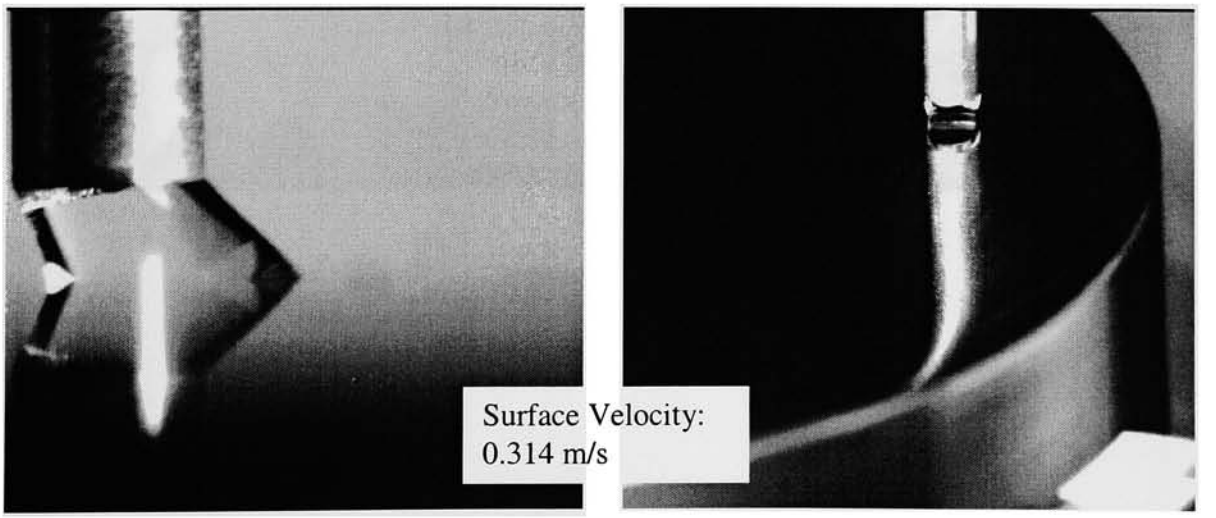
Surface Velocity:
0.314 m/s

Images of menisci for surface temperature of 107°C and water mass flow rate of 3.29E-7 kg/s with varying surface velocities.

Front View

Side View

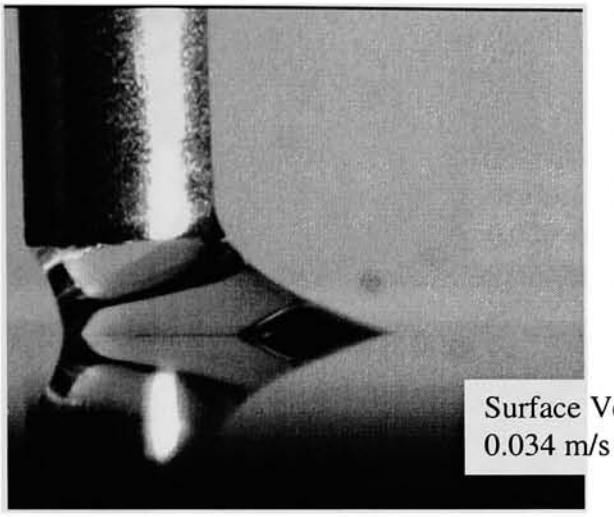

Surface Velocity:
0.034 m/s

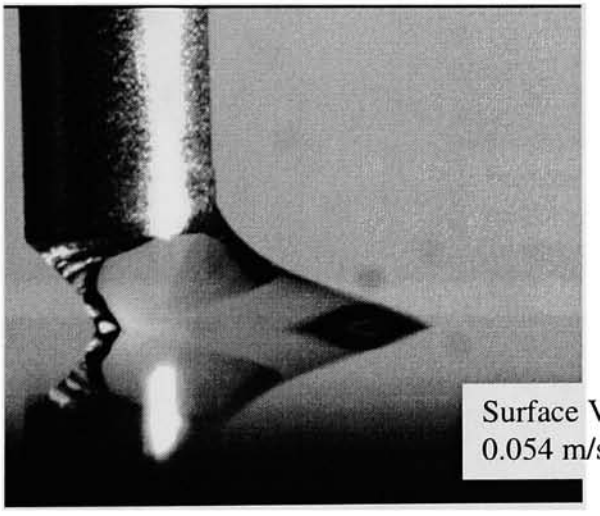

Surface Velocity:
0.054 m/s

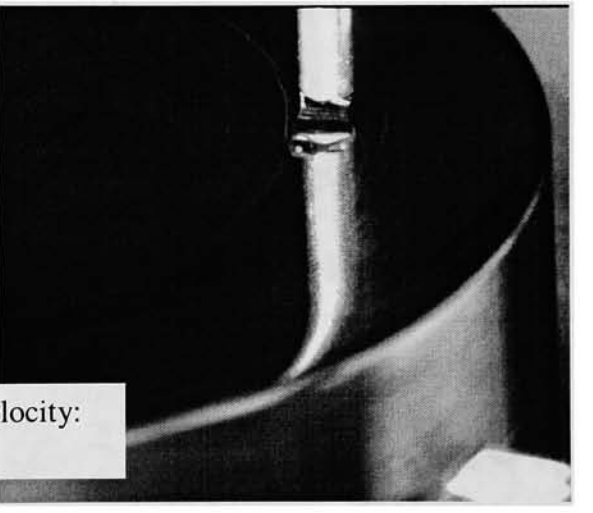

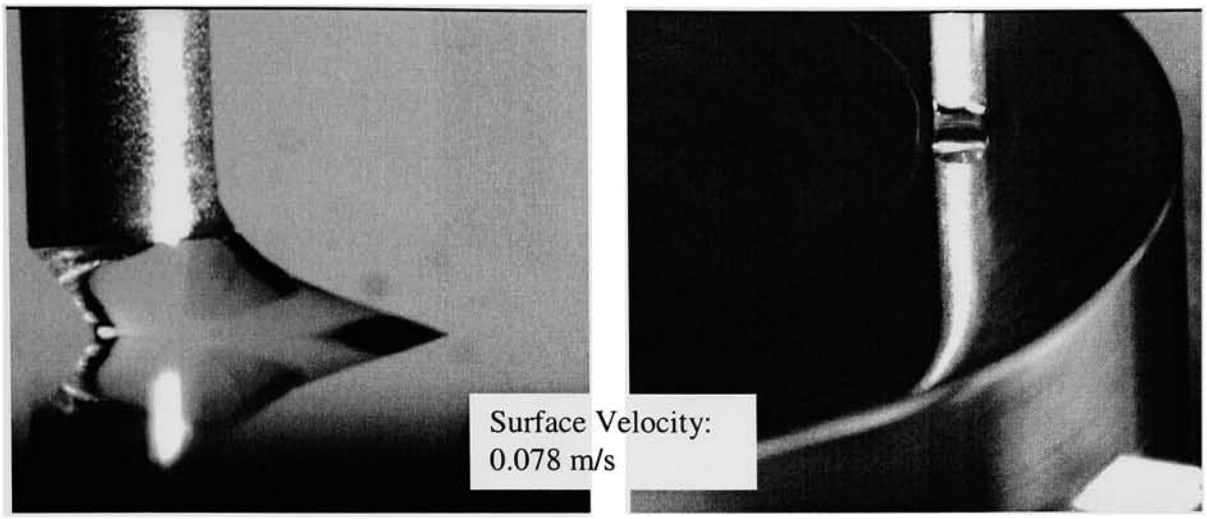
Surface Velocity:
0.078 m/s

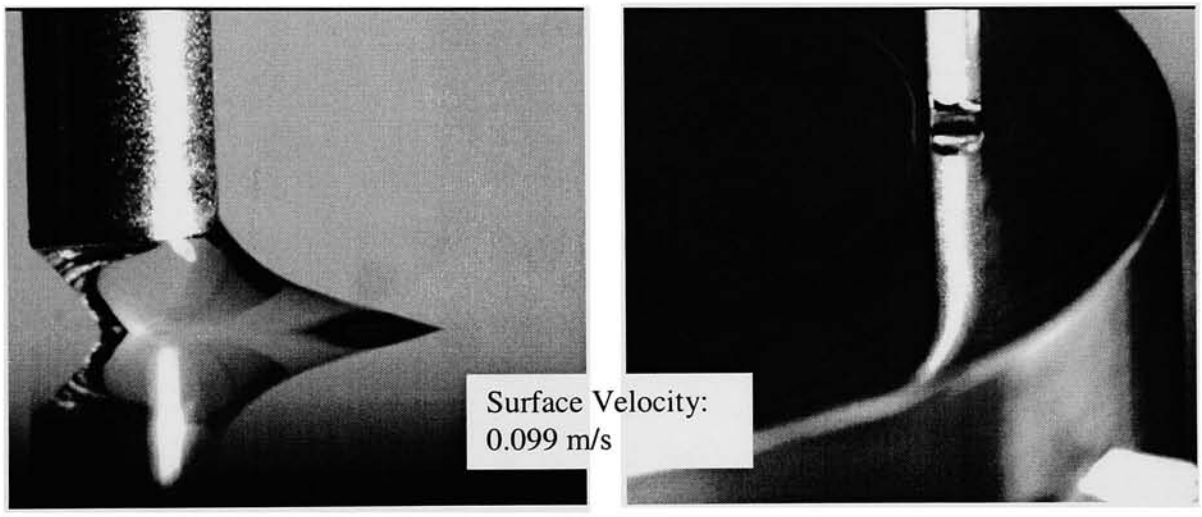
Surface Velocity:
0.099 m/s

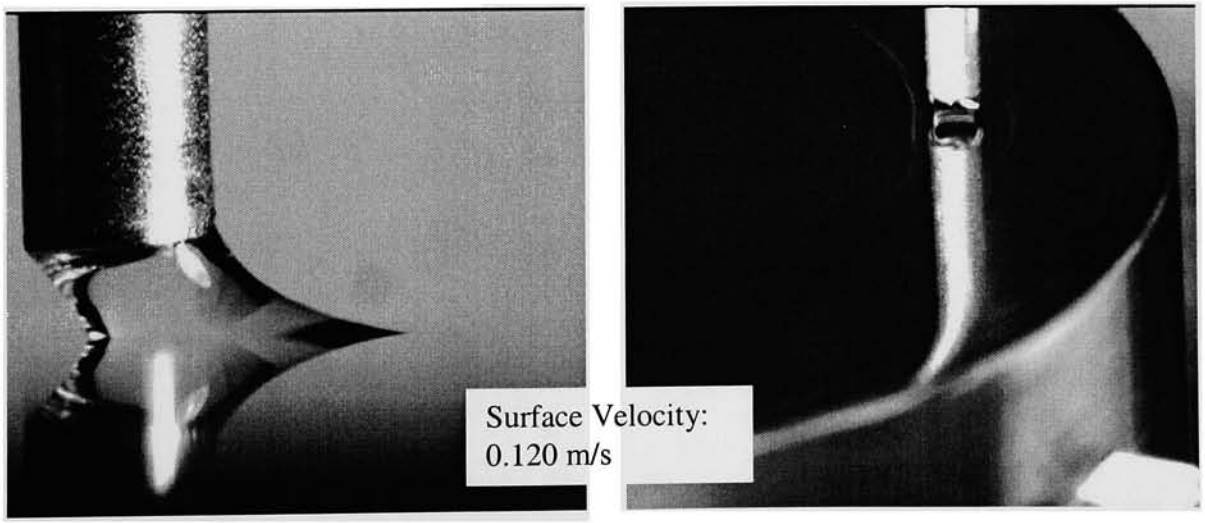
Surface Velocity:
0.120 m/s

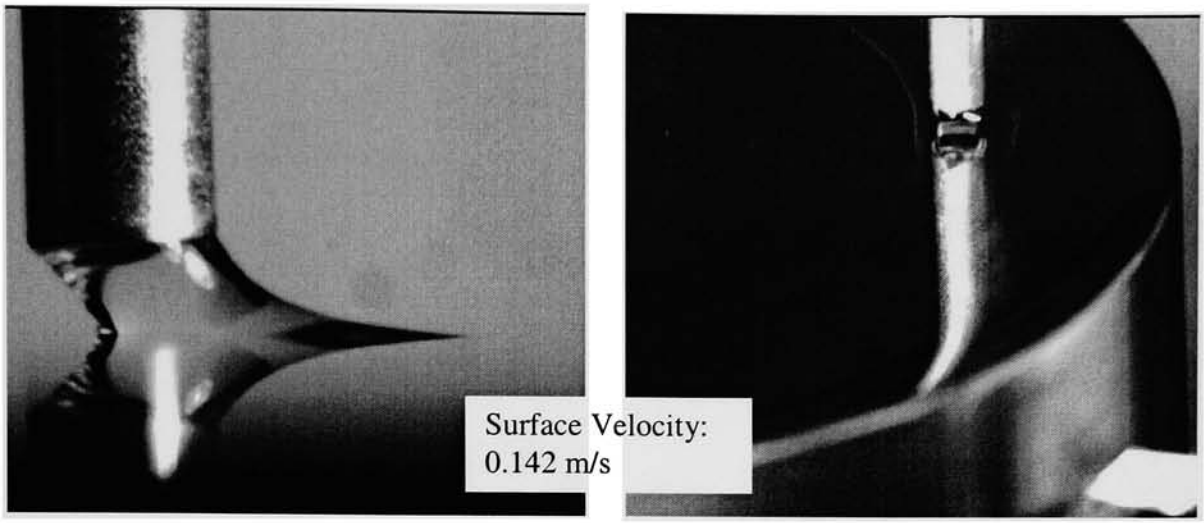
Surface Velocity:
0.142 m/s

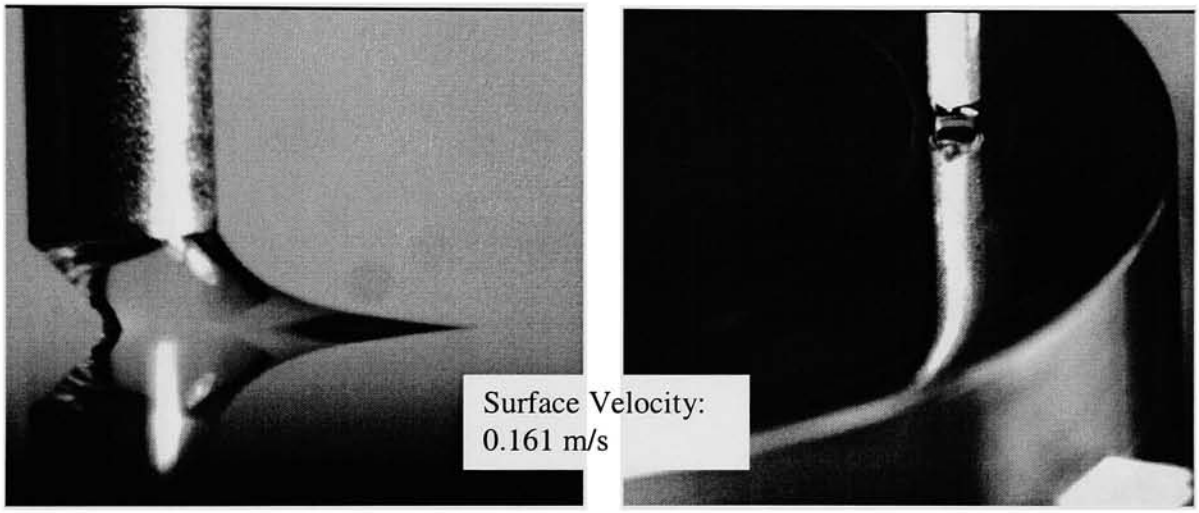
Surface Velocity:
0.161 m/s

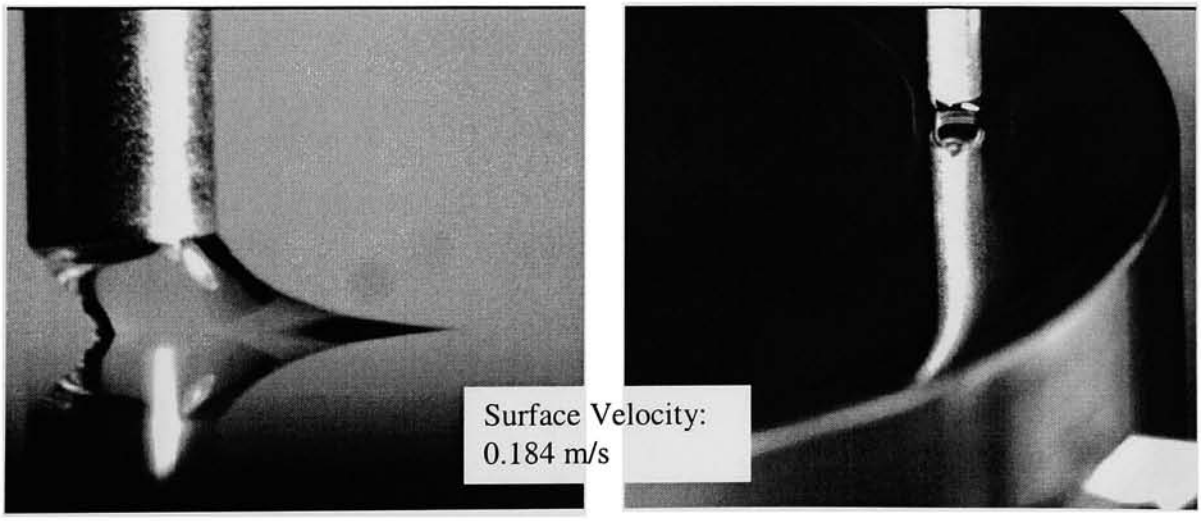
Surface Velocity:
0.184 m/s

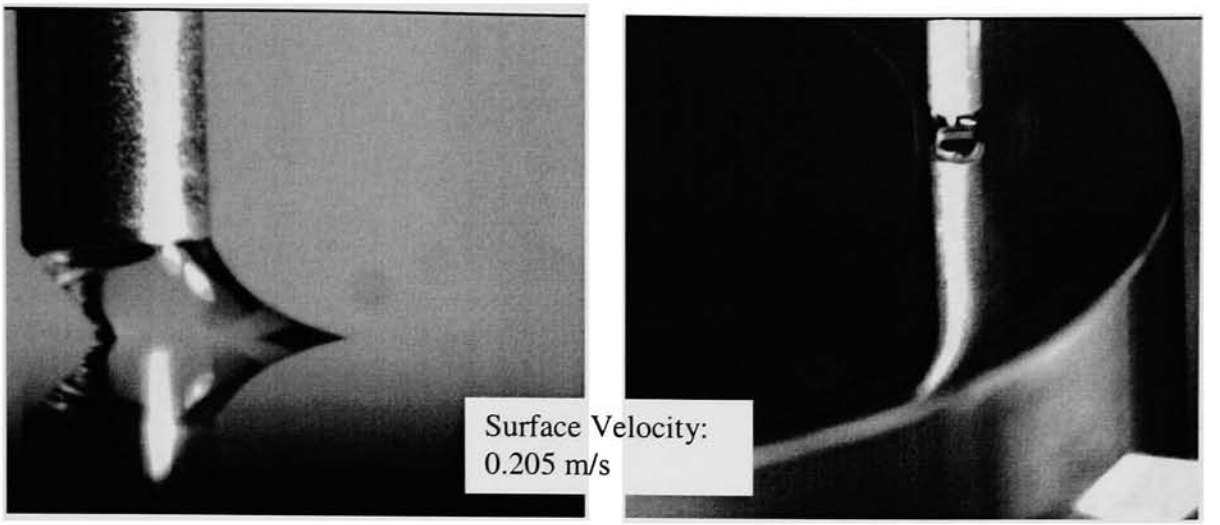
Surface Velocity:
0.205 m/s

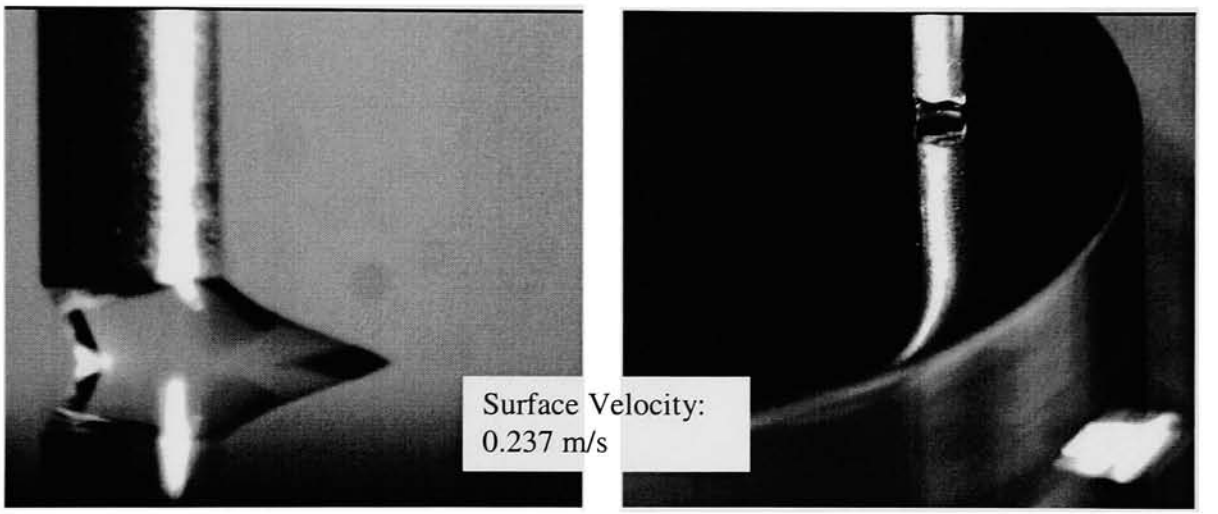
Surface Velocity:
0.237 m/s

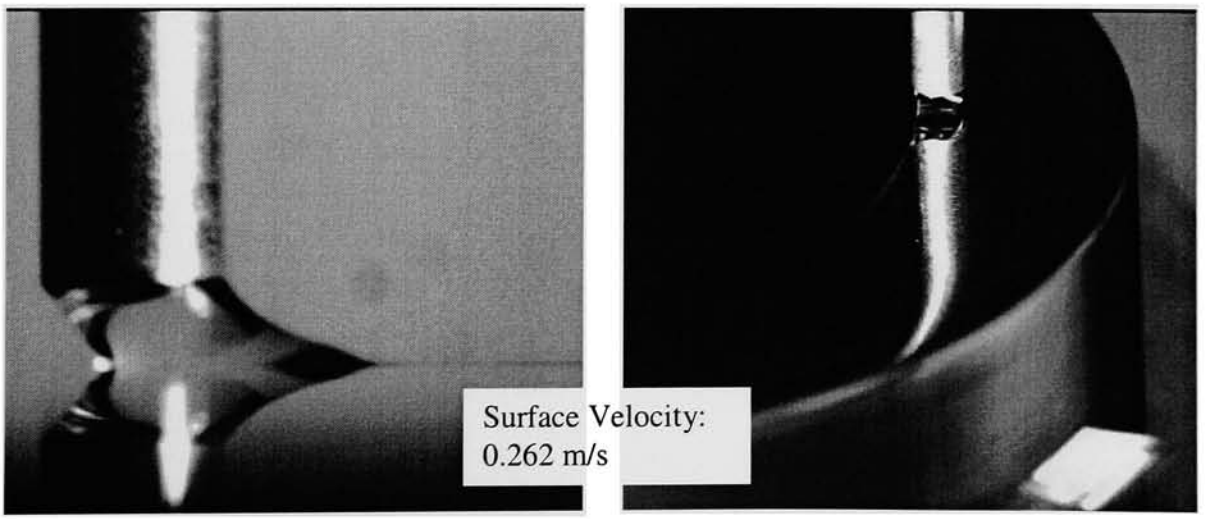
Surface Velocity:
0.262 m/s

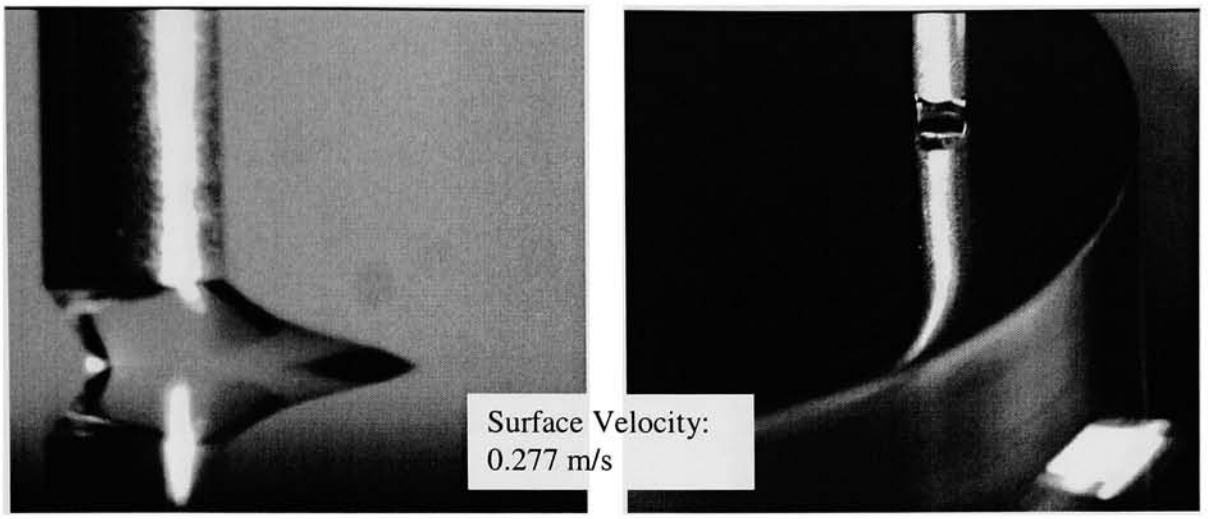
Surface Velocity:
0.277 m/s

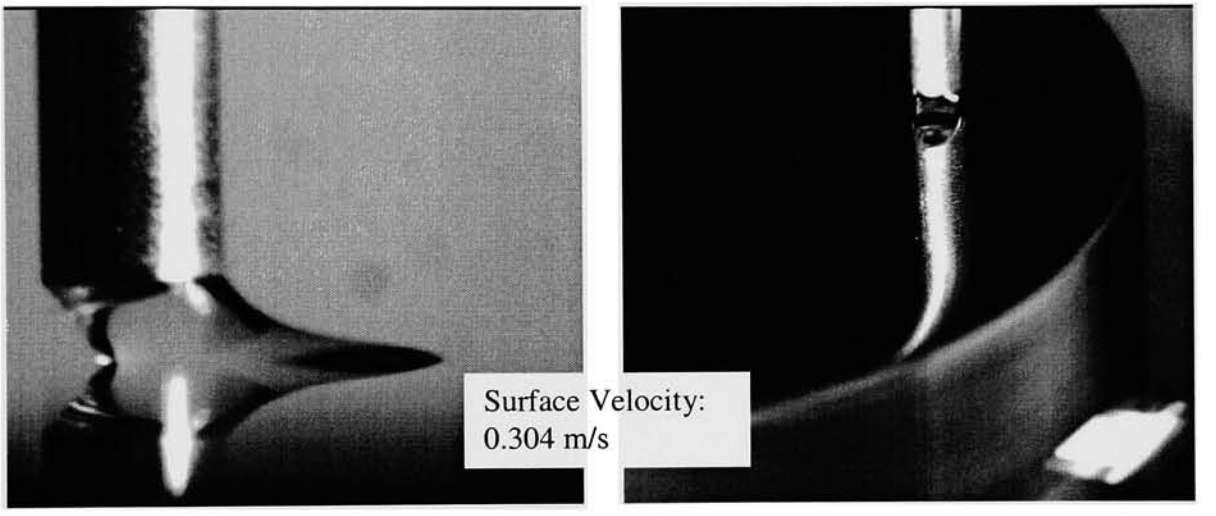
Surface Velocity:
0.304 m/s

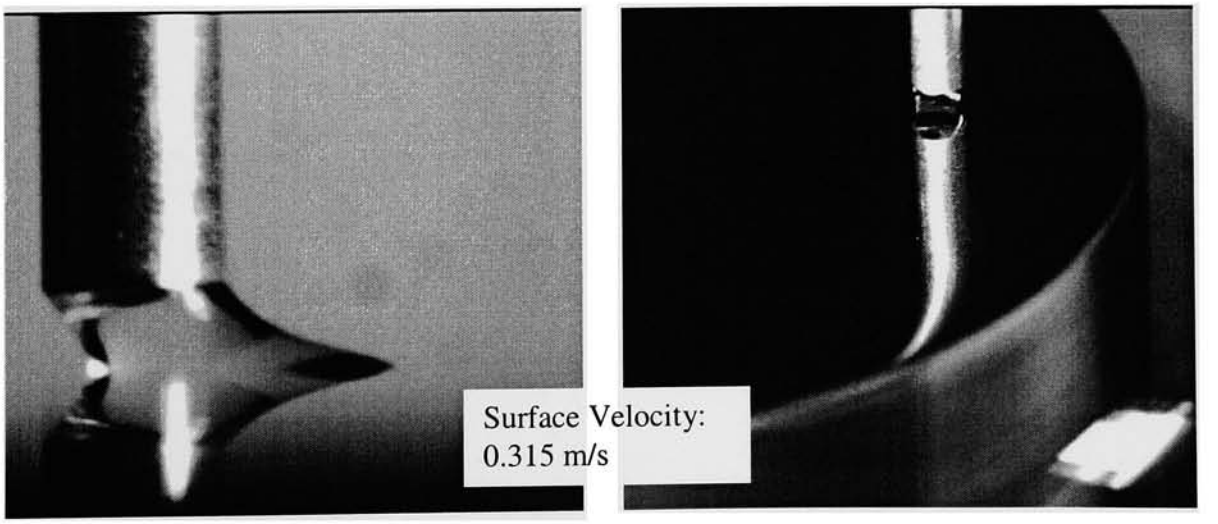
Surface Velocity:
0.315 m/s

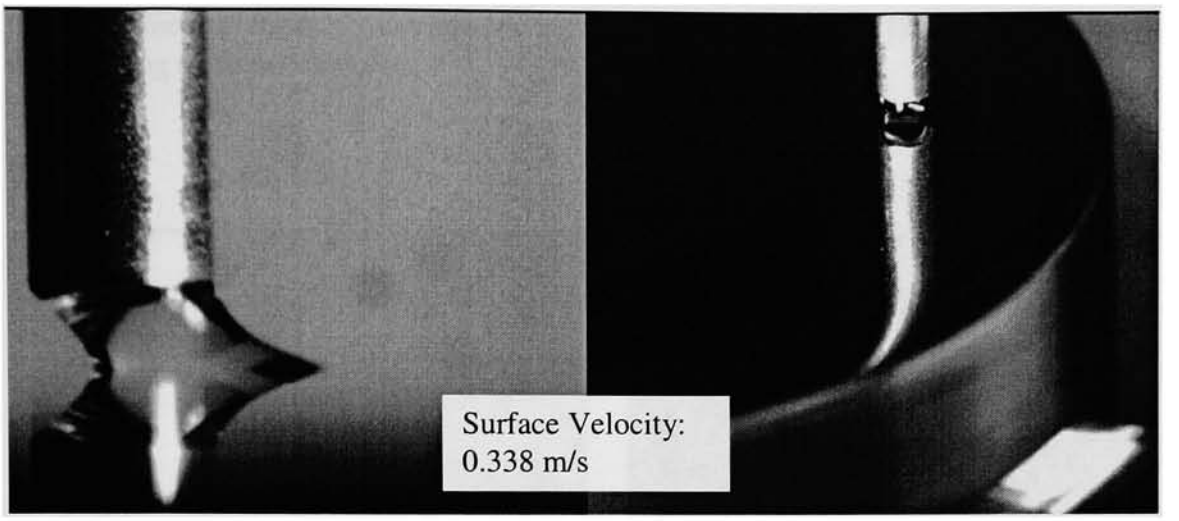
Surface Velocity:
0.338 m/s

Images of menisci for surface temperature of 107°C and water mass flow rate of 4.08E-7 kg/s with varying surface velocities.

Front View

Side View

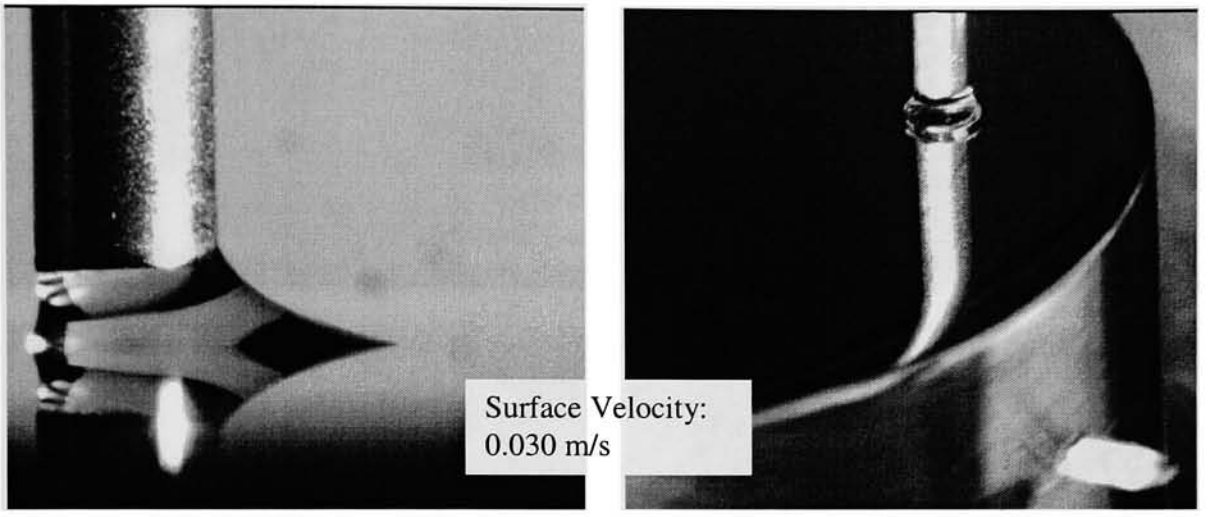

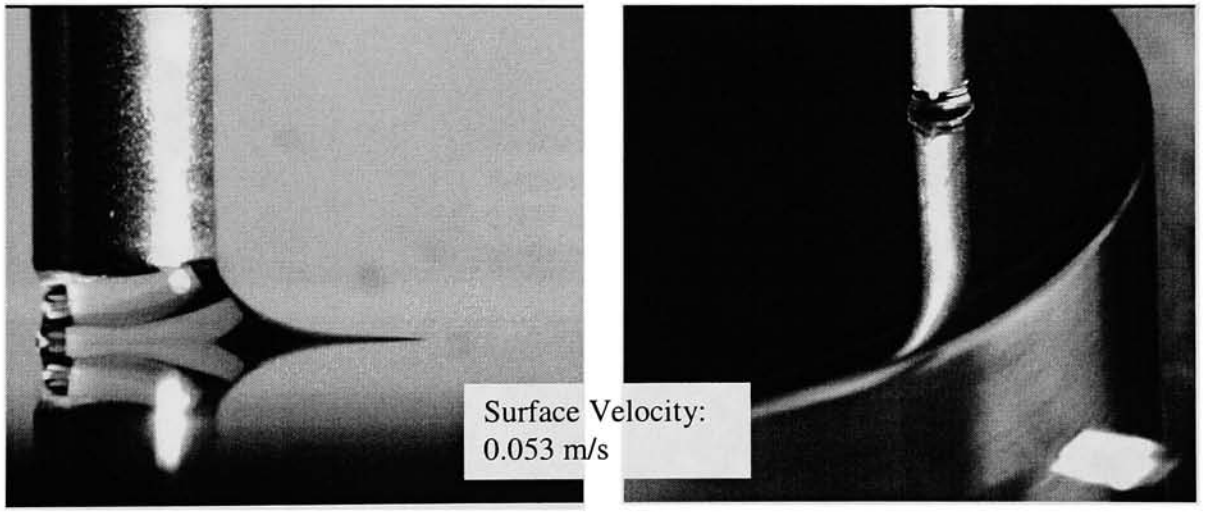

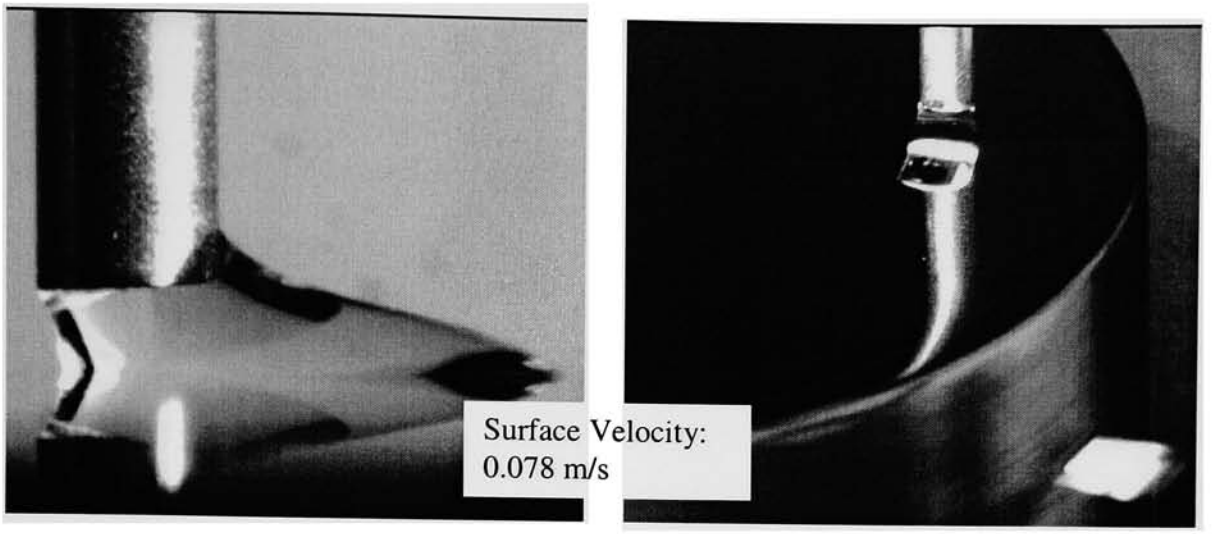
Surface Velocity:
0.078 m/s

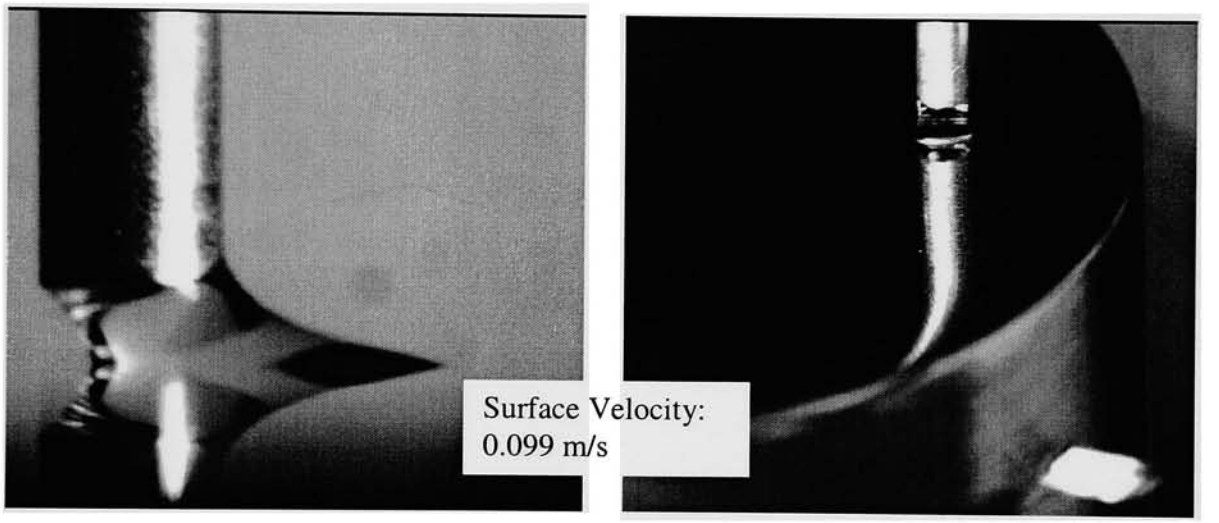
Surface Velocity:
0.099 m/s

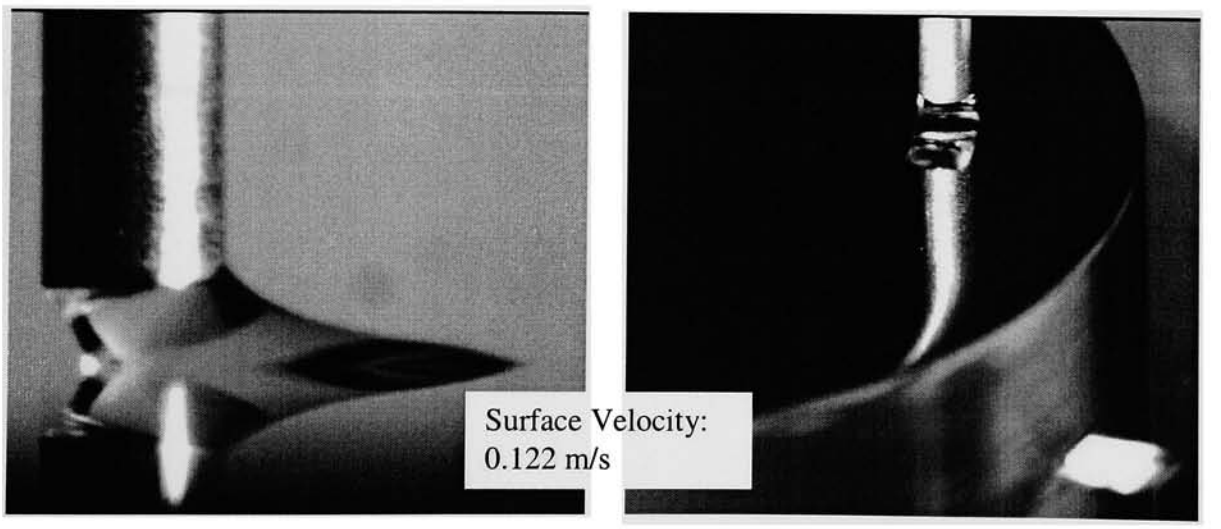
Surface Velocity:
0.122 m/s

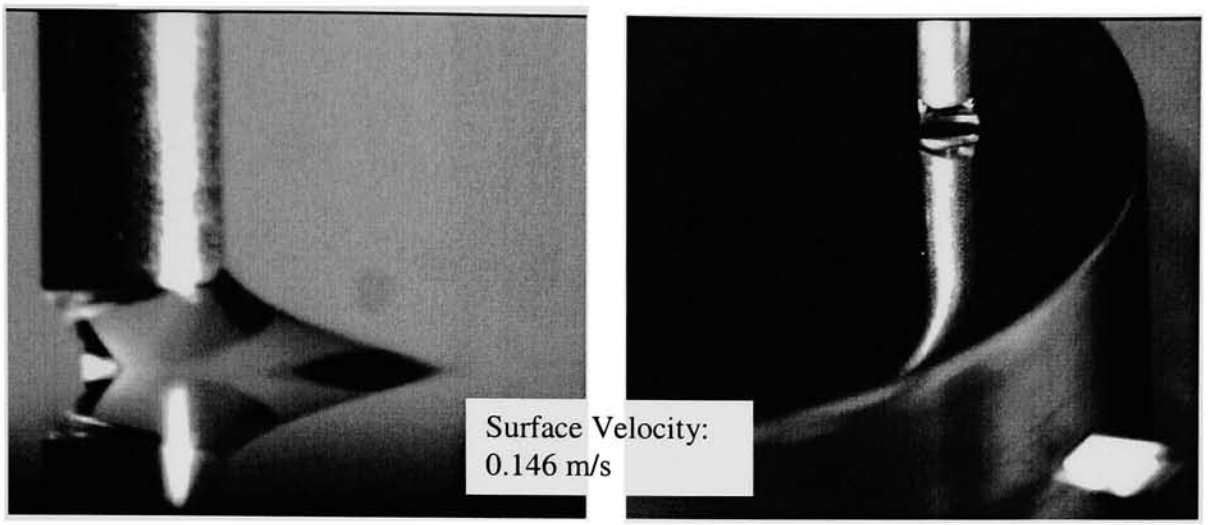
Surface Velocity:
0.146 m/s

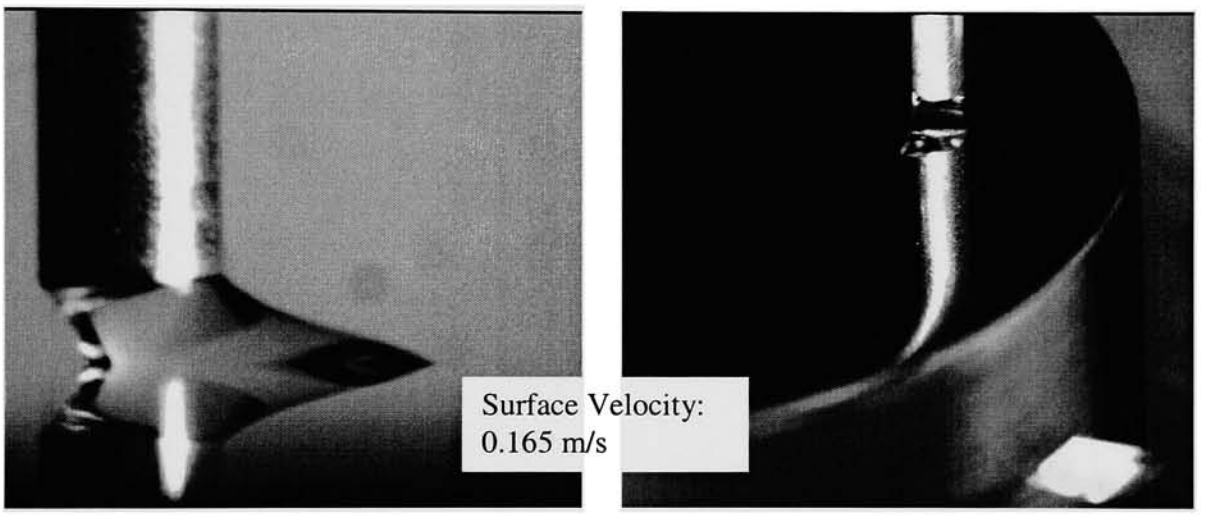
Surface Velocity:
0.165 m/s

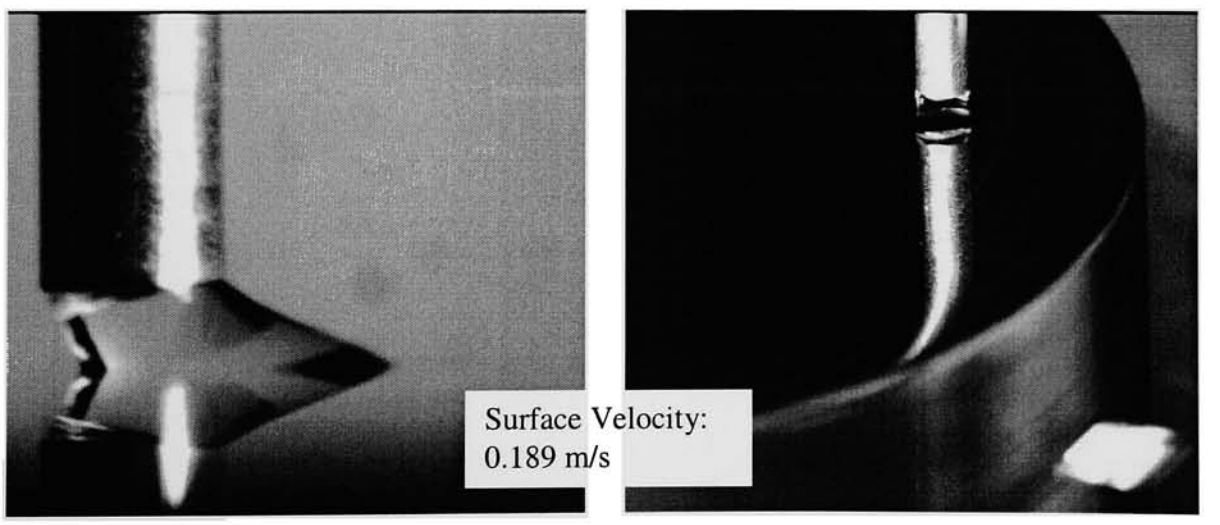
Surface Velocity:
0.189 m/s

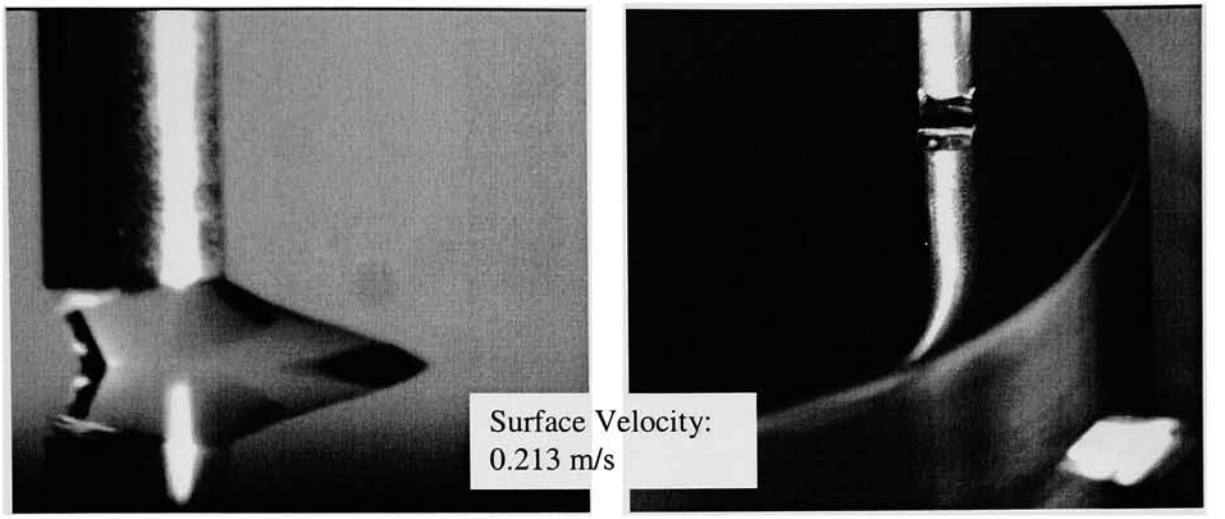
Surface Velocity:
0.213 m/s

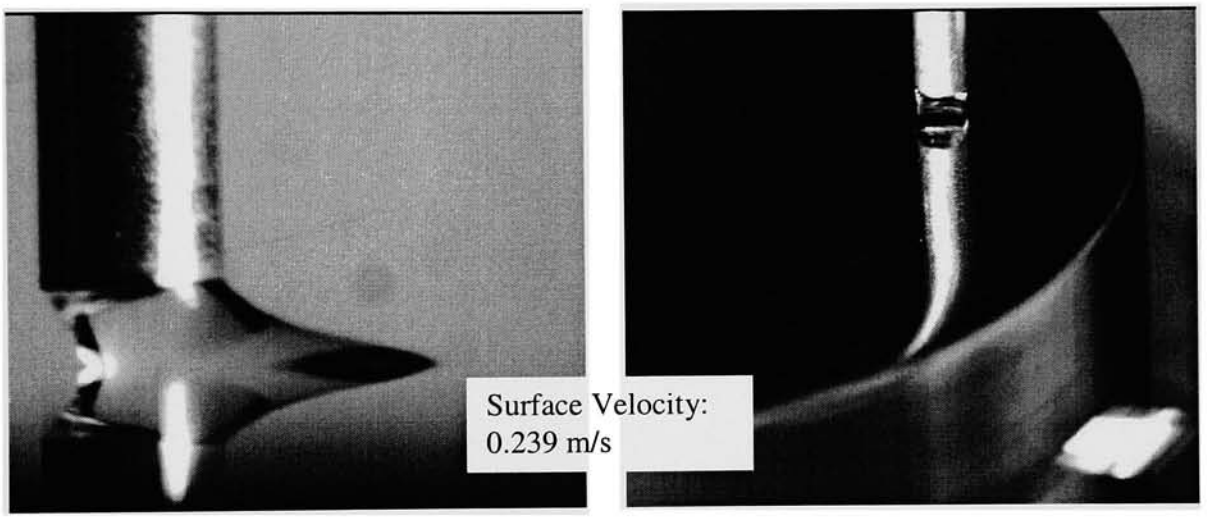
Surface Velocity:
0.239 m/s

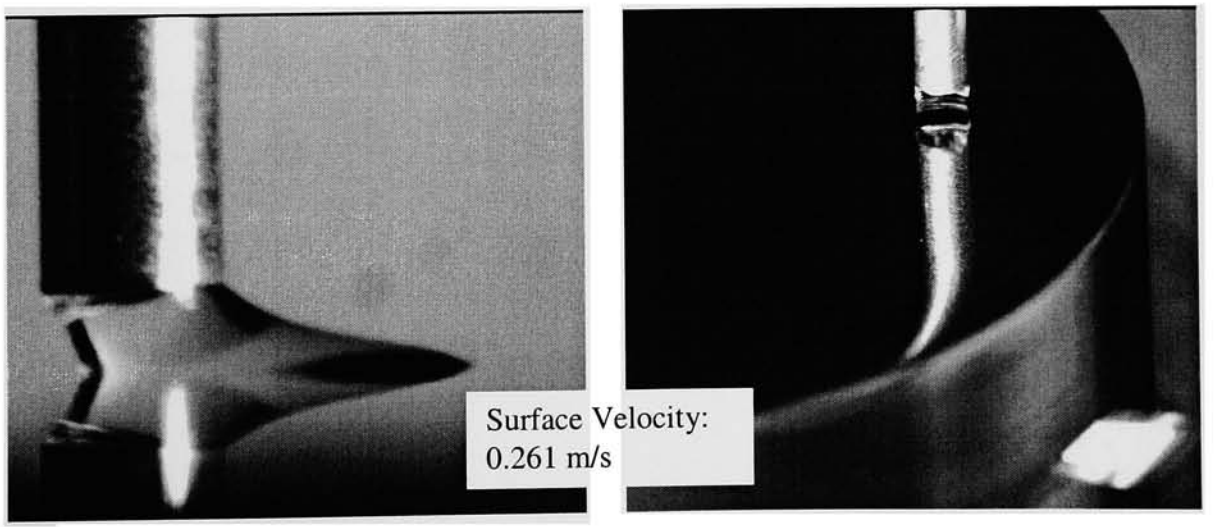
Surface Velocity:
0.261 m/s

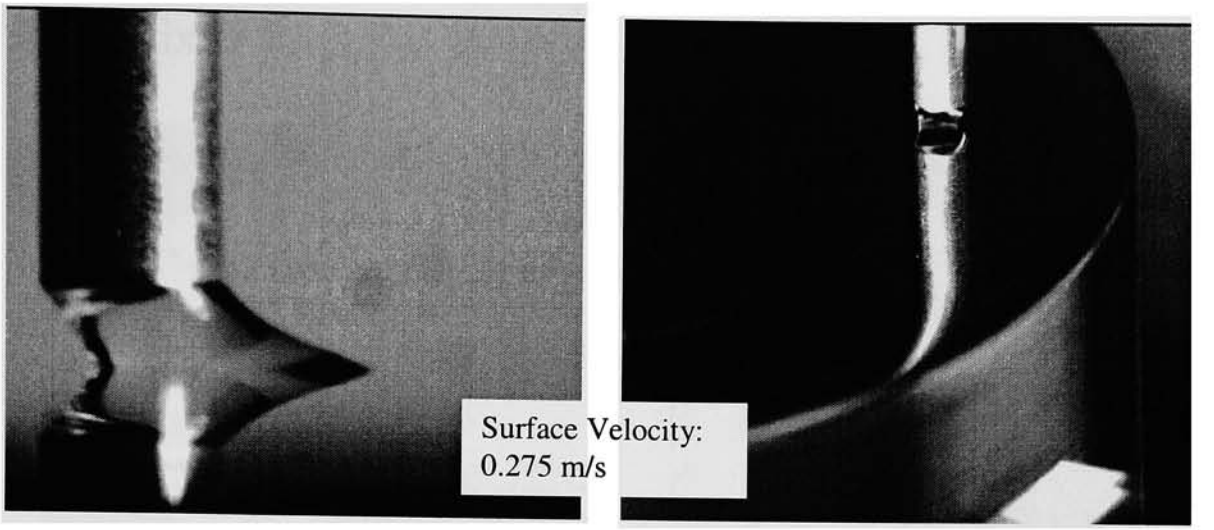
Surface Velocity:
0.275 m/s

Appendix D

GILMONT® Direct-Reading Variable Area Flowmeters

- PTFE and glass construction offers excellent chemical compatibility
- Wide selection of flow ranges—measure air from 0.02 mL/min to 675 LPM or water from 0.0002 mL/min to 20 LPM.
- Accuracy is ±5% of reading or 2 mm of the scale length, whichever is greater.

Unshielded Flowmeters are ideal for high purity and corrosion resistance in low-pressure applications. Fluid contacts only the borosilicate glass tube, PTFE body, and O-rings of Viton® fluoroelastomer. Glass taper joints are available to facilitate connection to other glassware, call for more information.

Shielded Flowmeters are great for higher pressure applications. The clear polycarbonate shield adds strength and protects the tube from damage. Fluid contacts only the borosilicate glass tube, PTFE body, and O-rings of Viton® fluoroelastomer—not the polycarbonate shield. End bushings are polypropylene with PTFE inserts. Order coupling adapters (below) to prevent fluid from contacting the end bushings. Meters accept ⅜" ID tubing over Teflon® inserts (sizes 14 and 15 accept ½" ID tubing).

Shielded Flowmeters with Valves offer greater control; micrometer capillary valves ensure precise, reproducible measurement and flow control. Valve consists of a glass tube and a precision-ground rod of Kel-F® (PTFE for sizes 14 and 15). This 20-turn micrometer valve can be adjusted from 0.1 to 100% of maximum flow giving you precise flow control. Meters accept ⅜" ID tubing over Teflon® inserts (sizes 14 and 15 accept ⅝" ID tubing).

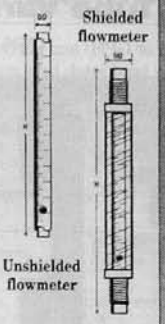

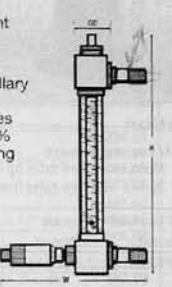

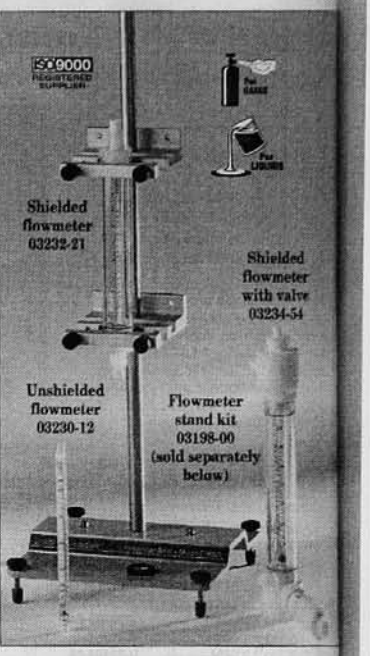

Dimensions

Tube size(s)	Unshielded	Shielded	Shielded with valves
10, 11, 12, 13	5⅛"H x ⅜"OD 5⅛"H x ⅝"OD	8"H x 1"OD	8⅛"H x 6"W x 1¾"OD
14, 15	5½"H x 1⅛"OD 5½"H x ⅞"OD	9¾"H x 1½"OD	11"H x 7"W x 1⅝"OD

Tube size	Floats* included	Flow rate Air (mL/min)	Flow rate Water (mL/min)	Unshielded flowmeters Catalog number	Max psi	Price	Shielded flowmeters Catalog number	Ports NPT(M)	Max psi	Price	Shielded flowmeters with valves Catalog number	Ports NPT(M)	Max psi	Price
10	Glass 316 SS	0.2-90 0.36-160	0.002-1.1 0.004-2.3	U-03230-10	15	$96.00	U-03232-20	¼"	125	$147.00	U-03234-51	¼"	125	$358.00
11	Glass 316 SS	1-280 2-500	0.01-4.0 0.02-8.6	U-03230-11	15	84.00	U-03232-21	¼"	125	135.00	U-03234-52	¼"	125	351.00
12	Glass 316 SS	20-2100 36-3700	0.4-40 0.86-86	U-03230-12	15	77.00	U-03232-22	¼"	100	128.00	U-03234-53	¼"	100	348.00
13	Glass 316 SS	200-14,000 360-25,000	2-300 4-640	U-03230-13	15	67.00	U-03232-23	¼"	75	126.00	U-03234-54	¼"	75	332.00
14	Glass 316 SS	1000-36,000 1800-64,000	10-850 21-1820	U-03230-14	15	121.00	U-03232-24	½"	60	196.00	U-03234-56	¼"	60	550.00
15	Glass 316 SS	3000-77,000 5300-137,000	30-1900 64-4100	U-03230-15	15	127.00	U-03232-25	½"	50	207.00	U-03234-57	¼"	50	559.00

Note: For pressure drop of each flowmeter, please call our Application Specialists. *When using the stainless steel float, refer to the correlation chart (included) for proper readings.
Kel-F—Reg TM 3M Co. Teflon—Reg TM E.I. DuPont de Nemours & Co. Viton—Reg TM DuPont Dow Elastomers L.L.C.

Accessories

Flow Rate Analysis Software generates accurate flow rate tables specific to your fluid, temperature, pressure, density, and viscosity using factory calibration data for the specific Gilmont® flow tube used.

U-32120-10 Flow rate analysis software runs with Windows® 95/98/NT computers; CD-ROM $50.00

Windows—Reg TM Microsoft Corp.

Flowmeter Stand Kit contains everything you need to mount your Gilmont® flowmeter on a benchtop or a wall. Mount valved flowmeters directly—base accepts two large flowmeters (size 14 or 15) or three of the smaller flowmeters.

U-03198-00 Flowmeter stand kit. Includes one base, one rod, and two mounting clamps $170.00
U-03198-10 Replacement flowmeter base $70.00
U-03198-20 Replacement rod, 18"L $25.00
U-03198-30 Replacement mounting clamp $40.00

Direct-Reading Flowmeter Kit comes complete with flowmeters, glass floats, 316 stainless steel floats, and instructions. Unshielded flowmeter kits can be used with flexible tubing or PTFE coupling adapters (below). Shielded flowmeter with valve kits contain one interchangeable shield and valve assembly.

Catalog number	Flow range (mL/min) Air	Flow range (mL/min) Water	Flowtube sizes included	Price
Unshielded flowmeters				
U-03230-00	0.2-25,000	0.002-640	10, 11, 12, and 13	$289.00
U-03230-60	1000-137,000	10-4100	14 and 15	218.00
Shielded flowmeters with valves				
U-03234-59	0.02-160	0.0002-2.3	10	431.00
U-03234-55	1-25,000	0.01-640	11, 12, and 13	460.00
U-03234-58	1000-137,000	10-4100	14 and 15	636.00

Coupling Adapters are for use with unshielded flowmeters.

U-03198-40 PTFE coupling adapter, ¼" NPT(F) $42.00/ea
U-03198-42 PTFE coupling adapter, ½" NPT(F) $47.00/ea

Infrared Heating Lamp

Ideal for drying paint and other surface coatings

Mount to any table or benchtop, or use our floor stands to support the heating lamp—features durable all-metal construction. Adjust the 42" swiveling extension arm to position lamp exactly where you want it. Dual reflector prevents excessive heat buildup.

03057-00

What's included: a screw-type mounting bracket; 10-ft grounded cord with plug; and a 250 watt infrared bulb. Easily remove wire bulb guard to replace bulb (order replacement bulb below).

U-03057-00 Infrared heating lamp; 115 VAC, 50/60 Hz. Shpg wt 6 lb (2.7 kg).....**$155.00**

U-03057-01 Replacement bulb, 250 watt **$19.00**

U-03057-50 Floor stand with caster base, 38½"H., Shpg wt 22 lb (10.0 kg).....**$105.00**

U-03057-52 Floor stand with pedestal base. Shpg wt 28 lb (12.7 kg).....**$85.00**

Milwaukee® Heavy-Duty Heat Guns

Cole-Parmer® Introduces

Built-in support stand allows hands-free use—keeps heat gun stationary for work-bench or assembly work

Choose either a dual temperature model with 3 position rocker switch or a variable temperature model. Heat gun kits include a high-impact carrying case and four accessory nozzles: air reduction nozzle for intensified heating in specific areas, hook nozzle for surrounding pipe or tubing, deflector for deflecting hot air from glass, and air spreader for less intense heating.

03060-00

Specifications & Ordering Information

Air volume: 14.8 cfm
Amps: 11.6
Power: 120 VAC

Shpg wt
Heat gun only: 2 lb (1.0 kg)
Heat gun kit: 6 lb (2.8 kg)

Temperature	Heat gun only		Heat gun kits	
	Catalog number	Price	Catalog number	Price
570°F and 1000°F	U-03060-00	$75.00	U-03060-10	$125.00
140 to 1040°F	U-03060-02	103.00	U-03060-12	147.00

Milwaukee—Reg TM Milwaukee Electric Tool Corporation

Industrial-Grade Heat Guns

A Dual-Temperature Heat Guns

Flameless heat—ideal for heat-shrink tubing, drying specimens, or controlling heat treatment of samples

Industrial-grade heat guns feature two fixed temperature settings. Guns are powerful enough to produce an air velocity of 3000 ft/min and an air volume of 23 cfm—great whenever you need fast, flameless heat. An adjustable air intake controls air blast temperature (measured 1" from the nozzle of the heat gun). Heat guns measure 8"L x 9½"H, and include a 6-ft neoprene-jacketed cord, only the 120 VAC units include a plug.

03020-00

Order attachments and replacement heating element kits separately below.

Specifications & Ordering Information

Catalog number	Temperature	Watts	Power VAC, Hz	Shpg wt lb (kg)	Price
U-03020-00	200/300°F (93/149°C)	600	120, 50/60	5 (2.3)	$102.00
U-03021-00		600	230, 50/60		102.00
U-03022-00	300/500°F (149/260°C)	1440	120, 50/60	5 (2.3)	102.00
U-03023-00		1440	230, 50/60		102.00
U-03024-00	500/750°F (260/399°C)	1680	120, 50/60	5 (2.3)	102.00
U-03025-00		1680	230, 50/60		102.00
U-03028-00	750/1000°F (399/538°C)	1740	120, 50/60	5 (2.3)	102.00
U-03029-00		2160	230, 50/60		102.00

Airflow Attachments for A and B.

U-03026-12 Shrink-tubing baffle for tubing up to ¾" OD.....**$14.80**

U-03026-18 Pinpoint adapter attachment, ¼" opening.....**$21.75**

U-03026-19 Shrink-wrap baffle, 8" wide.....**$47.50**

B Variable-Temperature Heat Guns

Use to heat-shrink tubing, activate adhesives, bend/form plastics, and more

When you need portable, flameless heat fast use variable-temperature heat guns. These heat guns feature a control knob to let you regulate temperatures and hold them constant. Handgrip has a safety switch guard. Guns measure 8"L x 9½"H and come supplied with a 6-ft cord; the 120 VAC unit also includes a plug. Shpg wt 5 lb (2.3 kg).

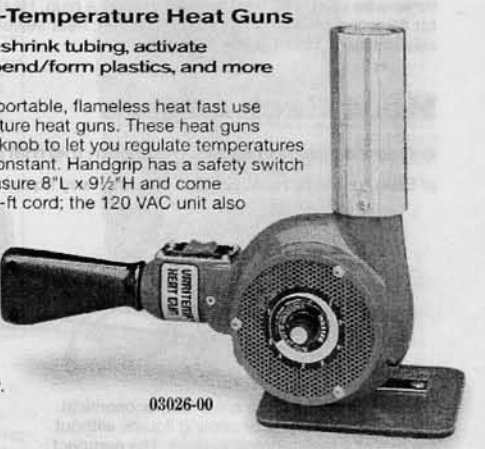

03026-00

Order attachments and replacement heating element kits separately below.

Specifications & Ordering Information

Catalog number	Temperature °F (°C)	Watts	Power	Air velocity, volume	Price
U-03026-00	72 to 1000 (22 to 537)	1740	120 VAC, 60 Hz	2200 ft/min, 17 cfm	$145.50
U-03026-01	72 to 750 (22 to 398)	1680	230 VAC, 50/60 Hz	2800 ft/min, 21cfm	151.00

Replacement Heating Element Kits for A and B.

Each element kit includes heating element, mica insulator, nozzle screen, all parts necessary for installation, and instructions.

Cat. no.	For gun	Price	Cat no.	For gun	Price
U-03020-60	03020-00	$25.65	U-03026-02	03024-00	$25.65
U-03021-60	03021-00	25.65	U-03026-03	03025-00	25.65
U-03022-60	03022-00	25.65	U-03028-60	03028-00	25.65
U-03023-60	03023-00	25.65	U-03029-60	03029-00	25.65
U-03028-60	03026-00	25.65	U-03026-03	03026-01	25.65

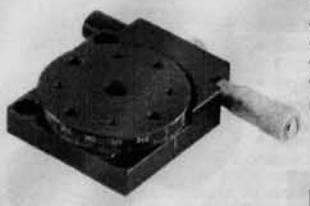

METRIC ROTARY STAGES

- Low Profile
- Smooth Micrometer Movement
- Black Anodized Aluminum Construction
- 360° Coarse Rotation, 2° Increments

SPECIFICATIONS

	Total Fine Rotation	Total Travel/Knob Rotation
40mm	12°	40min.
60mm	10°	24min.

Rotary Stages	Stock No.	Prices		
		1-4	5-9	10+
40mm Precision Rotary Stage	A55-028	$231.00	$219.40	Call
60mm Precision Rotary Stage	A55-029	$294.40	$279.70	

Adapter Plates	Stock No.	Prices		
		1-9	10-19	20+
40mm Adapter Plate	A55-037	$23.10	$21.90	Call
60mm Adapter Plate	A55-038	$25.90	$24.60	

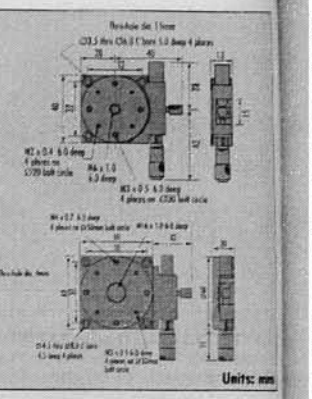

METRIC ROTARY STAGE

- Smooth, Manual Adjustment
- 360° Coarse Movement, 1° Increments
- Accepts Metric Posts When Used with Thread Adapter #A55-036 (Pg. 163)
- Sturdy, Black Anodized Aluminum Construction

Description	Stock No.	Prices		
		1-4	5-9	10+
Metric Rotary Stage	A55-030	$161.70	$153.60	Call

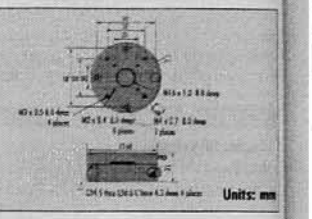

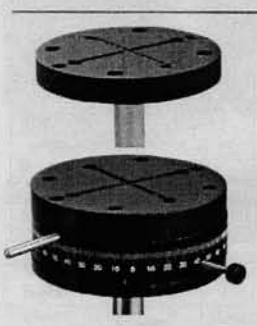

ROTARY MOUNTING BASE PLATE

The 3" dia. base is an ideal mounting surface for optical components. Plate attaches to the top of the Rotary Holder with two 4-40 mounting screws (included). Base plate is constructed of black anodized aluminum and features both mounting holes and slots for various positioning requirements. Both accessory plates can be used in conjunction with the rotary mount for an endless number of optical alignment applications where smooth rotation is required (scale is in 1° increments). The complete assembly can then be mounted either horizontally or vertically. Total assembly thickness is 1.3".

Description	Stock No.	Prices		
		1-9	10-19	20+
3" Mounting Base Plate	A03-678	$28.00	$26.60	Call
Rotary Mount Assembly	A53-026	$134.50	$127.70	

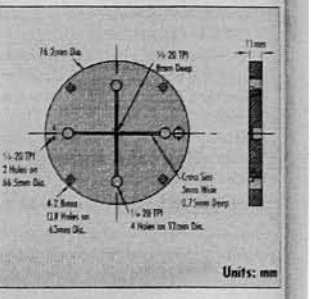

COMPACT ROTARY STAGES

2.62"

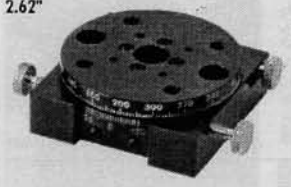

2.00"

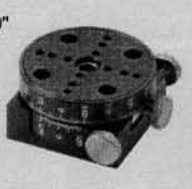

Compact miniature stages provide low-friction rotary movement with both coarse and fine adjustment. This allows for quick rotation over a continuous 360° travel, plus precise angular adjustment at any selected position. Features include preloaded angular contact ball bearing system, a positive position lock, a 2.00" or 2.62" diameter stage with tapped mounting holes and a calibrated dial with six minute vernier for accurate positional read-out. It can be combined with our compatible linear translation stages for multi-axis linear-rotary applications.

SPECIFICATIONS

Construction:	Aluminum-stainless steel
Finish:	Black anodized
Load Capacity:	10 lbs. (horizontal); 4 lbs. (vertical)
Vernier:	12 arc min. incr. over ± 2°
Range:	360° continuous (coarse adjust); 10° (fine adjust)
Drive Type:	Tangent Arm

Description	Stock No.	Prices		
		1-4	5-9	10+
2.00" Stage Diameter; Weight: 1 lb.	A33-465	$506.00	$480.70	Call
2.62" Stage Diameter; Weight: 1.8 lbs.	A38-193	$570.00	$541.50	Call

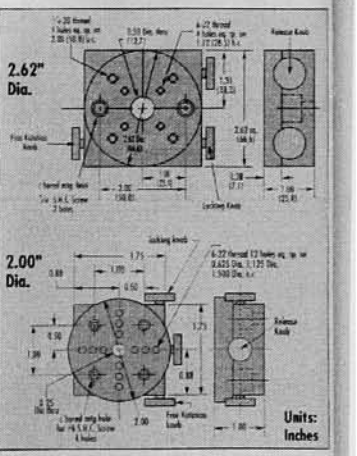

For OEM Quantity Pricing please call Edmund Industrial Optics at 800-363-1992